Production of CH_4 and CO on Cu_xO and Ni_xO_y coatings through CO_2 photoreduction

Production of CH_4 and CO on Cu_xO and Ni_xO_y Coatings through CO_2 Photoreduction

Manuel Alejandro Ávila-López[1], Jeannie Z. Y. Tan[2], E. Luévano-Hipólito[3], Leticia M. Torres-Martínez[1,4,], M. Mercedes Maroto-Valer[2,*]*

[1] Universidad Autónoma de Nuevo León, Facultad de Ingeniería Civil-Departamento de Ecomateriales y Energía, Cd. Universitaria, C.P. 66455 San Nicolás de los Garza, NL, México.

[2] Research Centre for Carbon Solutions (RCCS), School of Engineering & Physical Sciences, Heriot-Watt University, Edinburgh, United Kingdom.

[3] CONACYT - Universidad Autónoma de Nuevo León, Facultad de Ingeniería Civil-Departamento de Ecomateriales y Energía, Cd. Universitaria, C.P. 66455 San Nicolás de los Garza, NL, México.

[4] Centro de Investigación en Materiales Avanzados, S. C. (CIMAV) Miguel de Cervantes 120 Complejo Ind. Chihuahua, Chihuahua, Chih. 31136 México.

ABSTRACT

CO_2 capture and photocatalytic reduction to hydrocarbons is an interesting yet challenging area that requires photocatalysts with the capability to capture and photoconvert CO_2 simultaneously. Furthermore, earth-abundant photocatalysts with high efficiency and product selectivity are essential for commercialization. Thus, two earth-abundant photocatalysts based on copper and nickel oxides were selected to produce solar fuels from CO_2 photoreduction. The photocatalysts were immobilized on commercial glass fibers substrates by a facile one-step microwave-hydrothermal method. Cu_xO (x=1, 2) and Ni_xO_y (x=1, 2 and y =1, 3) coatings on glass fiber were evaluated as photocatalysts in two different reactors to investigate the selectivity in a continuous reactor and a batch system. Two different light sources were employed: a heterochromatic lamp to simulate part of the solar light in the continuous reactor and a LED visible light in the batch reactor. CuO/Cu_2O photocatalysts exhibited a selective production of CH_4 (95 μmol g^{-1} h^{-1}) and CH_3OH (177 μmol g^{-1} h^{-1}) from CO_2 photoreduction in the continuous and batch continuous systems, respectively. The superior performance was attributed to the unique rod-shape morphology, the presence of oxygen vacancies and efficient charge transfer in the CuO/Cu_2O heterostructure with high affinity towards CO_2, resulting the formation of mono- and bidentate carbonate species during the CO_2 photoreduction reaction. Ni_xO_y coating with 2D cubic shape produced CO (103 μmol g^{-1} h^{-1}) and HCOOH (4245 μmol g^{-1} h^{-1}), associating with the low CO_2 affinity and less efficient charge separation compared to CuO/Cu_2O heterostructure.

Keywords: Photocatalysis; CO_2 reduction; Solar fuels; CO_2 adsorption; CuxO; NixOy.

1. Introduction

Carbon dioxide (CO_2) is considered the main greenhouse gas (GHG) responsible for climate change [1]. Fossil fuel utilization is the main contributor to anthropogenic CO_2 emissions [2,3]. One of the promising routes to address CO_2 emissions and provide an alternative energy source is implementing artificial photosynthesis. This process could be carried out through CO_2 photocatalytic conversion into light hydrocarbon molecules, such as CH_4, syngas (CO/H_2), alcohols, and aldehydes [4-6].

TiO_2 has been extensively used as a photocatalyst reduction of CO_2 process. However, TiO_2 is not an ideal photocatalyst to carry out the CO_2 photoreduction because it has a low affinity for CO_2 in the presence of H_2O [7]. The use of other oxides such as Cu_xO (x=1, 2), NiO, Fe_2O_3, ZnO, and MgO, represents an excellent option to be used in this process due to their ability to attract electrons and provide active sites for CO_2 fixation, such as oxygen vacancies (OVs) [8-13]. Copper and nickel oxides have resulted in good efficiencies for the CO_2 photoconversion process; however, their use has been limited as co-catalysts for photocatalytic CO_2 conversion [9, 12-14].

Cu_xO (x= 1, 2) materials have shown potential advantages for the CO_2 conversion because CuO favors CO_2 adsorption through the formation of monodentate and bidentate carbonate species [14]; whereas Cu_2O provides adequate reduction potential, visible-light absorption, and selective active-sites to capture electrons, and enhancing multi-electron reactions on its surface [15, 16]. These properties have favored the production of CH_4. On the other hand, NiO has been used as a co-catalyst for CO_2 photoreduction to CH_3OH, CH_4, and CO in some composite materials, such as $NiO/In_2O_3/TiO_2$ [17], $Ni/NiO/g\text{-}C_3N_4$ [18], $NiO/InTaO_4$ [8], and ZnO/Ni [19]. Previous works suggest that the coexistence of Ni^{2+}/Ni^0 pairs in core-shells

structures enhanced the electron transfer among the semiconductors and it promotes the formation of CO from the CO_2 photoreduction [17, 18]. From these works, it seems that the presence of NiO and Cu_xO favored the generation of CO and CH_4 in gas phase continuous reactors, respectively. However, the selectivity of these two photocatalytic materials has not been explored in detail under similar operation parameters since most of the works use different high-power lamps that emit in the UV range [12,13,20-28]. Therefore, studying of both oxides under similar reaction conditions is interesting and could help understand each oxide's selectivity in the continuous and batch systems since previous reports suggest different reaction mechanisms in the gas (continuous) and liquid (batch) phases [29, 30], as is shown in **Figure 1**.

Some of the challenges related to the photocatalytic materials, for the scaling-up of the CO_2 photoreduction, are the rapid recombination of the photogenerated charges, light absorption, low surface areas, lack of active sites adequate for the reaction (e.g., OVs), the deactivation or poisoning of the photocatalysts, the CO_2 adsorption or the desorption of by-products, the low selectivity, and the immobilization of the photocatalyst [4]. Considering these factors, this work proposes two complementary strategies for the design of efficient photocatalytic materials to provide insights to overcome some of these challenges. One of the strategies implemented was the design of heterostructured materials to reduce the recombination of the photogenerated charges in earth-abundant copper and nickel oxides [31, 32]. In this context, the use of heterostructured materials represents a good strategy to promote an improvement of the separation of photogenerated electron-hole pairs and enhance the selectivity of solar fuel production. For this purpose, the use of type-II heterostructured materials promotes the formation internal electric fields that can drive the electron and holes transfer in opposite directions, which decrease the recombination of the photogenerated charges, as is also shown

in **Figure 1**. In this scheme is also included the charge transfer in type-II heterostructured materials.

Secondly, the immobilization of photocatalysts on commercially available, low-cost, and flexible substrates, e.g., glass fibers, could favor the process of scaling-up as well as providing a higher exposed area for photocatalytic reaction, promoting efficient charge transport, and enhancing light absorption [33]. The use of immobilized photocatalyst has been successfully demonstrated in recent reports for CO_2 photoreduction, as is shown in **Table S1**.

In summary, this work focuses on increasing solar fuel production using visible-light active heterostructure photocatalysts immobilized on flexible and low-cost substrates in a continuous and batch systems. The heterostructures were evaluated in a continuous reactor under UV-Visible light from a solar simulator. At the same time, in the batch experiments, a LED visible lamp was used to activate the materials. In addition, a practical yet novel approach to fabricate nickel and copper oxides coatings, which possessed a high affinity towards CO_2 and enhanced visible-light absorption, is proposed herein.

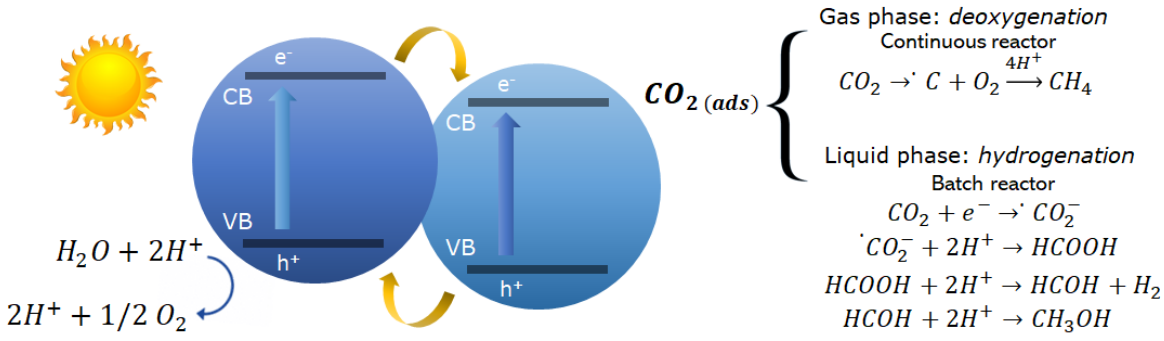

Figure 1. Photocatalytic mechanism of heterostructured materials in the gas and liquid phases.

2. Experimental Section

2.1. Fabrication of Cu_xO (x=1, 2) and Ni_xO_y (x=1, 2 and y =1, 3) coatings on glass fibers

The deposition of Cu_xO (x=1, 2) and Ni_xO_y (x=1, 2 and y =1, 3) on glass fiber (GF) were performed by an in-situ microwave-hydrothermal (MH) method. The oxides were deposited on GF substrates with the following composition: SiO_2, Na_2O, and CaO, with an open slit of 2.7 mm and an effective area of 2.73 cm^2 [33]. First, the substrate was cleaned under sonication for 25 minutes with pure acetone (Baker, 99.5%), methanol (DEQ, 99.9%), and distilled water. Then, the substrate was dried at 80 °C overnight before use.

The cleaned GF substrates were placed in an autoclave that contained an aqueous solution of $Cu(CH_3COO)_2 \cdot H_2O$ (Fermont, 99%) or $Ni(CH_3COO)_2 \cdot 4H_2O$ (Fermont, 99%), according to the experiment design, as shown in **Table 1**. Then, different quantities of glucose ($C_6H_{12}O_6$, Sigma, 99%) as reducing agent were added. Subsequently, NaOH (Fermont, 99%) was added slowly into the Cu and Ni solution. The autoclave was heated in a microwave reactor (Mars 6) at 300 W at 80 °C for 60 min. The coating on the GF was washed with distilled water and then dried at 100 °C overnight. The identification of the samples is shown in **Table 1**.

Table 1. Synthesis parameters used for the deposition of the films on the GF.

Sample ID	[NaOH] (M)	[$C_6H_{12}O_6$] (mol)
Cu-1	0.3	0.0
Cu-2	0.6	
Cu-3	0.3	0.015
Cu-4	0.6	
Ni-1	0.3	0.0
Ni-2	0.6	
Ni-3	0.3	0.015
Ni-4	0.6	

2.2. Material characterization

The crystalline phases of the coating were analyzed using X-ray diffraction (XRD, Bruker D8 Advance diffractometer). The measurements were performed in a 2θ interval from 10 to 70° with a step size of 0.02° for 0.3 s with Cu Kα radiation 1.5418 Å. The morphological characterization and elemental mapping were conducted with scanning electron microscopy (SEM) using a JEOL JSM-6490LV microscope with an acceleration voltage of 20 kV by placing the samples on carbon tape and covered with gold-palladium coating for the measurement. Furthermore, the surface of the samples was analyzed using a Luxo Microscope System model 273RB-RLI. Diffuse reflectance of the photocatalysts was determined using a Perkin Elmer Lambda 950 UV-Visible spectrophotometer equipped with a 150 mm integration sphere. The bandgap (Eg) was estimated using the Kubelka-Munk (K-M) function, considering a direct charge transfer on Cu and Ni transition oxides. With this data, the theoretical conduction and valence band potentials were calculated by equations 1 and 2.

$$E_{VB} = X - E^e + 0.5E_g \quad (1)$$

$$E_{CB} = X - E^e - 0.5E_g \quad (2)$$

where X is the absolute electronegativity, E^e is the energy of free electrons on a hydrogen scale (4.5 eV), and Eg is the energy band gap. Fourier transform infrared spectroscopy (FTIR) was used to study the surface properties of the fabricated samples before and after the CO_2 capture and photoreduction processes. The characteristic spectra of the samples were identified using the Thermo FTIR Nicolet iS50 kit in a range of 600-4000 cm^{-1}. Photoluminescence (PL) analysis was performed at room temperature in a fluorescence spectrophotometer (Cary Eclipse) integrated with a Xenon flash lamp. The samples were excited at 300 nm and an emission slit of 5 at room temperature. The crystal structure and shape of heterostructures were analyzed by transmission electron microscopy (TEM) using a JEOL JEM–2200FS. For

TEM characterization, the powders were suspended in isopropanol. The solution was dropped onto the Lacey carbon grids (300 mesh) and dried at room temperature. The surface composition of the coating was analyzed by X-ray photoelectron spectroscopy (XPS) using a Thermo Scientific Escalab 250 Xi with step energy of 200 eV for survey scans and 50 eV for high resolution scans with step sizes of 1.0 and 0.1 eV, respectively. Batch neutralization of the sample was accomplished using a combination of Ar low-energy ions and electrons. Photocurrent measurements were performed on FTO glass. For this purpose, the working electrode was prepared with each sample by the spin coating method; this method consists in preparing 5 mg of the sample in 10 mL of isopropanol and sonicated for 25 min. Then, the homogeneous solution was coated dropwise over an FTO glass with an active area of 1.0 x 1.0 cm^2 and dispersed by spinning at 2800 rpm for 20 s. The coated FTO glasses were then dried at 80 °C, and a similar step is repeated for consecutive layers (25 times). The prepared film was annealed at 200 ºC for 1 h, at 10 °C min^{-1}. Chronoamperometry was conducted using an Autolab with 0.1 M NaOH as an electrolyte. The irradiation source was turned on for 60 s and then off for another 60 s. These on-off cycles were repeated for 6 min.

2.3. CO_2 adsorption analysis

Temperature programmed desorption (TPD) was performed using a ChemBET Pulsar TPD from Quantachrome Instruments to evaluate the CO_2 adsorption affinity of the materials synthesized. 100 mg of the sample was placed in a U-shaped reactor between two pieces of quartz wool. The sample was heated in an inert atmosphere (N_2, 99.9995%) to 150 °C to eliminate adsorbed compounds for 3 h. Then, the sample was cooled down to 50 °C. Next, a flow of CO_2 (0.35 mL min^{-1}) was passed for 60 min and then replaced by He (99.9995%). The measurement started when a stable baseline was achieved. After that, the sample was

heated at 350°C at a constant rate of 10°C min^{-1}. The CO_2 desorption signal were recorded by Thermal Conductivity Detector (TCD).

Operando Diffuse Reflectance Infrared Fourier Transform Spectroscopy (DRIFTS) experiments were conducted on Agilent Cary 600 series spectrometer equipped with Harrick Praying Mantis reaction cell. The gas inlet of the cell was directly connected to a flow system equipped with mass flow controllers and a temperature controller. The cell outlet was connected to the mass spectrometer Hiden QGA MS. In each experiment, 20 mg of catalyst powder was placed in the cell. Before reaction, the KBr background was collected in presence of CO_2, which was flowing through the bubbler. 64 scans were collected per spectrum with a spectral resolution of 4 cm^{-1} and in the spectral range of 4000-400 cm^{-1}. The experiment was performed under UV-Vis irradiation at 24 and 40 °C and dark (24 °C) conditions to simulate the experimental conditions within the photocatalytic reactor.

2.4. Photocatalytic CO_2 reduction

a) Continuous reactor

Continuous gas-phase CO_2 photoreduction experiments were performed in a stainless-steel ring-type reactor, previously described in [34]. The coatings (2.5 x 4 cm^2) were placed in the photoreactor, with a volume of 1.96 mL, before it was sealed. The system was purged with pure CO_2 to remove residual air overnight. A constant flowrate of CO_2 was set to 0.35 mL min^{-1}, with a relative humidity of 1.8% measured by an Arduino sensor. In this case, H_2O was used as precursor of H^+ ions for the CO_2 photocatalytic reduction. The temperature of the reaction (40 °C) was maintained using a hot plate. The light source was a heterochromatic lamp model OmniCure S2000 that emits in 300-600 nm wavelength to simulate the solar light irradiation. The lamp was placed 30 mm above the surface of the sample. The irradiance

(150 mW cm^{-2}) was measured using an OmniCure R2000 radiometer (±5%). An inline GC/TCD/FID (Agilent, Model 7890B series), a Hayesep Q column (1.5 m), 1/16-inch OD, 1 mm OD), Molecular Sieve 13X (1.2 m), 1/16-inch OD, 1 mm ID) was used to quantify the photoreaction products. The system also has a nickel catalyzed methanizer and a flame ionization detector (FID) to analyze the products every 4 min. The products CH_4 and CO were measured by FID, while TCD identified H_2 and O_2.

To evaluate the recyclability of each set of coatings, third cycling tests was conducted under identical conditions. After each test, the sample was heated at 200 °C for 2 h before employing in the next cycle.

b) Batch reactor

The samples with the highest performance for CO_2 photoreduction were evaluated in a batch quartz reactor in liquid phase at room temperature. For these experiments, the coatings (2.73 cm^2) were placed inside the batch reactor with 150 mL of distilled water under magnetic stirring. The reactor was bubbled with CO_2 for 30 minutes to replace the solution's dissolved oxygen. In this reactor, a different light source was used to emulate the visible light from the solar light. The reactor was irradiated with 2 LED lamps of 20 W each, which exhibit two emissions at 443 and 535 nm, from the sides. The reaction products in the liquid phase were monitored by different techniques, as described here. Formic acid (HCOOH) and formaldehyde (CH_2O) were measured with high-performance liquid chromatography (HPLC) after 1 h of reaction. The CH_2O quantification was carried out by injecting 25 µL of the liquid sample into the system, with a Fenomenex C-18 column, using a 50:50 v/v acetonitrile-water (HPLC grade Baker) mixture as a carrier. Before the sample was injected, the liquid sample was derivatized, forming a complex product of the reaction with 2-4, dinitrophenyl hydrazine (Aldrich, 98%) and phosphoric acid (Baker, 98%) [35]. On the other hand, the HCOOH

measurement was carried out by injecting 15 μL of previously sample filtered reaction liquid sample [36]. Additionally, CH_3OH was determined by gas chromatography. To corroborate the reaction products, the liquid sample was analyzed by nuclear magnetic resonance (^1H NMR) analysis on a Bruker 400 MHz Avance III HD spectrometer (Bruker, BioSpin, USA) equipped with a 5 mm BBO SP probe with Z-field gradient. TopSpin 3.6.1 software (Bruker Biospin) was used for FID processing. CHENOMX NMR Suite 8.5 software was used for signal identification.

3. Results and discussion

3.1. Material properties

Homogeneous Cu_xO and Ni_xO_y coatings on GF were fabricated with a simultaneous microwave-hydrothermal method in the presence of glucose, as a reducing agent, in a basic medium. X-ray diffraction (XRD) was used to investigate the crystalline phases of the coatings (**Figure 2**). Cu_xO (x=1, 2) coatings exhibited a wide range of crystal compositions. The coatings obtained in the absence of the reducing agent (Cu-1 and Cu-2) exhibited the monoclinic phase of CuO (JCPDS:45-0937). The reflections of CuO were observed at 32.5, 35.8, and 38.6°, which correspond to the crystal planes (110), (-111), and (111), respectively (**Figure 2a**). Traces of the Cu_2O phase were also identified in these samples (**Table 2**). The rest of the samples (i.e., Cu-3 and Cu-4) synthesized in the presence of a reducing agent exhibited a mixture of Cu_2O and Cu phases in different proportions (**Table 2**). Specifically, Cu-3 presented a mixture of Cu_2O/Cu (i.e, Cu_2O as majority phase), whereas Cu-4 sample showed mainly elemental copper (Cu^0) with trace amount of Cu_2O (JCPDS: 01-71-4609 and 01-71-3645, respectively). The addition of NaOH also significantly influenced the crystal phase

mixtures in the samples. Notably, the increase of NaOH concentration promoted the reduction of Cu^{2+} to Cu in samples Cu-3 and Cu-4.

The nickel oxide coatings exhibited only the cubic structure of NiO (JCPDS:01-089-7131, **Table 2**). These samples presented intense reflections at 2θ = 37.4°, 43.4°, and 62.9°, corresponding to (110), (200) and (111) planes, respectively **(Figure 2b)**.

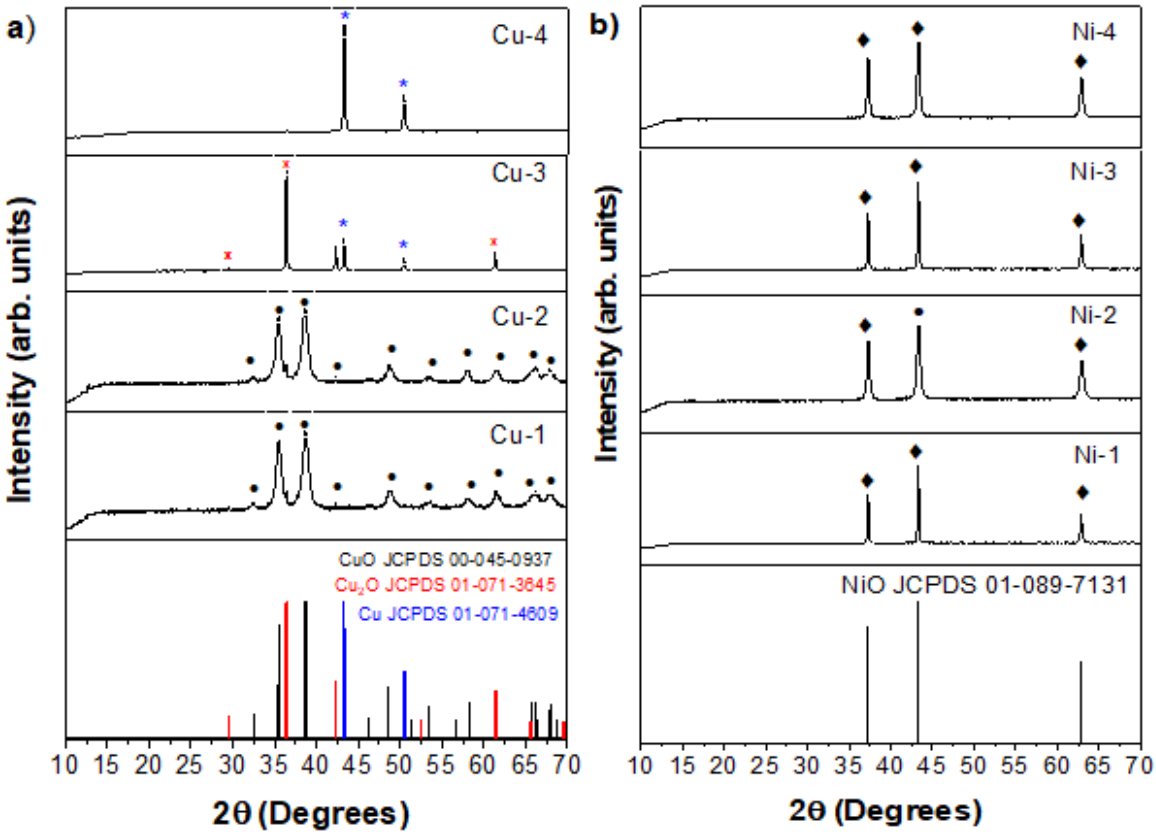

Figure 2. XRD patterns of a) Cu_xO (x=1, 2) and b) NiO coatings.

The morphology of the fabricated coatings was analyzed by SEM. All the Cu_xO coatings showed a variety of morphologies in the presence of glucose and different concentration of NaOH (**Figure 3**). Sample Cu-1 showed agglomeration with elongated bars (**Figure 3a**), whereas sample Cu-2 exhibited a more defined morphology of bars with an average width

and length of 1.3 and 5.2 µm, respectively (**Figure 3b**). Cu-3 and Cu-4 coatings, which possessed a mixture of Cu_2O/Cu phases, exhibited different octahedral particles with an agglomeration (**Figure 3c and d**) due to glucose addition.

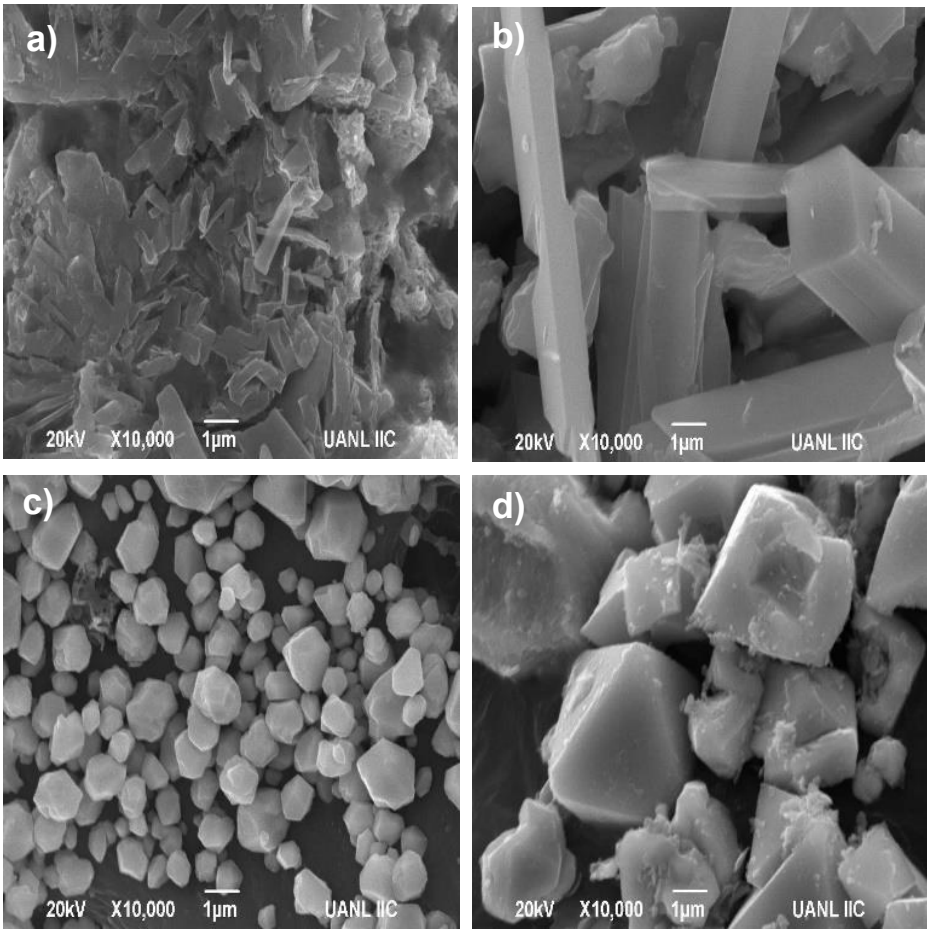

Figure 3. SEM images of a) Cu-1, b) Cu-2, c) Cu-3 and d) Cu-4 samples.

Different amounts of NaOH and glucose were also employed to synthesize nickel oxides. Sample Ni-1 exhibited a notable agglomeration and undefined morphology (**Figure 4a**). When the dosage of NaOH was increased to 0.6 M, the morphology of Ni-2 revealed irregular flakes with a thickness of ~275 nm and agglomerated cubes (~620 nm) (**Figure 4b)**. The addition of glucose promoted the formation of nanoflakes (~400 nm), as shown in samples Ni-3 (**Figure 4c**). When the highest dosage of NaOH (0.6 M) and glucose was added, a well-

defined cubic microstructure (~540 nm) was observed in the sample Ni-4 (**Figures 4d**). The average particle size is summarized in **Table 2**. EDS mapping obtained under SEM evidenced the homogeneity of the copper and nickel of the fabricated samples on GFs (**Figure S1**).

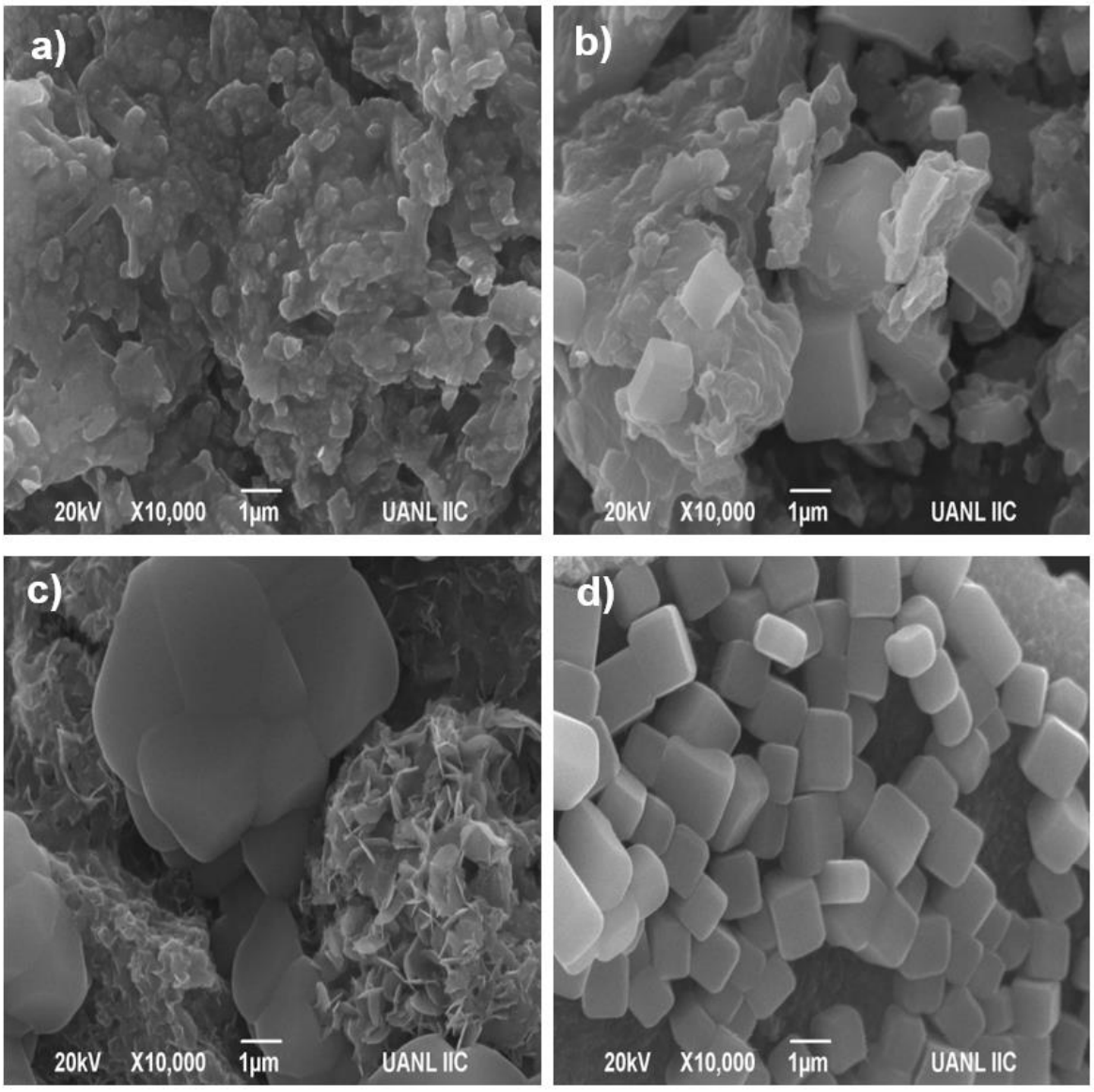

Figure 4. SEM images of a) Ni-1, b) Ni-2, c) Ni-3 and d) Ni-4 samples.

The bandgap energy of the fabricated samples was estimated from the graph of $[F(R\infty)h\nu]^{1/2}$ *vs* photon energy (**Figure 5**). The bandgap energies of the synthesized samples are summarized in **Table 2**. The Cu-1 and Cu-2 coatings, dominated by CuO particles, presented similar bandgap energies, as reported previously (1.5-1.6 eV, **Figure 5a**) [14]. The rest of the samples (Cu-3 and Cu-4) exhibited an additional adsorption band at 2.1-2.3 eV was probably due to the presence of Cu_2O (**Figure 2a**) [37].

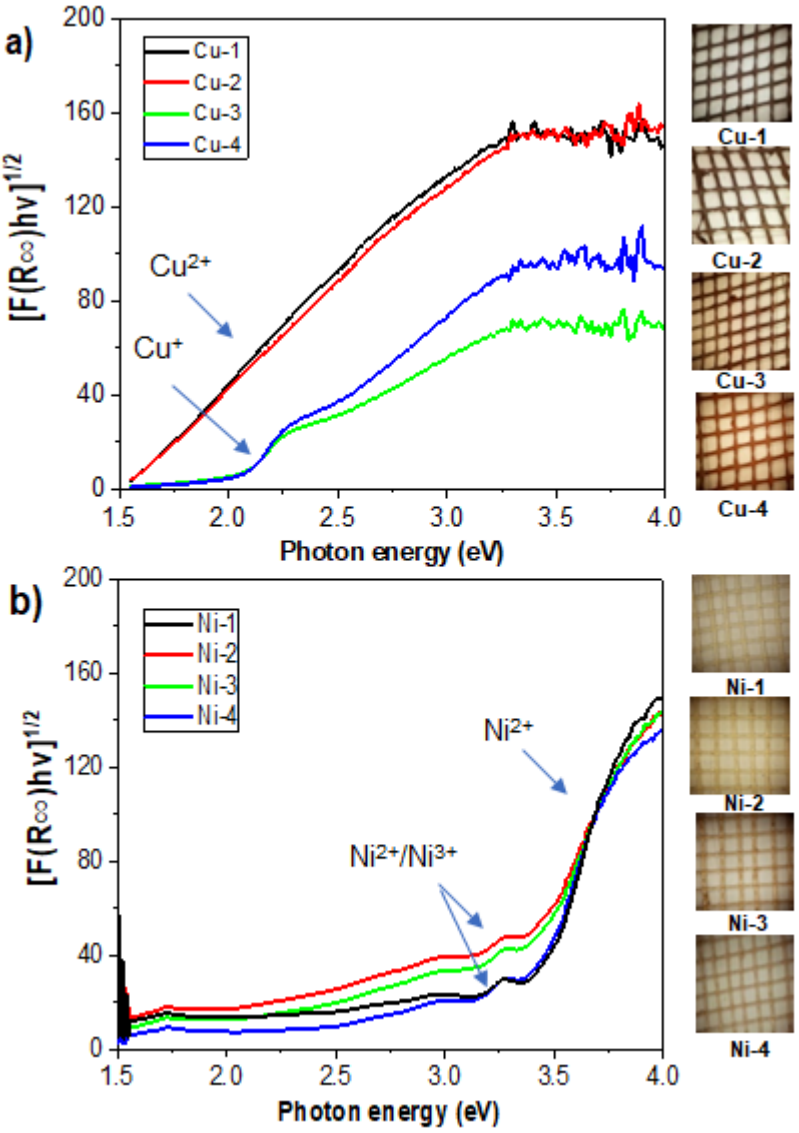

Figure 5. K-M spectra (left) and optical images (right) of the coatings: a) Copper oxides and b) Nickel oxides.

The K-M spectra of nickel oxides coatings are shown in **Figure 5b**. These samples exhibited bandgap energies between 3.3-3.5 eV, which are close to the values reported in the literature (i.e., 3.1- 3.6 eV) [38]. These values are characteristic of the green NiO (Ni-1 and Ni-3). In addition, a much weaker absorption band at 3.2-3.3 eV could be attributed to the Ni^{2+}/Ni^{3+} moiety [39, 40]. The presence of Ni^{2+}/Ni^{3+} is further discussed below using XPS.

Table 2. Physicochemical properties of the coatings.

Sample ID	Crystal phases identified	Particle size (nm)	Bandgap (eV)
Cu-1	CuO Cu_2O	300	1.5
Cu-2	CuO Cu_2O	1330	1.6
Cu-3	Cu_2O Cu	500	1.5
Cu-4	Cu Cu_2O	3300	2.3
Ni-1	NiO	275	3.2
Ni-2	NiO	620	3.3
Ni-3	NiO	400	3.2
Ni-4	NiO	540	3.3

PL spectra were used to study the recombination of charge carriers. The PL emission spectra of Cu_xO coatings exhibited two distinct peaks in the wavelength range of 600-900 nm (**Fig-**

ure 6a). Both peaks were assigned to the radiative emissions of the recombination of electrons and holes on CuO [41]. Cu-1 and Cu-2 samples showed a lower PL intensity, indicating a lower recombination rate as compared to Cu-3 and Cu-4 samples. This observation evidenced the efficient isolation of e^{-}-h^{+} pairs in the CuO/Cu_2O heterostructures [42].

The nickel oxides coatings showed a broad UV emission band peak at 378-380 nm corresponding to the radiative emission of the recombination of photogenerated charges in NiO (**Figure 6b**) [43]. Sample Ni-3 exhibited the lowest PL intensity, indicating a more efficient charge transfer with the flake structured sample.

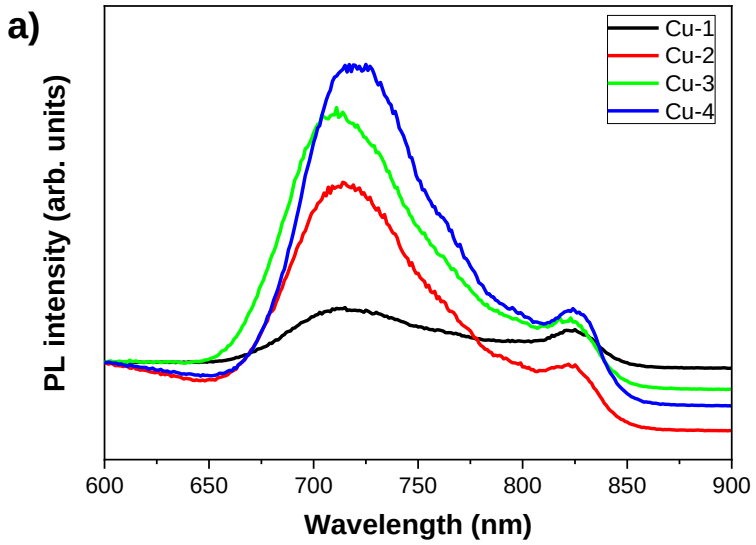

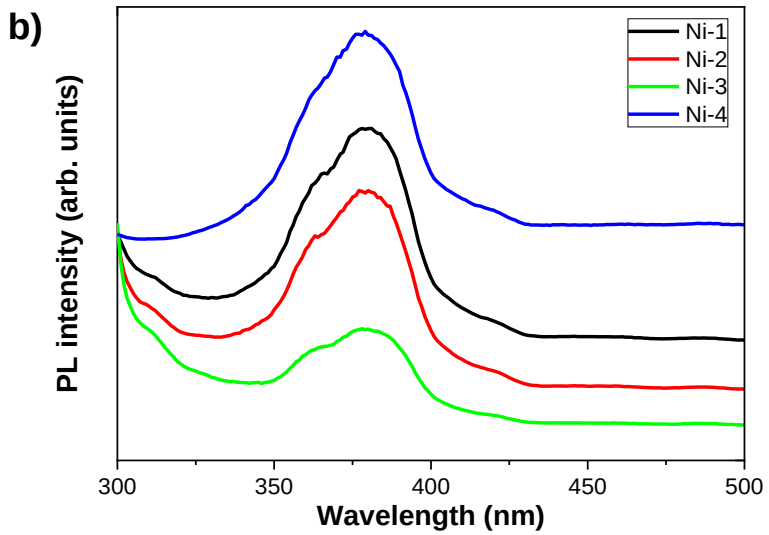

Figure 6. Photoluminescence (PL) emission spectra of the coatings (λ_{exc}= 300 nm).

3.2. Evaluation of CO_2 adsorption

FTIR spectroscopy was used to identify the CO_2 molecule fingerprint on the coatings (**Figure 7**). In general, copper oxides exhibited much more intense troughs than the coatings of nickel oxides, indicating that CuO samples possessed a higher affinity towards CO_2 molecules than nickel oxides. Specifically, Cu-1 and Cu-2 revealed two types of absorption bands at 1560 and 1410 cm^{-1} and 1340 and 1020 cm^{-1}, which were assigned to the monodentate and bidentate carbonate species, respectively [44-46]. However, these bands were absent in Cu-3 and Cu-4, probably attributed to the low basicity of Cu_2O and Cu that had a low affinity towards CO_2. On the other hand, the weak trough (1410 cm^{-1}) shown in the nickel oxides suggested only the monodentate bond presented on the surface of these samples.

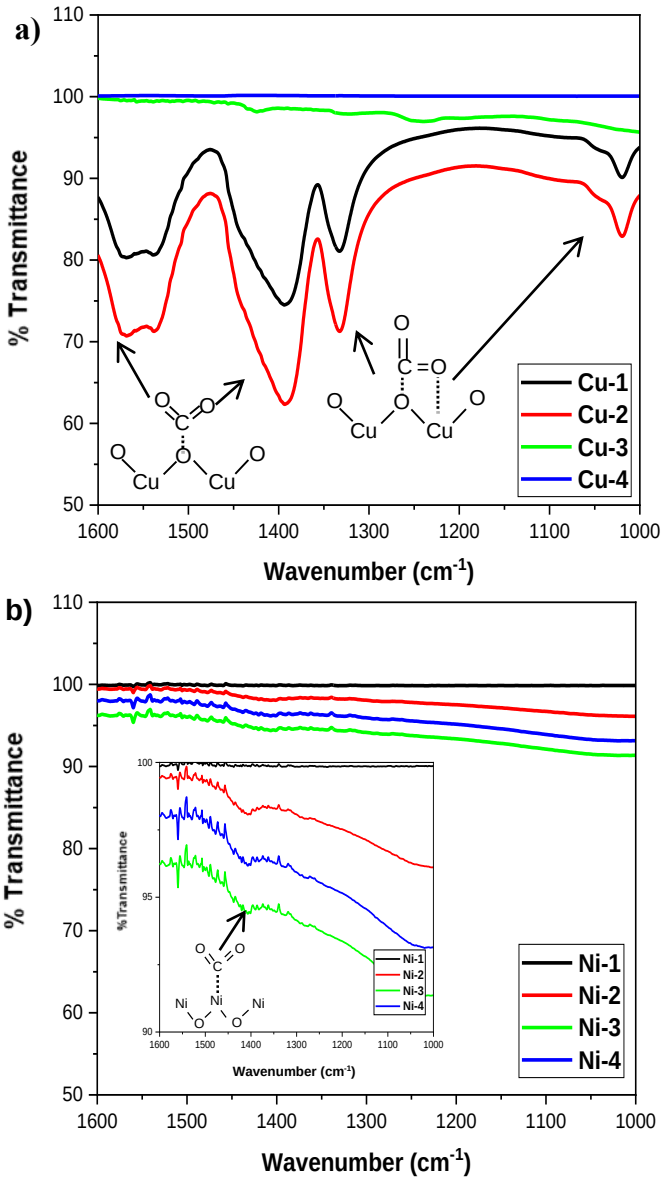

Figure 7. FTIR spectra of a) Copper oxides and b) Nickel oxide coatings.

Cu-1 and Cu-2 coatings, which exhibited a higher affinity towards CO_2 compared to the other fabricated samples, were further evaluated using TPD **(Figure 8)**. Cu-1 with higher CuO content compared to Cu-2 showed a higher CO_2 adsorption capacity. This observation agreed with the FTIR analysis, as shown in **Figure 7a**. The physical-desorption temperature of the samples was close to 280 °C for Cu-1 and Cu-2, respectively. This could be associated with

the exothermic enthalpy of CuO for CO_2 adsorption (ΔH_{ads}= -45.5 kJ mol^{-1}) [47]. The CO_2 chemical-desorption in the Cu-1 and Cu-2 samples was observed at ~320 °C, which may be related to the decomposition temperature of $CuCO_3$ around 300°C. It is worth mentioning that the rest of the samples did not show any response to the adsorbed CO_2 under the same conditions. This could be attributed to the presence of Cu and Cu_2O in the samples that hindered CO_2 adsorption since these phases exhibited endothermic enthalpies in this process ($\Delta H_{ads}Cu_2O$ = +142 kJ mol^{-1}) [47]. From the results reported above, samples Cu-1 and Cu-2 seems to be a potentially good candidate for the CO_2 adsorption and subsequent photocatalytic reduction of CO_2, since they have a low CO_2 desorption temperature that favored the subsequent conversion of CO_2. On the other hand, the adsorption over the nickel oxides samples was under limit detection, and the TPD patterns are in the supplementary section (**Figure S2**).

The FTIR spectra show the moieties adsorb on the surface of the photocatalyst during the reaction. In contrast, the TPD pattern shows the amount of CO_2 desorb. When the TPD peak is high, it indicates more negligible adsorption. This process also describes the physical- and chemical adsorption on the photocatalyst surface. Hence, the FTIR and TPD results show the correct relationship, in which high adsorption of CO_2 (FTIR) and low desorption (TPD), as shown in sample Cu-2, which eventually favor the CO_2 photoconversion. On the other hand, Ni-3 does not show CO_2 adsorption, which could modify its selectivity of the CO_2 reduction, as will be further discussed.

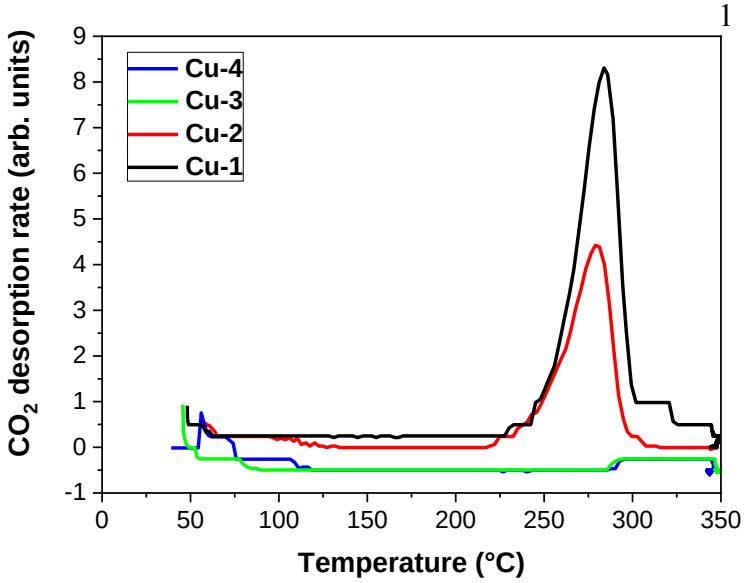

Figure 8. TPD profiles of the fabricated Copper oxides samples.

The sample with the highest affinity to CO_2 (i.e., Cu-2) was further studied with *operando* DRIFTS (**Figure S3**). The Cu-2 sample showed a strong absorption band at 2348 cm^{-1}, associated with the adsorbed CO_2, when CO_2 was fed into the reactor at 24 °C in the dark. In addition, bands at around 1620, 1420, and 1296 cm^{-1}, which were assigned to the asymmetric CO_3 stretching vibration [$\nu_{as}(CO_3)$], symmetric CO_3 stretching vibration [$\nu_s(CO_3)$] and O−H deformation vibration [δ (O−H)] of monodentate bicarbonate species (*m*-HCO_3^{2-}), respectively, were observed upon CO_2 feeding in the dark [48, 49]. When the UV-vis light irradiated onto the sample, the intensity of these bands decreased immediately. The bands at around 1540 and 1384 cm^{-1} correspond to the [$\nu_{as}(CO_2)$] and [$\nu_s(CO_2)$] of the bidentate formate species (*b*-HCO_2^{2-}) [50]. This observation suggested that the CO_2 molecules adsorbed on the surface of Cu-2 were mainly *m*-HCO_3^{2-} and converted to *b*-HCO_2^{2-} through the reaction with OH^- on the surface or oxygen vacancies (OVs) of Cu-2. When the reaction temperature increased to 40 °C, the bands of *m*-HCO_3^{2-} continued to decrease, whereas *b*-HCO_2^{2-} increased steadily. In other words, the adsorption of CO_2 and conversion of *m*-HCO_3^{2-} to *b*-HCO_2^{2-}

were enhanced at elevated temperatures. The *operando* DRIFT results suggested that the mechanism for the photocatalytic CO_2 reduction route of Cu-2 was through the carbene pathway.

According to the FTIR and *operando* DRIFTS results, the fabricated Copper oxides and Nickel oxides coatings were proposed to be partially carbonated during CO_2 adsorption. The proposed mechanism was illustrated in **Figure S4**. In the case of the CuO/Cu_2O, the surface oxygen present on the CuO could act as a Lewis base site that could donate an electron to the C=O bond of CO_2. This phenomenon promoted the formation of monodentate bonds (carbon coordination bonds) and bidentate at the CuO surface, as shown in **Figure S4a**. The Cu, close to OVs, acts as a Lewis acid site by accepting electrons, interacting with oxygen from CO_2 producing $Cu \cdots O - C = O$ species. On the other hand, the bidentate coordination bond occurred by interacting the Cu and O in the CuO with CO_2 molecules [9, 14].

The FTIR spectra of the nickel oxides samples did not show significant changes before and after the CO_2 purge (**Figure 7b**). Only an appreciated amount of the monodentate species was formed on the NiO surface (**Figure S4b**).

3.3. Photocatalytic CO_2 reduction in a continuous system

The Copper oxide and Nickel oxide coatings were evaluated for the photocatalytic reduction of CO_2 in the gas phase in a continuous reactor under UV-Visible light. The amounts of different gaseous products (H_2, CO, and CH_4) was monitored with GC. CH_4 was the main product of the photocatalytic reduction of CO_2 when copper oxides were used as the photocatalyst, while H_2 and CO were generated in low amounts (<10 ppm), as shown in **Figure S5**.

The Cu-1 film showed the highest production rate of CH_4 (94.7 μmol g^{-1} h^{-1}) followed by the Cu-2 sample (67.1 μmol g^{-1} h^{-1}), which showed up to 32 times higher production than other reports (**Table S1**) [7, 12, 13, 20, 21, 24-28]. However, Cu-2 revealed a more consistent production of CH_4 than Cu-1 throughout the 4 h reaction, which could be attributed to several factors:

- A higher affinity for CO_2 resulted in the formation of monodentate and subsequent bidentate species, as is observed in the FTIR spectra.
- Rod morphology that provided active sites for effective CO_2 adsorption.
- The coexistence of CuO/Cu_2O in this sample resulted in the type-II heterostructure formation that promoted efficient charge transfer, supplying sufficient protons (8 H^+) and electrons (8 e^-) for the conversion into CH_4.

Cu-3 and Cu-4 with a mixture of Cu/Cu_2O showed a lower production of CH_4 than those samples with a higher content of CuO (i.e., Cu-1 and Cu-2), as seen in **Figure 9**. This could be associated with a rapid photo-oxidation of Cu/Cu_2O and low adsorption of CO_2 on these samples. It should be noted that the substrates, which consisted of CaO and Na_2O, exhibited some activity for solar fuels generation due to their intrinsic properties on CO_2 adsorption [33].

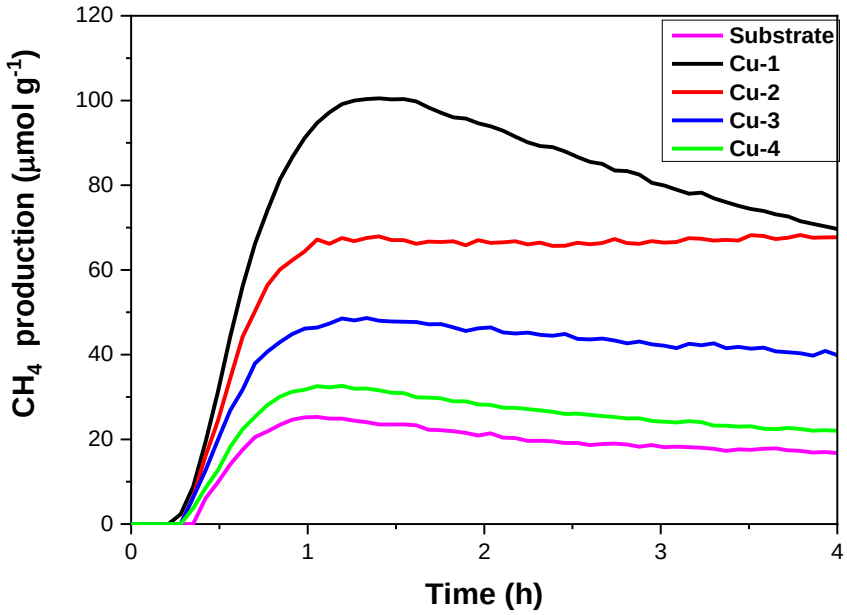

Figure 9. CH_4 evolution using the Copper oxide coatings under 300-600 nm irradiation.

The synthesized nickel oxides samples showed only CO production under the same experimental conditions (**Figure 10**). Ni-3 sample generated the highest amount of CO (103 µmol g^{-1} h^{-1}), which was around 3 times higher than the previous reports in the literature [20-23, 26-28]. Other carbonaceous by-products (CH_4) were obtained only in trace amounts (**Figure S6**). The superior results were attributed to the unique 2D morphology of flaky agglomeration and the coexistence of NiO and Ni_2O_3 moieties in Ni-3.

Also, it is important to note that the amount generated by the samples was distinguished than we observed having blank substrates, as shown in **Figures 9** and **10**.

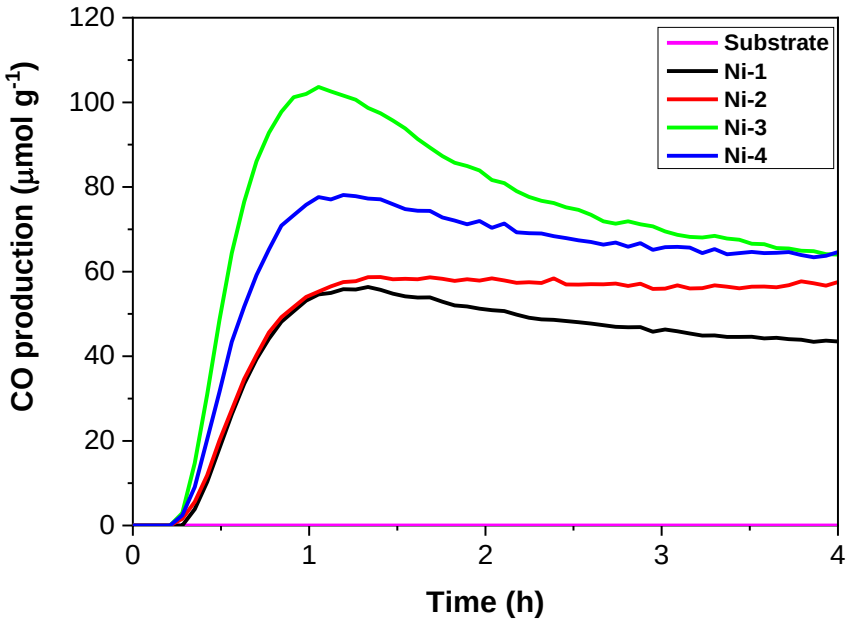

Figure 10. CO evolution using the nickel oxides coatings as photocatalyst under 300-600 nm irradiation.

Also, each system's best heterostructure activity was compared to single metal oxides to highlight the importance of the coexistence of CuO/Cu_2O and NiO/Ni_2O_3 phases on the coatings. A previous report of CuO coatings grown on glass fibers suggested that it exhibits selectivity for CH_4 production [51]; however, the stability and the efficiency for CH_4 generation with the CuO/Cu_2O heterostructure obtained here is higher. Regarding to the nickel-based samples, an additional sample was synthesized without the addition of NaOH or reducing agent, which was identified as Ni-0. This sample exhibited only the monoclinic NiO phase, and it did not exhibit the characteristic band of the coexistence of Ni^{2+}/Ni^{3+} sample, which confirms the presence of only NiO in this sample (Ni-0), as is shown in **Figure S7a,b**. The photocatalytic results show that pure NiO only produce half the yield as of sample with NiO and Ni_2O_3

heterostructure (**Figure S7c**). On the other hand, a coating of a commercial TiO_2 P-25 photocatalyst was prepared for comparative purposes. As shown in **Figure S8**, TiO_2 P-25 presented an apparent deactivation (55%) during the photocatalytic evaluation. This result could be explained by means of blocking the active sites through the deposition of carbon-containing products [52]. TiO_2 P-25 did not exhibit selectivity towards CH_4 or CO production since both products were obtained with 50 and 7 μmol g^{-1} h^{-1} production, respectively, after 4 h of reaction.

A general comparison of the CH_4 and CO production with the copper and nickel-based heterostructures and the traditional TiO_2 photocatalyst was included in **Figure S9**. As it can be seen, the CuO/Cu_2O and NiO/Ni_2O_3 heterostructures exhibited higher activity than the individual oxides: CuO, Cu_2O/Cu (Cu-3 sample), NiO and the traditional TiO_2 photocatalyst, which evidences its effectiveness for the selective generation of CH_4 and CO, respectively. Therefore, both compounds are good candidates to be used as alternative green fuels for energy process generation and other applications.

To provide further insights with Cu-2 and Ni-3, which showed the best performance in CO_2 photoreduction amongst the fabricated samples, these samples were further characterized using transient chronoamperometry (**Figure 11**) and HRTEM techniques (**Figure S10**) to elucidate the differences on their photocatalytic activity. Sample Cu-2 showed a *p*-type behavior with a negative photocurrent response, and the photocurrent density 2 was stable throughout the chronoamperometry measurements. However, the Ni-3 film, which was expected to be a *p*-type semiconductor, showed an *n*-type characteristic with a positive photocurrent response [53]. This observation could be attributed to defects within the crystalline structure, such as OVs, leading to the formation of Ni_2O_3 [54].

Specifically, Cu-2 showed a higher photocurrent (-27.3 μA cm^{-2}) than Ni-3 (0.41 μA cm^{-2}). The delta observed in the charge density in the coatings indicated a surplus of holes available in the photocatalyst valence band that could interact with the water molecule to generate hydroxyl radicals (·OH) and release protons (H^+). Hence, the result suggested that Cu-2 managed to photogenerated more electron-hole pairs for the photo-redox reaction, thus leading to a higher conversion efficiency than Ni-3.

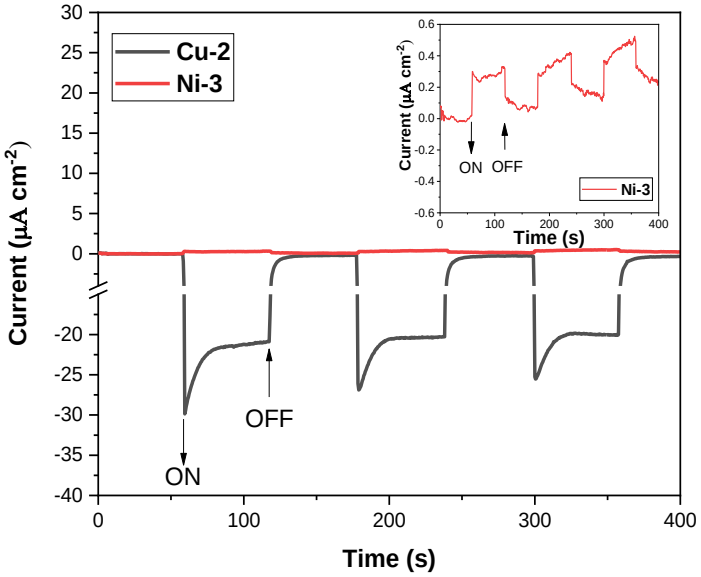

Figure 11. Chronoamperometric pattern of the Cu-2 and Ni-3 samples.

The morphology of Cu-2 and Ni-3 observed under TEM (**Figure S10a and b, respectively**) presented similar structures are those observed under SEM (**Figure 3**). HRTEM images evidenced the presence of the heterostructures in Cu-2 and Ni-3 (**Figure S10c and d)**. The CuO (111), and Cu_2O (211) and (200) crystal planes were identified with *d*-spacings ~0.23, ~0.17, and ~0.21 nm, respectively (**Figure S10c**); whereas the lattice fringes of NiO (200) and Ni_2O_3 (112) revealed an interplanar spacing of ~0.20 and 0.17 nm, respectively.

3.4. Characterization of the coatings after photocatalytic testing

The surface compositions and elemental valence states of the best performance coatings (i.e., Cu-2 and Ni-3) were investigated by XPS before and after the photocatalytic experiments. The analysis of the Cu-2 film surface before and after the photocatalytic reaction is shown in **Figure 12**. Three peaks at 284.4, 285.2, and 288.5 eV are associated with the C-C, C-O, and O-C=O bonds, respectively, of the adsorbed CO_2 (**Figure 12a**) [14, 55, 56]. The O 1s spectrum was fitted with four peaks centered at 529.6, 531.0, 531.9, and 533.3 eV (**Figure 12b**), corresponding to the oxygen in the lattice structure (O_L) of the O_L-CuO and O_L-Cu_2O [57, 58], OVs [59, 60], and oxygen adsorbed on the surface with low coordination related with C-O (O_a) [61, 62], respectively. Meanwhile, the Cu 2p spectrum was deconvoluted in two peaks attributed to Cu^+ and Cu^{2+} at 933.1 and 953.1 eV, respectively (**Figure 12c**) [63-65]. The Cu^{2+} peaks and their respective satellites (Cu $2p_{3/2}$ and Cu $2p_{1/2}$) appeared at 934.3, 954.3, 961.4, and 962.5 eV for Cu-2.

After the photocatalytic reaction, the Cu-2 sample showed an additional band in its C 1s spectrum related to C-H bond at 286.1 eV (**Figure 12d**). This band could be ascribed to the residual methoxide, which is an intermediate of the photocatalytic reaction [66]. This species could be adsorbed on the edge sites of the film forming CH_3O-Cu^{2+} [67]. Moreover, the intensity of the signal at 532.1 eV grew after the reaction due to the presence of hydroxides (O-H), carbonates (CO_3^{2-}) [68], or oxygen-containing hydrocarbons (CH_3O-Cu^{2+}) [69], while the signal related to OVs at 531.0 eV disappeared after photocatalytic CO_2 reduction, probably because to the partial carbonation of the photocatalyst after the test (**Figure 12e**). The results indicated that OVs acted as an active site for CO_2 adsorption. It is also possible to observe an additional band around 934.8 eV related to the partial carbonation of the CuO [46, 70], which suggested the formation of intermediates monodentate and bidentate carbonate species. The Na 1s signal, which was originated from the substrates, was studied thoroughly.

The reference spectra showed a central peak at 1071.2 eV corresponding to Na-O bond present in Na_2O (**Figure S11a, b)** [71, 72]. A new band around 1071.6 eV appeared in the Na 1s spectrum after the reaction, which was associated with the partial carbonation of Na_2O (**Figure S11c, d)** [72, 73]. The carbonation of Na-O suggested that this oxide acted as an additional active site for CO_2 adsorption, enhancing the global efficiency.

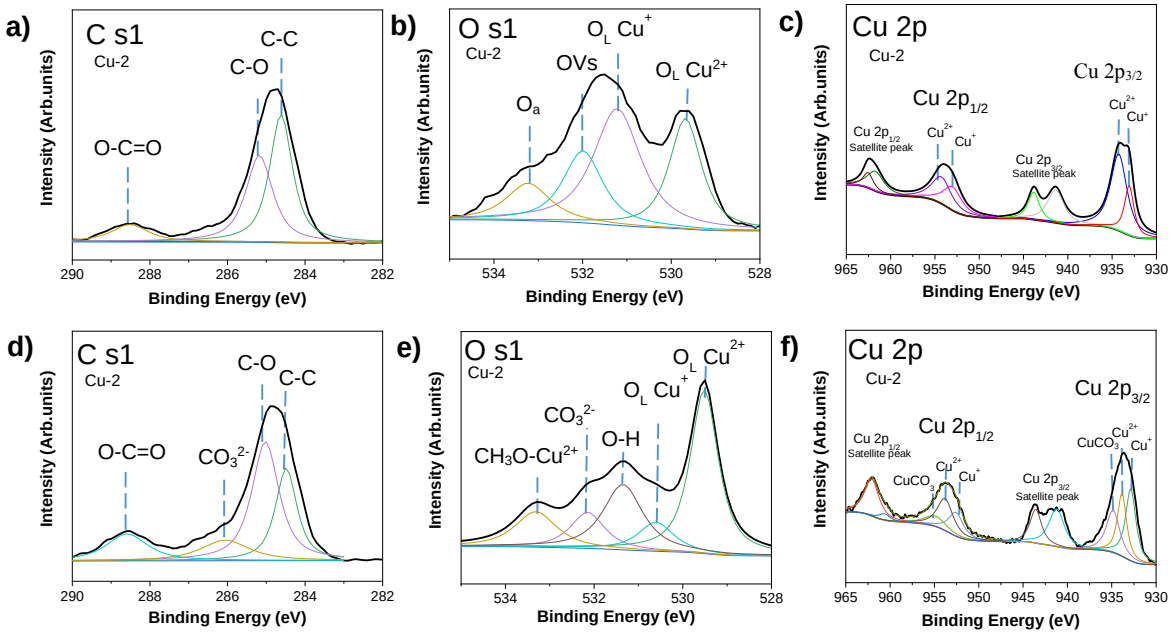

Figure 12. XPS spectra of Cu-2 film before and after the photocatalytic reaction for the element of a) and d) C 1s, b) and e) O 1s, c) and f) Cu 2p, respectively.

The surface analysis of Ni-3 before and after CO_2 reduction is shown in **Figure 13**. The C 1s spectrum of the film shows peaks at 284.4, 285.2, and 288.5 eV attributed to *sp*2 carbon components C–C, C-O, and O-C=O bonds, respectively (**Figure 13a**) [14, 55, 56]. These signals were due to the CO_2 adsorbed from the air. For the O1s spectrum (**Figure 13b),** three peaks were observed at 529.7, 530.5, and 531.4 eV, related to Ni^{2+} (O_L Ni^{2+}) of NiO [74], to oxygen adsorbed on the surface with low coordination (O_a) [61, 75], and Ni^{3+} (O_L Ni^{3+}) of Ni_2O_3 [76, 77], respectively. The Ni 2p spectrum in **Figure 13c** displays two edge splits by

spin-orbital coupling: i) the Ni $2p_{3/2}$ peak at 854.7 eV related with NiO [78], and ii) the $2p_{3/2}$ central peak at 855.7 eV and its satellite at 860.2 eV, evidencing the existence of Ni_2O_3 on the surface [77, 78]. This observation also explained the enhanced performance in PL (**Figure 6**) and the *p*-type characteristic of the sample, as shown in the transient chronoamperometry tests (**Figure 11**). After CO_2 reduction, Ni-3 film presented additional bands in the C 1s, Ni 2p, and O 1s spectra related to the presence of hydroxides, carbonates, or oxygen-containing hydrocarbons (**Figure 13d, e**) [68, 79]. The Ni 2p spectrum after the reaction showed the $2p_{3/2}$ at 855.7 eV, the $2p_{1/2}$ at 872.6 eV, and its satellite peak at 860.2 and 879.5 eV, respectively (**Figure 13f**). Also, additional bands in the O 1s spectrum were observed at 856.7 and 866.1 eV, suggesting the conversion of NiO to $Ni(OH)_2$ after the reaction [80]. According to these results, the formation $Ni(OH_2)$ species during the photocatalytic reaction promoted the hydroxylation of NiO phase and the dissolution of the NiO/Ni_2O_3 heterostructure. As a result, the photoreduction of CO_2 activity deactivated with time, as shown in **Figure 10**, which eventually decreased the charge transfer in the Ni-3 sample.

According to the results, the decrease of CH_4 or CO production by Cu-1 and Ni-3, respectively, was due to the carbonation occurred on the surface of the catalyst as discussed with **Figures 12** and **13**. These experiments gave a strong indication that no degradation occurred during CO_2 photoreduction reaction.

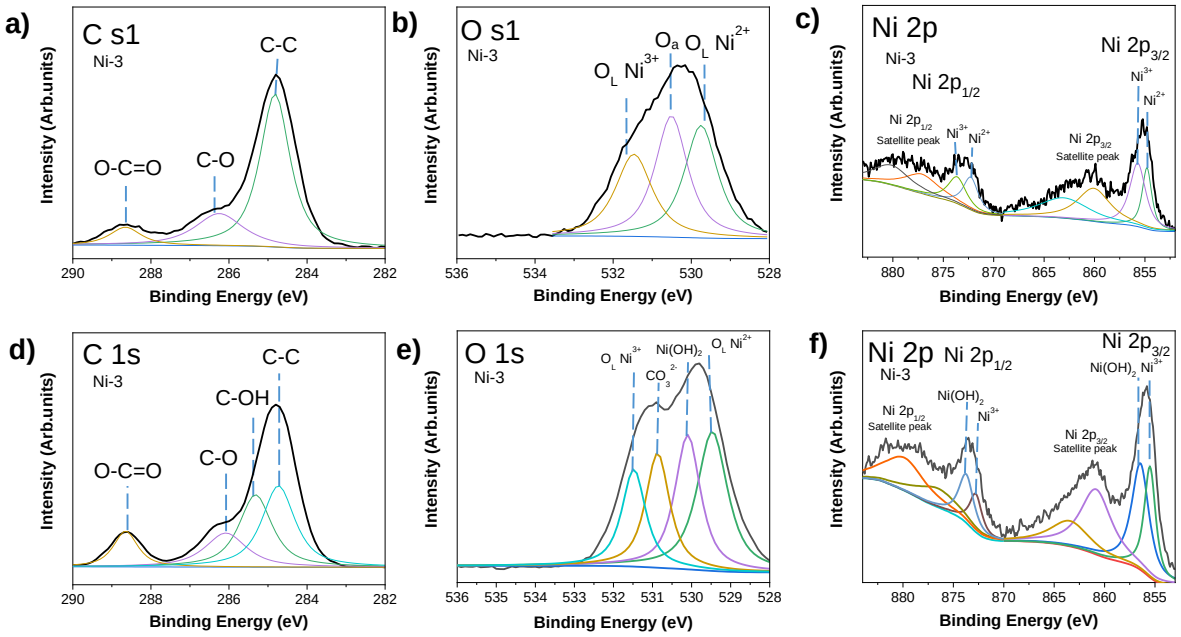

Figure 13. XPS spectra of Ni-3 film before and after the photocatalytic CO_2 reduction for the element of a) and d) C 1s, b) and e) O 1s, c) and f) Ni 2p, respectively.

3.5. Stability test

The stability of the optimized samples (Cu-2 and Ni-3) was conducted under a similar photocatalytic reduction of CO_2. Three consecutive runs were performed on each sample (**Figure S12**). The results revealed that copper oxides exhibited a stable CH_4 production after three consecutive cycles, whereas the CO production of Ni-3 coating deteriorated in each cycle significantly, around 28% in the second cycle and 42% in the third one.

After the tests, the morphology of the Cu-2 and Ni-3 samples was analyzed by SEM. After the test, the Ni-3 sample maintained its morphology of polyhedral particles, while the particles with flake morphology were not observed, as is shown in **Figure S13a**. On the contrary, the morphology of Cu-2 bars changed after the photocatalytic evaluation. **Figure S13b** shows that after the reaction, the bars tended to agglomerate with each other forming elongated

agglomerates, which could be related to the loss of active sites for the photocatalytic CO_2 reduction.

3.6. Photocatalytic CO_2 reduction in a batch reactor

The photocatalytic activity of the samples with the best performance in the continuous system (Cu-2 and Ni-3) was also evaluated in a batch reactor to investigate the formation of liquid solar fuels under LED visible-light (**Figure S14**). Both samples produced HCOOH and CH_3OH; however, traces of CH_2O were identified in both samples (<2 μmol g^{-1} h^{-1}). Cu-2 sample exhibited higher CH_3OH production (177 μmol g^{-1} h^{-1}) than Ni-3 sample (5 μmol g^{-1} h^{-1}). These results could be attributed to efficient charge transfer in the CuO/Cu_2O film, high affinity of CO_2 adsorption, and the type of carbonate adsorbed species. Formic acid was also identified, which production was better in the Ni-3 sample (4245 μmol g^{-1} h^{-1}) compared with the Cu-2 sample (1450 μmol g^{-1} h^{-1}). These results confirm that the charge transfer efficiency and the CO_2 affinity are important factors to obtain hydrocarbons of higher molecular weights, since the use of NiO/Ni_2O_3 promote the formation of CO and HCOOH in the gas and liquid phases, respectively. Because these reactions just required two electrons to occur. The liquid products obtained from the photocatalytic evaluation of Cu-2 were confirmed and monitored by ^1H NMR (**Figure S15**). It was possible to corroborate the presence of methanol at 3.6 ppm in the sample and ethanol at 3.4 ppm. The observed concentrations are of the same order of magnitude as those liquid samples analyzed using GC. With this technique was not possible to identify the presence of CH_2O and HCOOH due to its detection limit (<2 ppm). Also, for comparative purposes, TiO_2 P-25 was evaluated under the same experimental conditions in the liquid phase. This reference sample only promoted the formation of HCOOH

(81 μmol g^{-1} h^{-1}), and other products were not detected. These results confirm the better photocatalytic activity of the earth-abundant photocatalyst proposed in this work.

3.7. Photocatalytic mechanism

The photocatalytic proposed for the CO_2 reduction mechanism on the surface of the Cu-2 and Ni-3 sample was illustrated in **Figure 14**. The theoretical potential of the conduction band of Cu_2O is more negative (-0.4 eV) than that of CuO (0.3 eV). Therefore, the electrons (e^-) of the valence band of Cu_2O are transferred to the conduction band of CuO generating a hole (h^+) in the first band, which reacts with the CO_2 and H_2O molecules adsorbed on its surface (**Figure 14a I**). In the proposed mechanism, the presence of Na_2O in the substrate, represented as a gray circle, provides an extra active site where the CO_2 adsorption occurs. This phenomenon was corroborated by analyzing the Na1s spectrum after and before the photocatalytic reaction, which evidences the formation of Na_2CO_3 after its interaction with the CO_2 molecule. Once the carbonates are captured on the photocatalytic device (Metal oxides/Substrate), the photogenerated electrons can proceed to reduce this species onto C1 products (**Figure 14a II**). In an initial step, the CO_2 molecule is adsorbed on the heterostructure surface, forming mono and bidentate species (as it was previously demonstrated by FTIR analysis); at the beginning of the reaction, electrons are transferred from Cu_2O to CuO and then to the adsorbed species (**Figure 14a III**). CO_2 can be physisorbed as a linear molecule or chemisorbed as a partly charged $CO_2^{\delta-}$ species via interactions with surface atoms. Three different coordination systems have been proposed for CO_2 molecules adsorbed on a photocatalyst surface:

1. First, the positively charged carbon atom may behave as a Lewis acid, accepting electrons from Lewis's base centers such as oxide ions and forming a carbonate-like species (**Figure S16a**).

2. Second, as illustrated in **Figure S16b**, the oxygen atoms in CO_2 have lone pairs of electrons that can be transported to the Lewis acid centers on the surface.

3. Thirdly, the oxygen and carbon atoms of the CO_2 molecule can act as electron donors and acceptors, resulting in a mixed coordination structure, as is shown in **Figure S16c**.

The mechanism for the formation of C1 products such as CH_3OH and CH_4 can occur by different routes [50]. The first route is by forming *CO and subsequent hydrogenation to *CHO, *CH_2O (which desorbs as HCHO), and *CH_3O (methoxy). Additionally, the intermediate *CH_3O may convert to CH_4, leaving *O on the surface, which would evolve into H_2O. Another way to form CH_4 also originates from the formation of *CO on the surface. This intermediate is hydrogenated to form *COH on the surface, subsequently dehydrated to form *C. Via step-by-step hydrogenation, this intermediate forms CH_4. An additional mechanism that differs from these two pathways could also occur. Rather than forming *CO initially, this pathway begins with the bidentate coordination of $CO_2{}^{*-}$ via the oxygen atoms, followed by the generation of HCO_2, H_2OCO*, and *CHO. This mechanism is referred to as the carbene pathway [50]. On the other hand, the Ni-based coatings only produce CO and HCOOH due to their lower affinity to adsorbed CO_2. Based on the results, it is proposed that the reaction mechanism follows the carbene route since it was possible to identify by XPS residual species such as CH_3O-Cu^{2+}, which is an intermediate in the production of methanol and methane.

On the other hand, the proposed mechanism of the photocatalytic reactions that take place in the Ni-3 coating is illustrated in **Figure 14b**. Like that of the Cu-2 film, the photoreduction process begins once CO_2 is adsorbed. Electrons are transferred from the conduction band of NiO to Ni_2O_3 according to their theoretical CB potentials, e.g., -0.34 and 0.07 V vs NHE, respectively. In this mechanism, NiO acts as an electron donor in which the photoexcited

electrons could be transferred to the CO_2 adsorbed on the Ni_2O_3 surface, producing CO following the pathway for C_1 products [81]. Due to the relatively low amount of photogenerated electrons in the NiO conduction band, a small amount of these is transferred to the Ni_2O_3. Then, the electrons photogenerated in Ni_2O_3 (small black particles) are transferred to the Ni-O = C = O species (**Figure 14b I**). According to the results shown in the FTIR spectrum, the lower affinity for CO_2 on NiO could promote a rapid desorption of carbonate species, which favored the formation of CO and HCOOH in the gas and liquid phase, respectively. Furthermore, the minor current density indicates that the NiO/Ni_2O_3 heterostructure did not provide enough electrons for CO_2 photoreduction to methane or methanol. Additionally, the presence of Ni_2O_3 could favor de charge transfer due to the formation of a type-II heterostructure, while the presence of Na_2O, also help to prevents the re-oxidation of the products (**Figure 14b II.**). A closer view of this mechanism is shown in **Figure 14b III**, in which the CO or HCOOH production starts when the CO_2 molecule is adsorbed on the NiO surface. Of note, when the surface of NiO interacts with water, it could form $Ni(OH)_2$ on the surface, which would reduce the photocatalytic activity of the heterostructure.

In both mechanisms, the H_2 generation is suppressed by the higher affinity of CO_2 for the protons (H^+) generated in the valence band of the semiconductors, as is shown in **Figure S5c**.

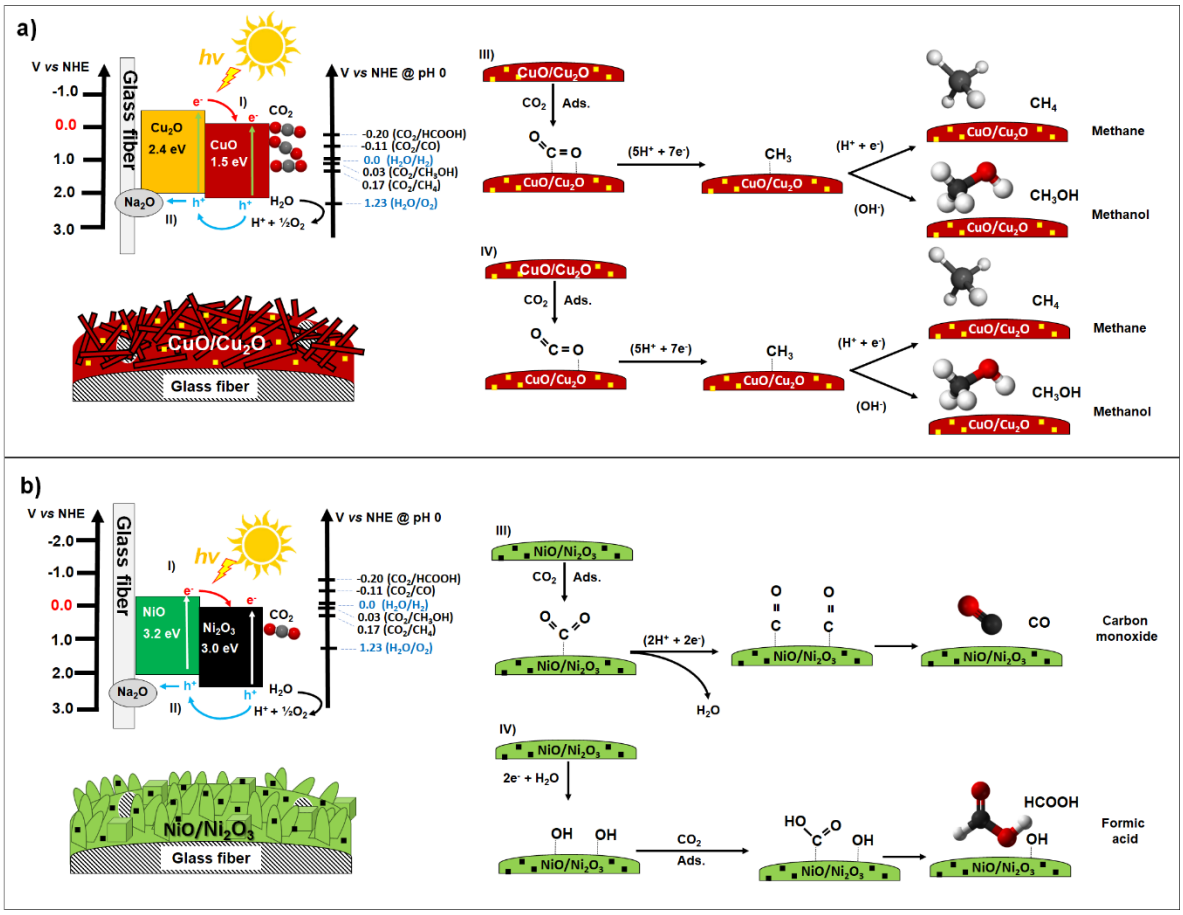

Figure 14. Schematic diagram of proposed mechanisms for the photocatalytic CO_2 reduction in a) Cu-2 (CuO/Cu_2O) and b) Ni-3 (NiO/Ni_2O_3) samples.

4. Conclusions

Heterostructured Cu_xO (x = 1 and 2) and Ni_xO_y (x=1 and 2, y=1 and 3) coatings on flexible substrates were obtained by an *in-situ* microwave-hydrothermal method using glucose as a reductive agent at 80 °C for 1 h. The coatings exhibited photocatalytic activity to convert CO_2 into value-added products, such as CH_4 and CO in a continuous system under UV-Visible light and CH_3OH and HCOOH in a batch reactor under visible light. The CuO/Cu_2O coatings were selective towards CH_4 and CH_3OH; meanwhile NiO/Ni_2O_3 preferably produced CO and HCOOH.

The highest CH_4 production with CuO/Cu_2O coatings was 94 μmol g^{-1} h^{-1}, which was 32 times higher than previous studies in the literature using a simple or binary oxides of coatings. The superior CO_2 photoreduction was attributed to the high affinity for CO_2 and an efficient charge transfer in the CuO/Cu_2O heterostructure. On the other hand, Ni_xO_y coatings showed a much lower affinity to CO_2 adsorption and less efficient charge transfer than CuO/Cu_2O coatings, producing lighter products: CO in the continuous reactor and HCOOH in the batch reactor. Also, the stability in these samples was lower than the copper oxide coatings due to the conversion of NiO/Ni_2O_3 to $NiO/Ni(OH)_2$, as evidenced in XPS.

5. Acknowledgments

The authors wish to thank CONACYT for financial support for this research through the following projects: Cátedras CONACYT 1060, CONACYT-FC-1725, and Paradigmas y Fronteras de la Ciencia 320379. Also, the authors thank to UANL for its support by PAICYT projects. Manuel Alejandro Ávila López wants to thank CONACYT for the PhD scholarship. In addition, the authors want to thank to M.C Luis Gerardo Silva Vidaurri from CIMAV for his help with the XPS analysis.

UK Catalysis Hub is kindly thanked for resources and support provided via the membership of the UK Catalysis Hub Consortium and funded by current EPSRC grants: EP/R026939/1 and EP/R026815/1. The authors would like to thank Dr. Leila Negahdar, Dr. June Callison, Dr. Nitya Ramanan, and Prof. Andrew M. Beale for their great help and support during the DRIFTS experiments. The authors also thank the financial support provided by the UK Engineering and Physical Sciences Research Council (EP/K021796/1). They are also grateful for the support provided by the Research Centre for Carbon Solutions (RCCS) and the Buchan Chair in Sustainable Energy Engineering at Heriot-Watt University.

6. References

[1] J. Bradshaw, Z. Chen, A. Garg, D. Gomez, H.-H. Rogner, D. Simbeck, R. Williams, in: B. Metz, O. Davidson, de C. Heleen, M. Loos, L. Meyer (Eds.), Carbon Dioxide Capture and Storage, Intergovernmental Panel on Climate Change, Canada, 2009, pp. 75–104.

[2] Q. Wang, J. Luo, Z. Zhong, A. Borgna, CO2 capture by solid adsorbents and their applications: current status and new trends, Energy Environ. Sci. 4 (2011) 42–55. https://doi.org/10.1039/C0EE00064G

[3] Y. Wang, L. Zhao, A. Otto, M. Robinius, D. Stolten, A Review of Post-combustion CO2 Capture Technologies from Coal-fired Power Plants, Energy Procedia 114 (2017) 650–665. https://doi.org/10.1016/j.egypro.2017.03.1209

[4] W. Tu, Y. Zhou, Z. Zou, Photocatalytic Conversion of CO2 into Renewable Hydrocarbon Fuels: State-of-the-Art Accomplishment, Challenges, and Prospects, Adv. Mater 26 (2014) 4607-4626. https://doi.org/10.1002/adma.201400087

[5] Ž. Kovačič, B. Likozar, M. Huš, Photocatalytic CO2 Reduction: A Review of Ab Initio Mechanism, Kinetics, and Multiscale Modeling Simulations, ACS Catal. 10 (2020) 14984-15007. https://doi.org/10.1021/acscatal.0c02557

[6] J. Fu, K. Jiang, X. Qiu, J. Yu, M. Liu, Product selectivity of photocatalytic CO2 reduction reactions, Mater. Today 32 (2020) 222-243. https://doi.org/10.1016/j.mattod.2019.06.009

[7] W.A. Thompson, A. Olivo, D. Zanardo, G. Cruciani, F. Menegazzo, M. Signoretto, M.M. Maroto-valer, Systematic study of TiO2/ZnO mixed metal oxides for CO2 photoreduction, RSC Adv 9 (2019) 21660–21666. https://doi.org/10.1039/C9RA03435H

[8] Z.-Y. Wang, H.-C. Chou, J.C.S. Wu, D.P. Tsai, G. Mul, CO2 photoreduction using NiO/InTaO4 in optical-fiber reactor for renewable energy, Appl. Catal. A 380 (2010) 172–177. https://doi.org/10.1016/j.apcata.2010.03.059

[9] A.E. Nogueira, J.A. Oliveira, G.T.S.T. da Silva, C. Ribeiro, Insights into the role of CuO in the CO2 photoreduction process, Sci. Rep. 9 (2019) 1316. https://doi.org/10.1038/s41598-018-36683-8

[10] Z. Xiong, Z. Lei, C.-C. Kuang, X. Chen, B. Gong, Y. Zhao, J. Zhang, C. Zheng, J.C.S. Wu, Selective photocatalytic reduction of CO2 into CH4 over Pt-Cu2O TiO2 nanocrystals: The interaction between Pt and Cu2O cocatalysts, Appl. Catal. B Environ. 202 (2017) 695–703. https://doi.org/10.1016/j.apcatb.2016.10.001

[11] J.Y. Do, B.S. Kwak, S.-M. Park, M. Kang, Effective Carbon Dioxide Photoreduction over Metals (Fe-, Co-, Ni-, and Cu-) Incorporated TiO2/Basalt Fiber Films, Int. J. Photoenergy 2016 (2016) 1–12. https://doi.org/10.1155/2016/5195138

[12] J.Z.Y. Tan, Y. Fernández, D. Liu, M. Maroto-Valer, J. Bian, X. Zhang, Photoreduction of CO2 using copper-decorated TiO2 nanorod films with localized surface plasmon behavior, Chem. Phys. Lett. 531 (2012) 149–154. https://doi.org/10.1016/j.cplett.2012.02.016

[13] J.-C. Wang, L. Zhang, W. Fang, J. Ren, Y.-Y. Li, H. Yao, J. Wang, Z. Li, Enhanced Photoreduction CO2 Activity over Direct Z-Scheme α-Fe2O3/Cu2O Heterostructures under Visible Light Irradiation, ACS Appl. Mater. Interfaces 7 (2015) 8631–8639. https://doi.org/10.1021/acsami.5b00822

[14] M.A. Ávila-López, E. Luévano-Hipólito, L.M. Torres-Martínez, CO2 adsorption and its visible-light-driven reduction using CuO synthesized by an eco-friendly sonochemical method, J. Photochem. Photobiol. A Chem. 382 (2019) 111933. https://doi.org/10.1016/j.jphotochem.2019.111933

[15] Y. Li, W.-N. Wang, Z. Zhan, M.-H. Woo, C.-Y. Wu, P. Biswas, Photocatalytic reduction of CO2 with H2O on mesoporous silica supported Cu/TiO2 catalysts, Appl. Catal. B Environ. 100 (2010) 386–392. https://doi.org/10.1016/j.apcatb.2010.08.015

[16] Y. Yan, Y. Yu, C. Cao, S. Huang, Y. Yang, X. Yang, Y. Cao, Enhanced photocatalytic activity of TiO2–Cu/C with regulation and matching of energy levels by carbon and copper for photoreduction of CO2 into CH4, CrystEngComm 18 (2016) 2956–2964. https://doi.org/10.1039/C6CE00117C

[17] M. Tahir, B. Tahir, N. A. S. Amin, A. Muhammad, Photocatalytic CO2 methanation over NiO/In2O3 promoted TiO2 nanocatalysts using H2O and/or H2 reductants, Energy Conversion and Management 119 (2016) 368-378. https://doi.org/10.1016/j.enconman.2016.04.057

[18] C. Han, R. Zhang, Y. Ye, L. Wang, Z. Ma, F. Su, H. Xie, Y. Zhou, P.K. Wong, L. Ye, Chainmail co-catalyst of NiO shell-encapsulated Ni for improving photocatalytic CO2 reduction over g-C3N4, J. Mater. Chem. A 7 (2019) 9726–9735. https://doi.org/10.1039/C9TA01061K

[19] A.M. Huerta-Flores, E. Luévano-Hipólito, Leticia M. Torres-Martínez, A.T. Sánchez, Photocatalytic H2 production and CO2 reduction on Cu, Ni‑ doped ZnO: effect of metal doping and oxygen vacancies, J. Mater. Sci. Mater. Electron. (2019) 1–13. https://doi.org/10.1039/C9TA01061K

[20] L. Liu, H. Zhao, J.M. Andino, Y. Li, Photocatalytic CO2 Reduction with H2O on TiO2 Nanocrystals: Comparison of Anatase, Rutile, and Brookite Polymorphs and Exploration of Surface Chemistry, Catal. ACS 2 (2012) 1817–1828. https://doi.org/10.1021/cs300273q

[21] M. Tasbihi, F. Fresno, U. Simon, I.J. Villar-García, V. Pérez-Dieste, C. Escudero, V.A. de la Peña O'Shea, On the selectivity of CO2 photoreduction towards CH4 using Pt/TiO2 catalysts supported on mesoporous silica, Appl. Catal. B Environ. 239 (2018) 68–76. https://doi.org/10.1016/j.apcatb.2018.08.003

[22] B.S. Kwak, K.M. Kim, S.-M. Park, M. Kang, Synthesis of basalt fiber@Zn1-xMgxO core/shell nanostructures for selective photoreduction of CO2 to CO, Appl. Surf. Sci. 407 (2017) 109–116. https://doi.org/10.1016/j.apsusc.2017.02.178

[23] M. Tahir, B. Tahir, N.A.S. Amin, A. Muhammad, Photocatalytic CO2 methanation over NiO/In2O3 promoted TiO2 nanocatalysts using H2O and/or H2 reductants, Energy Convers. Manag. 119 (2016) 368–378. https://doi.org/10.1016/j.enconman.2016.04.057

[24] N. Jantarasorn, O. Mekasuwandumrong, P. Kelly, P. Praserthdam, Reactive Magnetron Sputter Deposition of Copper on TiO2 Support for Photoreduction of CO2 to CH4, IOP Conf. Ser. Mater. Sci. Eng. 559 (2019) 012017. https://doi.org/10.1088/1757-899X/559/1/012017

[25] J.Y. Do, Y. Im, B.S. Kwak, S.-M. Park, M. Kang, Dramatic CO2 photoreduction with H2O vapors for CH4 production using the TiO2 (bottom)/Fe–TiO2 (top) double-layered films, Ceram. Int. 42 (2016) 5942–5951. https://doi.org/10.1016/j.cej.2015.03.066

[26] Y. Im, S.-M. Park, M. Kang, Effect of Ca/Ti Ratio on the Core-Shell Structured

CaTiO3@basalt Fiber for Effective Photoreduction of Carbon Dioxide, Bull. Korean Chem. Soc. 38 (2017) 397–400. https://doi.org/10.1002/bkcs.11100

[27] A.A. Beigi, S. Fatemi, Z. Salehi, Synthesis of nanocomposite CdS/TiO2 and investigation of its photocatalytic activity for CO2 reduction to CO and CH4 under visible light irradiation, J CO2 Util. 7 (2014) 23–29. https://doi.org/10.1016/j.jcou.2014.06.003

[28] J. Kim, J.Y. Do, N.K. Park, S.J. Lee, J.P. Hong, M. Kang, Photoreduction of CO2 into CH4 using Bi2S3-TiO2 double-layered dense films, Korean J. Chem. Eng. 35 (2018) 1089–1098. https://doi.org/10.1007/s11814-018-0007-y

[29] A. Olivo, E. Ghedini, M. Signoretto, Matteo Compagnoni, Ilenia Rossetti, Liquid vs. Gas Phase CO2 Photoreduction Process: Which Is the Effect of the Reaction Medium?, Energies 10 (2017) 1394. http://dx.doi.org/10.3390/en10091394

[30] A. Olivo, D. Zanardo, E. Ghedini, F. Menegazzo, M. Signoretto, Solar Fuels by Heterogeneous Photocatalysis: From Understanding Chemical Bases to Process Development, Chemengineering 2 (2018) 42. http://dx.doi.org/10.3390/chemengineering2030042

[31] T. Baran, A. Visibile, M. Busch, X. He, S. Wojtyla, S. Rondinini, A. Minguzzi, A. Vertova, Copper Oxide-Based Photocatalysts and Photocathodes: Fundamentals and Recent Advances. Molecules 26 (2021) 7271. https://doi.org/10.3390/molecules26237271

[32] A. I. Vaizogullar, Facile preparation and characterization of NiO/Ni2O3-decorated nanoballs and mixed phase CdS nano rods (CdS&NiO/Ni2O3) for effective photocatalytic decomposition of Congo red under visible light irradiation, J. Dispers. Sci. Technol. 42 (2021) 1408-1418. https://doi.org/10.1080/01932691.2020.1814804

[33] M.A. Ávila-López, E. Luévano-Hipólito, L.M. Torres-Martínez, CuO coatings on glass fibers: a hybrid material for CO2 adsorption and photocatalytic reduction to solar fuels,

J. Mater. Sci. Mater. Electron. 32 (2020) 11336–11337. https://doi.org/10.1007/s10854-020-03955-x

[34] W. A. Thompson, A. Olivo, D. Zanardo, G. Cruciani, F. Menegazzo, M. Signoretto, M. Mercedes Maroto-Valer, Systematic study of TiO2/ZnO mixed metal oxides for CO2 photoreduction, RSC Advances 9 (2019) 21660-21666. https://doi.org/10.1039/C9RA03435H

[35] A. Soman, Y. Qiu, Q. Chan Li, HPLC-UV Method Development and Validation for the Determination of Low Level Formaldehyde in a Drug Substance, J. Chromatogr. Sci. 46 (2008) 461–465. https://doi.org/10.1093/chromsci/46.6.461

[36] D. Hasan, I. Mahmood, I. Ahmad, F. Aziz, I. Ahmad, Development of an HPLC Method for Formic Acid Analysis through Peak Exclusion Approach, Sains Malaysiana 48 (2019) 1011–1018. http://dx.doi.org/10.17576/jsm-2019-4805-09

[37] S. Banerjee, D. Chakravorty, Optical absorption by nanoparticles of Cu2O, Europhys. Lett. 52 (2000) 468–473. https://dx.doi.org/10.1209/epl/i2000-00461-5

[38] M. Hashem, E. Saion, N.M. Al-hada, H.M. Kamari, A.H. Shaari, Z.A. Talib, S.B. Paiman, M.A. Kamarudeen, Results in Physics Fabrication and characterization of semiconductor nickel oxide (NiO) nanoparticles manufactured using a facile thermal treatment, Results Phys. 6 (2016) 1024–1030. https://doi.org/10.1016/j.rinp.2016.11.031

[39] A. Molla, M. Sahu, S. Hussain, Synthesis of Tunable Band Gap Semiconductor Nickel Sulphide Nanoparticles: Rapid and Round the Clock Degradation of Organic Dyes Sci. Rep. 6 (2016) 26034. https://doi.org/10.1038/srep26034

[40] A. Renaud, B. Chavillon, L. Cario, L. Le Pleux, N. Szuwarski, Y. Pellegrin, E. Blart, E. Gautron, F. Odobel, S. Jobic, Origin of the Black Color of NiO Used as Photocathode in pType Dye-Sensitized Solar Cell, J. Phys. Chem. C 117 (2013) 22478–22483. https://doi.org/10.1021/jp4055457

[41] X. Zhao, P. Wang, Z. Yan, N. Ren, Room temperature photoluminescence properties of CuO nanowire arrays, Opt. Mater. 42 (2015) 544–547. https://doi.org/10.1016/j.optmat.2014.12.032

[42] X.X. Jiang, X. De Hu, M. Tarek, P. Saravanan, R. Alqadhi, S.Y. Chin, M.M. Rahman Khan, Tailoring the properties of g-C3N4 with CuO for enhanced photoelectrocatalytic CO2 reduction to methanol, J. CO2 Util. 40 (2020) 101222. https://doi.org/10.1016/j.jcou.2020.101222

[43] L. Kumari, W.Z. Li, C.H. Vannoy, R.M. Leblanc, D.Z. Wang, Vertically aligned and interconnected nickel oxide nanowalls fabricated by hydrothermal route, Cryst. Res. Technol. 44 (2009) 495–499. https://doi.org/10.1002/crat.200800583

[44] H. Du, C.T. Williams, A.D. Ebner, J.A. Ritter, In Situ FTIR Spectroscopic Analysis of Carbonate Transformations during Adsorption and Desorption of CO2 in K-Promoted HTlc Chem. Mater. 22 (2010) 3519–3526. https://doi.org/10.1021/cm100703e

[45] Y. Liu, Y. Yang, Q. Sun, Z. Wang, B. Huang, Y. Dai, X. Qin, X. Zhang, Chemical Adsorption Enhanced CO2 Capture and Photoreduction over a Copper Porphyrin Based Metal Organic Framework, ACS Appl. Mater. Interfaces 5 (2013) 7654–7658. https://doi.org/10.1021/am4019675

[46] A. Hakim, T.S. Marliza, N.M. Abu Tahari, R.W.N. Wan Isahak, R.M. Yusop, W.M. Mohamed Hisham, A.M. Yarmo, Studies on CO2 Adsorption and Desorption Properties from Various Types of Iron Oxides (FeO, Fe2O3, and Fe3O4), Ind. Eng. Chem. Res. 55 (2016) 7888–7897. https://doi.org/10.1021/acs.iecr.5b04091

[47] W.N.R.W. Isahak, Z.A.C. Ramli, M.W. Ismail, K. Ismail, R.M. Yusop, M.W.M. Hisham, M.A. Yarmo, Adsorption–desorption of CO2 on different type of copper oxides surfaces: Physical and chemical attractions studies, J. CO2 Util. 2 (2013) 8–15. https://doi.org/10.1016/j.jcou.2013.06.002

[48] L. Liu, C. Zhao, J. Xu, Y. Li, Integrated CO2 capture and photocatalytic conversion by a hybrid adsorbent/photocatalyst material, Appl. Catal. B Environ. 179 (2015) 489–499. https://doi.org/10.1016/j.apcatb.2015.06.006

[49] Y. Kato, M. Yamamoto, M. Akatsuka, R. Ito, A. Ozawa, Y. Kawaguchi, T. Tanabe, T. Yoshida, Study on carbon dioxide reduction with water over metal oxide photocatalysts Surf. Interface Anal. 51 (2019) 40–45. http://dx.doi.org/10.1002/sia.6542

[50] S.N. Habisreutinger, L. Schmidt-Mende, J.K. Stolarczyk, Photocatalytic Reduction of CO2 on TiO2 and Other Semiconductors, Angew. Chemie Int. Ed. 52 (2013) 7372–7408. https://doi.org/10.1002/anie.201207199

[51] Manuel Alejandro Ávila-López, Stelios Gavrielides, Xiao Jiao Luo, Abah Ezra Ojoajogwu, Jeannie Z. Y. Tan, E. Luévano-Hipólito, Leticia M. Torres-Martínez, M. Mercedes Maroto-Valer, Comparative study of CO2 photoreduction using different conformations of CuO photocatalyst: Powder, coating on mesh and thin film, Journal of CO2 Utilization 50 (2021) 101588. doi.org/10.1016/j.jcou.2021.101588

[52] E. Korovin, D. Selishchev, D. Kozlov, Photocatalytic CO2 Reduction on the TiO2 P25 Under the High Power UV-LED Irradiation, Top. Catal. 59 (2016) 1292–1296. https://link.springer.com/article/10.1007/s11244-016-0651-6

[53] N. Põldme, L. O'Reilly, I. Fletcher, J. Portoles, I. V. Sazanovich, M. Towrie, C. Long, J.G. Vos, M.T. Pryce, E.A. Gibson, Photoelectrocatalytic H2 evolution from integrated photocatalysts adsorbed on NiO, Chem. Sci. 10 (2019) 99–112. https://doi.org/10.1039/C8SC02575D

[54] M. Fingerle, S. Tengeler, W. Calvet,z W. Jaegermann, T. Mayer, Sputtered Nickel Oxide Thin Films on n-Si(100)/SiO2 Surfaces for Photo-Electrochemical Oxygen Evolution Reaction (OER): Impact of Deposition Temperature on OER Performance and on Composition before and after OER, J. Electrochem. Soc. 167 (2020) 136514.

[55] H. Jensen, A. Soloviev, Z. Li, E.G. Søgaard, XPS and FTIR investigation of the surface properties of different prepared titania nano-powders, Appl. Surf. Sci. 246 (2005) 239–249. https://doi.org/10.1016/j.apsusc.2004.11.015

[56] Y. Wang, Y. Jin, M. Jia, Ultralong Fe3O4 nanowires embedded graphene aerogel composite anodes for lithium ion batteries, Mater. Lett. 228 (2018) 395–398. https://doi.org/10.1016/j.matlet.2018.06.077

[57] Y. Min, T. Wang, Y. Chen, Microwave-assistant synthesis of ordered CuO microstructures on Cu substrate, Appl. Surf. Sci. 257 (2010) 132–137. https://doi.org/10.1016/j.apsusc.2010.06.049

[58] Y. Wang, Y. Lü, W. Zhan, Z. Xie, Q. Kuang, L. Zheng, Synthesis of porous Cu2O/CuO cages using Cu-based metal–organic frameworks as templates and their gas-sensing properties, J. Mater. Chem. A 3 (2015) 12796–12803. https://doi.org/10.1039/C5TA01108F

[59] H. Yu, J. Li, Y. Zhang, S. Yang, K. Han, F. Dong, T. Ma, H. Huang, Three-in-One Oxygen Vacancies: Whole Visible-Spectrum Absorption, Efficient Charge Separation, and Surface Site Activation for Robust CO 2 Photoreduction, Angew. Chemie - Int. Ed. 58 (2019) 3880–3884. https://doi.org/10.1002/anie.201813967

[60] Z.P. Nie, D.K. Ma, G.Y. Fang, W. Chen, S.M. Huang, Concave Bi2WO6 nanoplates with oxygen vacancies achieving enhanced electrocatalytic oxygen evolution in near-neutral water, J. Mater. Chem. A 4 (2016) 2438–2444. https://doi.org/10.1039/C5TA09536K

[61] S. Jaiswar, K.D. Mandal, Evidence of Enhanced Oxygen Vacancy Defects Inducing Ferromagnetism in Multiferroic CaMn7O12 Manganite with Sintering Time, J. Phys. Chem. C 121 (2017) 19586–19601. https://doi.org/10.1021/acs.jpcc.7b05415

[62] Y. Zhao, M. Ikram, J. Zhang, K. Kan, H. Wu, W. Song, L. Li, K. Shi, Outstanding Gas Sensing Performance of CuO-CNTs Nanocomposite Based on Asymmetrical Schottky Junctions, Appl. Surf. Sci. 428 (2018) 415–421. http://dx.doi.org/10.1016/j.apsusc.2017.09.173

[63] J. Park, K. Lim, R.D. Ramsier, Y.-C. Kang, Spectroscopic and Morphological Investigation of Copper Oxide Thin Films Prepared by Magnetron Sputtering at Various Oxygen Ratios, Bull. Korean Chem. Soc. 32 (2011) 3395–3399. http://dx.doi.org/10.5012/bkcs.2011.32.9.3395

[64] L. Yang, D. Chu, L. Wang, X. Wu, J. Luo, Synthesis and photocatalytic activity of chrysanthemum-like Cu2O/Carbon Nanotubes nanocomposites, Ceram. Int. 42 (2016) 2502–2509. https://doi.org/10.1016/j.ceramint.2015.10.051

[65] K. Ozawa, Y. Oba, K. Edamoto, Formation and characterization of the Cu2O overlayer on Zn-terminated ZnO(0 0 0 1), Surf. Sci. 603 (2009) 2163–2170. http://dx.doi.org/10.1016/j.susc.2009.04.027

[66] K. Habermehl-Ćwirzeń, J. Lahtinen, P. Hautojärvi, Methanol on Co(0 0 0 1): XPS, TDS, WF and LEED results, Surf. Sci. 598 (2005) 128–135. https://doi.org/10.1016/j.susc.2005.08.033

[67] J.M. Montero, M.A. Isaacs, A.F. Lee, J.M. Lynam, K. Wilson, The surface chemistry of nanocrystalline MgO catalysts for FAME production: an in situ XPS study of H2O, CH3OH and CH3OAc adsorption, Surf. Sci. 646 (2016) 170–178. https://doi.org/10.1016/j.susc.2015.07.011

[68] S. Röhe, K. Frank, A. Schaefer, A. Wittstock, V. Zielasek, A. Rosenauer, M. Bäumer, CO oxidation on nanoporous gold: A combined TPD and XPS study of active catalysts, Surf. Sci. 609 (2013) 106–112. http://dx.doi.org/10.1016/j.susc.2012.11.011

[69] B.K. Deka, K. Kong, J. Seo, D. Kim, Y. Park, H.W. Park, Controlled growth of CuO nanowires on woven carbon fibers and effects on the mechanical properties of woven carbon fiber/polyester composites, Compos. Part A Appl. Sci. Manuf. 69 (2015) 56–63. https://doi.org/10.1016/j.compositesa.2014.11.001

[70] Y. Wang, H. Xiang, C. Yang, D. Liu, Corrosion Resistance of Copper-bearing Duplex Stainless Steel in Culture Medium without and with Bacteria, J. Chinese Soc. Corros. Prot. 34 (2014) 558–565. https://doi.org/10.11902/1005.4537.2013.184

[71] S. Wu, Y. Qiao, K. Jiang, Y. He, S. Guo, H. Zhou, Tailoring Sodium Anodes for Stable Sodium-Oxygen Batteries, Adv. Funct. Mater. 28 (2018) 1706374. https://doi.org/10.1002/adfm.201706374

[72] D. McNulty, D. Noel Buckley, C. O'Dwyer, NaV2O5 from Sodium Ion-Exchanged Vanadium Oxide Nanotubes and Its Efficient Reversible Lithiation as a Li-Ion Anode Material, ACS Appl. Energy Mater. 2 (2019) 822–832. https://doi.org/10.1021/acsaem.8b01895

[72] P.C. Kao, J.Y. Wang, J.H. Lin, S.H. Chen, Enhancement of Electron Injection in Organic Light Emitting Diodes Using an Ultrathin Sodium Carbonate Buffer Layer, J. Electrochem. Soc. 157 (2010) 1–5. http://dx.doi.org/10.1149/1.3305947

[73] J.F. Moulder, W.F. Stickle, P.E. Sobol, K.D. Bomben, Handbook of X-Ray Photoelectron Spectroscopy, John Wiley & Sons, Ltd, Chichester, UK, 2005, pp. 50–51.

[74] V.V. Kaichev, A.Y. Gladky, I.P. Prosvirin, A.A. Saraev, M. Hävecker, A. Knop-Gericke, R. Schlögl, V.I. Bukhtiyarov, In situ XPS study of self-sustained oscillations in catalytic oxidation of propane over nickel, Surf. Sci. 609 (2013) 113–118. https://doi.org/10.1016/j.susc.2012.11.012

[75] S.-B. Lee, J.-H. Boo, W.-S. Ahn, XPS Studies of Oxygen Adsorption on Polycrystalline Nickel Surface, Bull. Korean Chem. Soc. 8 (1987) 358–362.

[76] Q. Liu, Q. Chen, Q. Zhang, Y. Xiao, X. Zhong, G. Dong, M.-P. Delplancke-Ogletree, H. Terryn, K. Baert, F. Reniers, X. Diao, In situ electrochromic efficiency of a nickel oxide

thin film: origin of electrochemical process and electrochromic degradation, J. Mater. Chem. C 6 (2018) 646–653. https://doi.org/10.1039/C7TC04696K

[77] H. Lin, B. Sun, H. Wang, Q. Ruan, Y. Geng, Y. Li, J. Wu, W. Wang, J. Liu, X. Wang, Unique 1D Cd1−xZnxS@O-MoS2/NiOx Nanohybrids: Highly Efficient Visible-Light-Driven Photocatalytic Hydrogen Evolution via Integrated Structural Regulation, Small 15 (2019) 1804115. https://doi.org/10.1002/smll.201804115

[78] N. Weidler, J. Schuch, F. Knaus, P. Stenner, S. Hoch, A. Maljusch, R. Schäfer, B. Kaiser, W. Jaegermann, X-ray Photoelectron Spectroscopic Investigation of Plasma-Enhanced Chemical Vapor Deposited NiOx, NiOx(OH)y, and CoNiOx(OH)y: Influence of the Chemical Composition on the Catalytic Activity for the Oxygen Evolution Reaction, J. Phys. Chem. C 121 (2017) 6455–6463. https://doi.org/10.1021/acs.jpcc.6b12652

[79] D.H. Kim, M.C. Jung, S.H. Cho, S.H. Kim, H.Y. Kim, H.J. Lee, K.H. Oh, M.W. Moon, UV-responsive nano-sponge for oil absorption and desorption, Sci. Rep. 5 (2015) 1–12. http://dx.doi.org/10.1038/srep12908

[80] S. Oswald, W. Brückner, XPS depth profile analysis of non-stoichiometric NiO films, Surf. Interface Anal. 36 (2004) 17–22. https://doi.org/10.1002/sia.1640

[81] L. Wang, W. Chen, D. Zhang, Y. Du, R. Amal, S. Qiao, J. Wu, Z. Yin, Surface strategies for catalytic CO2 reduction: from two-dimensional materials to nanoclusters to single atoms, Chem. Soc. Rev. 48 (2019) 5310–5349. https://doi.org/10.1039/c9cs00163h

Production of CH_4 and CO on Cu_xO and Ni_xO_y Coatings through CO_2 Photoreduction

Manuel Alejandro Ávila-López[1], Jeannie Z. Y. Tan[2], E. Luévano-Hipólito[3], Leticia M. Torres-Martínez[1,4,], M. Mercedes Maroto-Valer[2,*]*

[1] Universidad Autónoma de Nuevo León, Facultad de Ingeniería Civil-Departamento de Ecomateriales y Energía, Cd. Universitaria, C.P. 66455 San Nicolás de los Garza, NL, México.

[2] Research Centre for Carbon Solutions (RCCS), School of Engineering & Physical Sciences, Heriot-Watt University, Edinburgh, United Kingdom.

[3] CONACYT - Universidad Autónoma de Nuevo León, Facultad de Ingeniería Civil-Departamento de Ecomateriales y Energía, Cd. Universitaria, C.P. 66455 San Nicolás de los Garza, NL, México.

[4] Centro de Investigación en Materiales Avanzados, S. C. (CIMAV) Miguel de Cervantes 120 Complejo Ind. Chihuahua, Chihuahua, Chih. 31136 México.

ABSTRACT

CO_2 capture and photocatalytic reduction to hydrocarbons is an interesting yet challenging area that requires photocatalysts with the capability to capture and photoconvert CO_2 simultaneously. Furthermore, earth-abundant photocatalysts with high efficiency and product selectivity are essential for commercialization. Thus, two earth-abundant photocatalysts based on copper and nickel oxides were selected to produce solar fuels from CO_2 photoreduction. The photocatalysts were immobilized on commercial glass fibers substrates by a facile one-step microwave-hydrothermal method. Cu_xO (x=1, 2) and Ni_xO_y (x=1, 2 and y =1, 3) coatings on glass fiber were evaluated as photocatalysts in two different reactors to investigate the selectivity in a continuous reactor and a batch system. Two different light sources were employed: a heterochromatic lamp to simulate part of the solar light in the continuous reactor and a LED visible light in the batch reactor. CuO/Cu_2O photocatalysts exhibited a selective production of CH_4 (95 μmol g^{-1} h^{-1}) and CH_3OH (177 μmol g^{-1} h^{-1}) from CO_2 photoreduction in the continuous and batch continuous systems, respectively. The superior performance was attributed to the unique rod-shape morphology, the presence of oxygen vacancies and efficient charge transfer in the CuO/Cu_2O heterostructure with high affinity towards CO_2, resulting the formation of mono- and bidentate carbonate species during the CO_2 photoreduction reaction. Ni_xO_y coating with 2D cubic shape produced CO (103 μmol g^{-1} h^{-1}) and HCOOH (4245 μmol g^{-1} h^{-1}), associating with the low CO_2 affinity and less efficient charge separation compared to CuO/Cu_2O heterostructure.

Keywords: Photocatalysis; CO_2 reduction; Solar fuels; CO_2 adsorption; CuxO; NixOy.

1. Introduction

Carbon dioxide (CO_2) is considered the main greenhouse gas (GHG) responsible for climate change [1]. Fossil fuel utilization is the main contributor to anthropogenic CO_2 emissions [2,3]. One of the promising routes to address CO_2 emissions and provide an alternative energy source is implementing artificial photosynthesis. This process could be carried out through CO_2 photocatalytic conversion into light hydrocarbon molecules, such as CH_4, syngas (CO/H_2), alcohols, and aldehydes [4-6].

TiO_2 has been extensively used as a photocatalyst reduction of CO_2 process. However, TiO_2 is not an ideal photocatalyst to carry out the CO_2 photoreduction because it has a low affinity for CO_2 in the presence of H_2O [7]. The use of other oxides such as Cu_xO (x=1, 2), NiO, Fe_2O_3, ZnO, and MgO, represents an excellent option to be used in this process due to their ability to attract electrons and provide active sites for CO_2 fixation, such as oxygen vacancies (OVs) [8-13]. Copper and nickel oxides have resulted in good efficiencies for the CO_2 photoconversion process; however, their use has been limited as co-catalysts for photocatalytic CO_2 conversion [9, 12-14].

Cu_xO (x= 1, 2) materials have shown potential advantages for the CO_2 conversion because CuO favors CO_2 adsorption through the formation of monodentate and bidentate carbonate species [14]; whereas Cu_2O provides adequate reduction potential, visible-light absorption, and selective active-sites to capture electrons, and enhancing multi-electron reactions on its surface [15, 16]. These properties have favored the production of CH_4. On the other hand, NiO has been used as a co-catalyst for CO_2 photoreduction to CH_3OH, CH_4, and CO in some composite materials, such as $NiO/In_2O_3/TiO_2$ [17], $Ni/NiO/g\text{-}C_3N_4$ [18], $NiO/InTaO_4$ [8], and ZnO/Ni [19]. Previous works suggest that the coexistence of Ni^{2+}/Ni^0 pairs in core-shells

structures enhanced the electron transfer among the semiconductors and it promotes the formation of CO from the CO_2 photoreduction [17, 18]. From these works, it seems that the presence of NiO and Cu_xO favored the generation of CO and CH_4 in gas phase continuous reactors, respectively. However, the selectivity of these two photocatalytic materials has not been explored in detail under similar operation parameters since most of the works use different high-power lamps that emit in the UV range [12,13,20-28]. Therefore, studying of both oxides under similar reaction conditions is interesting and could help understand each oxide's selectivity in the continuous and batch systems since previous reports suggest different reaction mechanisms in the gas (continuous) and liquid (batch) phases [29, 30], as is shown in **Figure 1**.

Some of the challenges related to the photocatalytic materials, for the scaling-up of the CO_2 photoreduction, are the rapid recombination of the photogenerated charges, light absorption, low surface areas, lack of active sites adequate for the reaction (e.g., OVs), the deactivation or poisoning of the photocatalysts, the CO_2 adsorption or the desorption of by-products, the low selectivity, and the immobilization of the photocatalyst [4]. Considering these factors, this work proposes two complementary strategies for the design of efficient photocatalytic materials to provide insights to overcome some of these challenges. One of the strategies implemented was the design of heterostructured materials to reduce the recombination of the photogenerated charges in earth-abundant copper and nickel oxides [31, 32]. In this context, the use of heterostructured materials represents a good strategy to promote an improvement of the separation of photogenerated electron-hole pairs and enhance the selectivity of solar fuel production. For this purpose, the use of type-II heterostructured materials promotes the formation internal electric fields that can drive the electron and holes transfer in opposite directions, which decrease the recombination of the photogenerated charges, as is also shown

in **Figure 1**. In this scheme is also included the charge transfer in type-II heterostructured materials.

Secondly, the immobilization of photocatalysts on commercially available, low-cost, and flexible substrates, e.g., glass fibers, could favor the process of scaling-up as well as providing a higher exposed area for photocatalytic reaction, promoting efficient charge transport, and enhancing light absorption [33]. The use of immobilized photocatalyst has been successfully demonstrated in recent reports for CO_2 photoreduction, as is shown in **Table S1**.

In summary, this work focuses on increasing solar fuel production using visible-light active heterostructure photocatalysts immobilized on flexible and low-cost substrates in a continuous and batch systems. The heterostructures were evaluated in a continuous reactor under UV-Visible light from a solar simulator. At the same time, in the batch experiments, a LED visible lamp was used to activate the materials. In addition, a practical yet novel approach to fabricate nickel and copper oxides coatings, which possessed a high affinity towards CO_2 and enhanced visible-light absorption, is proposed herein.

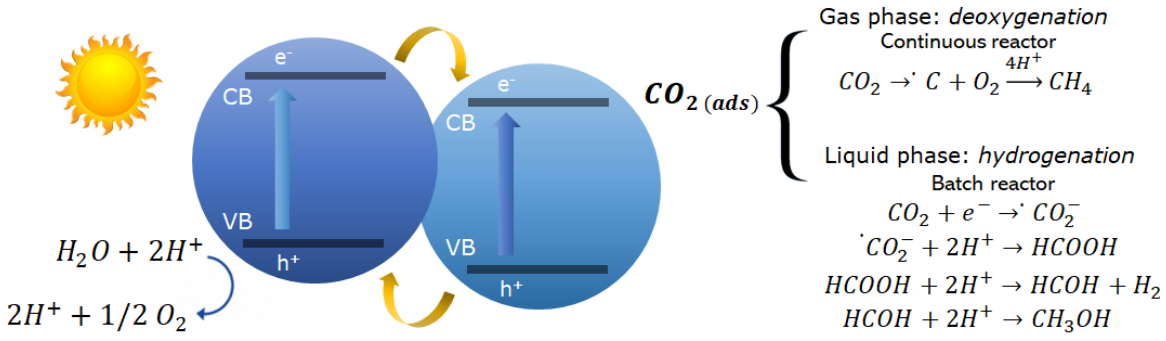

Figure 1. Photocatalytic mechanism of heterostructured materials in the gas and liquid phases.

2. Experimental Section

2.1. Fabrication of Cu_xO (x=1, 2) and Ni_xO_y (x=1, 2 and y =1, 3) coatings on glass fibers

The deposition of Cu_xO (x=1, 2) and Ni_xO_y (x=1, 2 and y =1, 3) on glass fiber (GF) were performed by an in-situ microwave-hydrothermal (MH) method. The oxides were deposited on GF substrates with the following composition: SiO_2, Na_2O, and CaO, with an open slit of 2.7 mm and an effective area of 2.73 cm^2 [33]. First, the substrate was cleaned under sonication for 25 minutes with pure acetone (Baker, 99.5%), methanol (DEQ, 99.9%), and distilled water. Then, the substrate was dried at 80 °C overnight before use.

The cleaned GF substrates were placed in an autoclave that contained an aqueous solution of $Cu(CH_3COO)_2 \cdot H_2O$ (Fermont, 99%) or $Ni(CH_3COO)_2 \cdot 4H_2O$ (Fermont, 99%), according to the experiment design, as shown in **Table 1**. Then, different quantities of glucose ($C_6H_{12}O_6$, Sigma, 99%) as reducing agent were added. Subsequently, NaOH (Fermont, 99%) was added slowly into the Cu and Ni solution. The autoclave was heated in a microwave reactor (Mars 6) at 300 W at 80 °C for 60 min. The coating on the GF was washed with distilled water and then dried at 100 °C overnight. The identification of the samples is shown in **Table 1**.

Table 1. Synthesis parameters used for the deposition of the films on the GF.

Sample ID	[NaOH] (M)	[$C_6H_{12}O_6$] (mol)
Cu-1	0.3	0.0
Cu-2	0.6	
Cu-3	0.3	0.015
Cu-4	0.6	
Ni-1	0.3	0.0
Ni-2	0.6	
Ni-3	0.3	0.015
Ni-4	0.6	

2.2. Material characterization

The crystalline phases of the coating were analyzed using X-ray diffraction (XRD, Bruker D8 Advance diffractometer). The measurements were performed in a 2θ interval from 10 to 70° with a step size of 0.02° for 0.3 s with Cu Kα radiation 1.5418 Å. The morphological characterization and elemental mapping were conducted with scanning electron microscopy (SEM) using a JEOL JSM-6490LV microscope with an acceleration voltage of 20 kV by placing the samples on carbon tape and covered with gold-palladium coating for the measurement. Furthermore, the surface of the samples was analyzed using a Luxo Microscope System model 273RB-RLI. Diffuse reflectance of the photocatalysts was determined using a Perkin Elmer Lambda 950 UV-Visible spectrophotometer equipped with a 150 mm integration sphere. The bandgap (Eg) was estimated using the Kubelka-Munk (K-M) function, considering a direct charge transfer on Cu and Ni transition oxides. With this data, the theoretical conduction and valence band potentials were calculated by equations 1 and 2.

$$E_{VB} = X - E^e + 0.5E_g \quad (1)$$

$$E_{CB} = X - E^e - 0.5E_g \quad (2)$$

where X is the absolute electronegativity, E^e is the energy of free electrons on a hydrogen scale (4.5 eV), and Eg is the energy band gap. Fourier transform infrared spectroscopy (FTIR) was used to study the surface properties of the fabricated samples before and after the CO_2 capture and photoreduction processes. The characteristic spectra of the samples were identified using the Thermo FTIR Nicolet iS50 kit in a range of 600-4000 cm^{-1}. Photoluminescence (PL) analysis was performed at room temperature in a fluorescence spectrophotometer (Cary Eclipse) integrated with a Xenon flash lamp. The samples were excited at 300 nm and an emission slit of 5 at room temperature. The crystal structure and shape of heterostructures were analyzed by transmission electron microscopy (TEM) using a JEOL JEM–2200FS. For

TEM characterization, the powders were suspended in isopropanol. The solution was dropped onto the Lacey carbon grids (300 mesh) and dried at room temperature. The surface composition of the coating was analyzed by X-ray photoelectron spectroscopy (XPS) using a Thermo Scientific Escalab 250 Xi with step energy of 200 eV for survey scans and 50 eV for high resolution scans with step sizes of 1.0 and 0.1 eV, respectively. Batch neutralization of the sample was accomplished using a combination of Ar low-energy ions and electrons. Photocurrent measurements were performed on FTO glass. For this purpose, the working electrode was prepared with each sample by the spin coating method; this method consists in preparing 5 mg of the sample in 10 mL of isopropanol and sonicated for 25 min. Then, the homogeneous solution was coated dropwise over an FTO glass with an active area of 1.0 x 1.0 cm^2 and dispersed by spinning at 2800 rpm for 20 s. The coated FTO glasses were then dried at 80 °C, and a similar step is repeated for consecutive layers (25 times). The prepared film was annealed at 200 ºC for 1 h, at 10 °C min^{-1}. Chronoamperometry was conducted using an Autolab with 0.1 M NaOH as an electrolyte. The irradiation source was turned on for 60 s and then off for another 60 s. These on-off cycles were repeated for 6 min.

2.3. CO_2 adsorption analysis

Temperature programmed desorption (TPD) was performed using a ChemBET Pulsar TPD from Quantachrome Instruments to evaluate the CO_2 adsorption affinity of the materials synthesized. 100 mg of the sample was placed in a U-shaped reactor between two pieces of quartz wool. The sample was heated in an inert atmosphere (N_2, 99.9995%) to 150 °C to eliminate adsorbed compounds for 3 h. Then, the sample was cooled down to 50 °C. Next, a flow of CO_2 (0.35 mL min^{-1}) was passed for 60 min and then replaced by He (99.9995%). The measurement started when a stable baseline was achieved. After that, the sample was

heated at 350°C at a constant rate of 10°C min^{-1}. The CO_2 desorption signal were recorded by Thermal Conductivity Detector (TCD).

Operando Diffuse Reflectance Infrared Fourier Transform Spectroscopy (DRIFTS) experiments were conducted on Agilent Cary 600 series spectrometer equipped with Harrick Praying Mantis reaction cell. The gas inlet of the cell was directly connected to a flow system equipped with mass flow controllers and a temperature controller. The cell outlet was connected to the mass spectrometer Hiden QGA MS. In each experiment, 20 mg of catalyst powder was placed in the cell. Before reaction, the KBr background was collected in presence of CO_2, which was flowing through the bubbler. 64 scans were collected per spectrum with a spectral resolution of 4 cm^{-1} and in the spectral range of 4000-400 cm^{-1}. The experiment was performed under UV-Vis irradiation at 24 and 40 °C and dark (24 °C) conditions to simulate the experimental conditions within the photocatalytic reactor.

2.4. Photocatalytic CO_2 reduction

a) Continuous reactor

Continuous gas-phase CO_2 photoreduction experiments were performed in a stainless-steel ring-type reactor, previously described in [34]. The coatings (2.5 x 4 cm^2) were placed in the photoreactor, with a volume of 1.96 mL, before it was sealed. The system was purged with pure CO_2 to remove residual air overnight. A constant flowrate of CO_2 was set to 0.35 mL min^{-1}, with a relative humidity of 1.8% measured by an Arduino sensor. In this case, H_2O was used as precursor of H^+ ions for the CO_2 photocatalytic reduction. The temperature of the reaction (40 °C) was maintained using a hot plate. The light source was a heterochromatic lamp model OmniCure S2000 that emits in 300-600 nm wavelength to simulate the solar light irradiation. The lamp was placed 30 mm above the surface of the sample. The irradiance

(150 mW cm^{-2}) was measured using an OmniCure R2000 radiometer (±5%). An inline GC/TCD/FID (Agilent, Model 7890B series), a Hayesep Q column (1.5 m), 1/16-inch OD, 1 mm OD), Molecular Sieve 13X (1.2 m), 1/16-inch OD, 1 mm ID) was used to quantify the photoreaction products. The system also has a nickel catalyzed methanizer and a flame ionization detector (FID) to analyze the products every 4 min. The products CH_4 and CO were measured by FID, while TCD identified H_2 and O_2.

To evaluate the recyclability of each set of coatings, third cycling tests was conducted under identical conditions. After each test, the sample was heated at 200 °C for 2 h before employing in the next cycle.

b) Batch reactor

The samples with the highest performance for CO_2 photoreduction were evaluated in a batch quartz reactor in liquid phase at room temperature. For these experiments, the coatings (2.73 cm^2) were placed inside the batch reactor with 150 mL of distilled water under magnetic stirring. The reactor was bubbled with CO_2 for 30 minutes to replace the solution's dissolved oxygen. In this reactor, a different light source was used to emulate the visible light from the solar light. The reactor was irradiated with 2 LED lamps of 20 W each, which exhibit two emissions at 443 and 535 nm, from the sides. The reaction products in the liquid phase were monitored by different techniques, as described here. Formic acid (HCOOH) and formaldehyde (CH_2O) were measured with high-performance liquid chromatography (HPLC) after 1 h of reaction. The CH_2O quantification was carried out by injecting 25 µL of the liquid sample into the system, with a Fenomenex C-18 column, using a 50:50 v/v acetonitrile-water (HPLC grade Baker) mixture as a carrier. Before the sample was injected, the liquid sample was derivatized, forming a complex product of the reaction with 2-4, dinitrophenyl hydrazine (Aldrich, 98%) and phosphoric acid (Baker, 98%) [35]. On the other hand, the HCOOH

measurement was carried out by injecting 15 μL of previously sample filtered reaction liquid sample [36]. Additionally, CH_3OH was determined by gas chromatography. To corroborate the reaction products, the liquid sample was analyzed by nuclear magnetic resonance (^1H NMR) analysis on a Bruker 400 MHz Avance III HD spectrometer (Bruker, BioSpin, USA) equipped with a 5 mm BBO SP probe with Z-field gradient. TopSpin 3.6.1 software (Bruker Biospin) was used for FID processing. CHENOMX NMR Suite 8.5 software was used for signal identification.

3. Results and discussion

3.1. Material properties

Homogeneous Cu_xO and Ni_xO_y coatings on GF were fabricated with a simultaneous microwave-hydrothermal method in the presence of glucose, as a reducing agent, in a basic medium. X-ray diffraction (XRD) was used to investigate the crystalline phases of the coatings (**Figure 2**). Cu_xO (x=1, 2) coatings exhibited a wide range of crystal compositions. The coatings obtained in the absence of the reducing agent (Cu-1 and Cu-2) exhibited the monoclinic phase of CuO (JCPDS:45-0937). The reflections of CuO were observed at 32.5, 35.8, and 38.6°, which correspond to the crystal planes (110), (-111), and (111), respectively (**Figure 2a**). Traces of the Cu_2O phase were also identified in these samples (**Table 2**). The rest of the samples (i.e., Cu-3 and Cu-4) synthesized in the presence of a reducing agent exhibited a mixture of Cu_2O and Cu phases in different proportions (**Table 2**). Specifically, Cu-3 presented a mixture of Cu_2O/Cu (i.e, Cu_2O as majority phase), whereas Cu-4 sample showed mainly elemental copper (Cu^0) with trace amount of Cu_2O (JCPDS: 01-71-4609 and 01-71-3645, respectively). The addition of NaOH also significantly influenced the crystal phase

mixtures in the samples. Notably, the increase of NaOH concentration promoted the reduction of Cu^{2+} to Cu in samples Cu-3 and Cu-4.

The nickel oxide coatings exhibited only the cubic structure of NiO (JCPDS:01-089-7131, **Table 2**). These samples presented intense reflections at 2θ = 37.4°, 43.4°, and 62.9°, corresponding to (110), (200) and (111) planes, respectively **(Figure 2b)**.

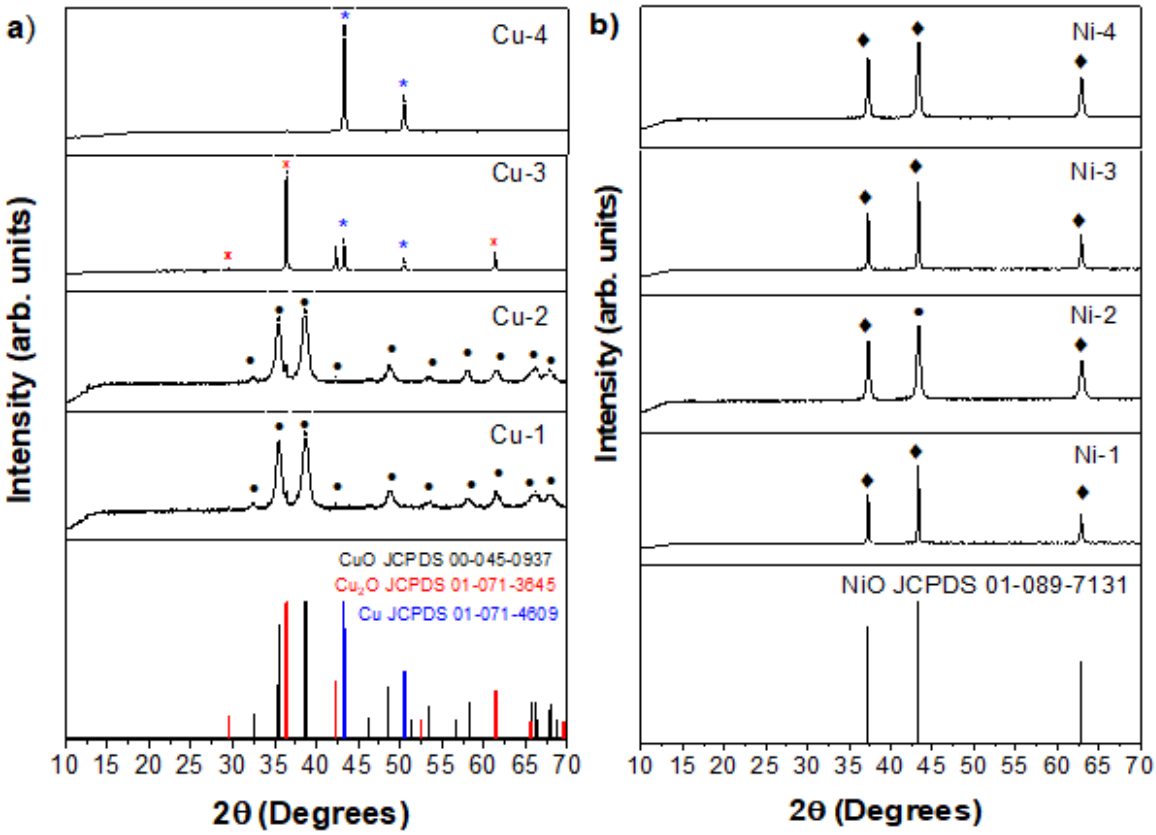

Figure 2. XRD patterns of a) Cu_xO (x=1, 2) and b) NiO coatings.

The morphology of the fabricated coatings was analyzed by SEM. All the Cu_xO coatings showed a variety of morphologies in the presence of glucose and different concentration of NaOH (**Figure 3**). Sample Cu-1 showed agglomeration with elongated bars (**Figure 3a**), whereas sample Cu-2 exhibited a more defined morphology of bars with an average width

and length of 1.3 and 5.2 µm, respectively (**Figure 3b**). Cu-3 and Cu-4 coatings, which possessed a mixture of Cu_2O/Cu phases, exhibited different octahedral particles with an agglomeration (**Figure 3c and d**) due to glucose addition.

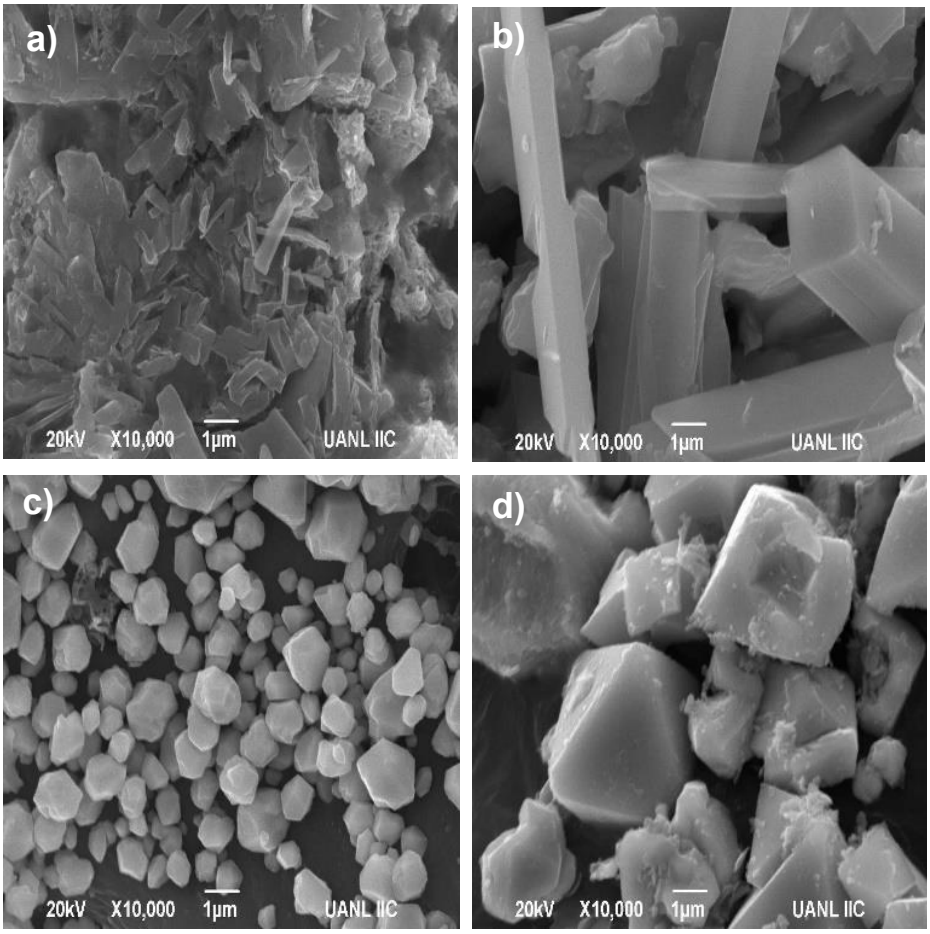

Figure 3. SEM images of a) Cu-1, b) Cu-2, c) Cu-3 and d) Cu-4 samples.

Different amounts of NaOH and glucose were also employed to synthesize nickel oxides. Sample Ni-1 exhibited a notable agglomeration and undefined morphology (**Figure 4a**). When the dosage of NaOH was increased to 0.6 M, the morphology of Ni-2 revealed irregular flakes with a thickness of ~275 nm and agglomerated cubes (~620 nm) (**Figure 4b)**. The addition of glucose promoted the formation of nanoflakes (~400 nm), as shown in samples Ni-3 (**Figure 4c**). When the highest dosage of NaOH (0.6 M) and glucose was added, a well-

defined cubic microstructure (~540 nm) was observed in the sample Ni-4 (**Figures 4d**). The average particle size is summarized in **Table 2**. EDS mapping obtained under SEM evidenced the homogeneity of the copper and nickel of the fabricated samples on GFs (**Figure S1**).

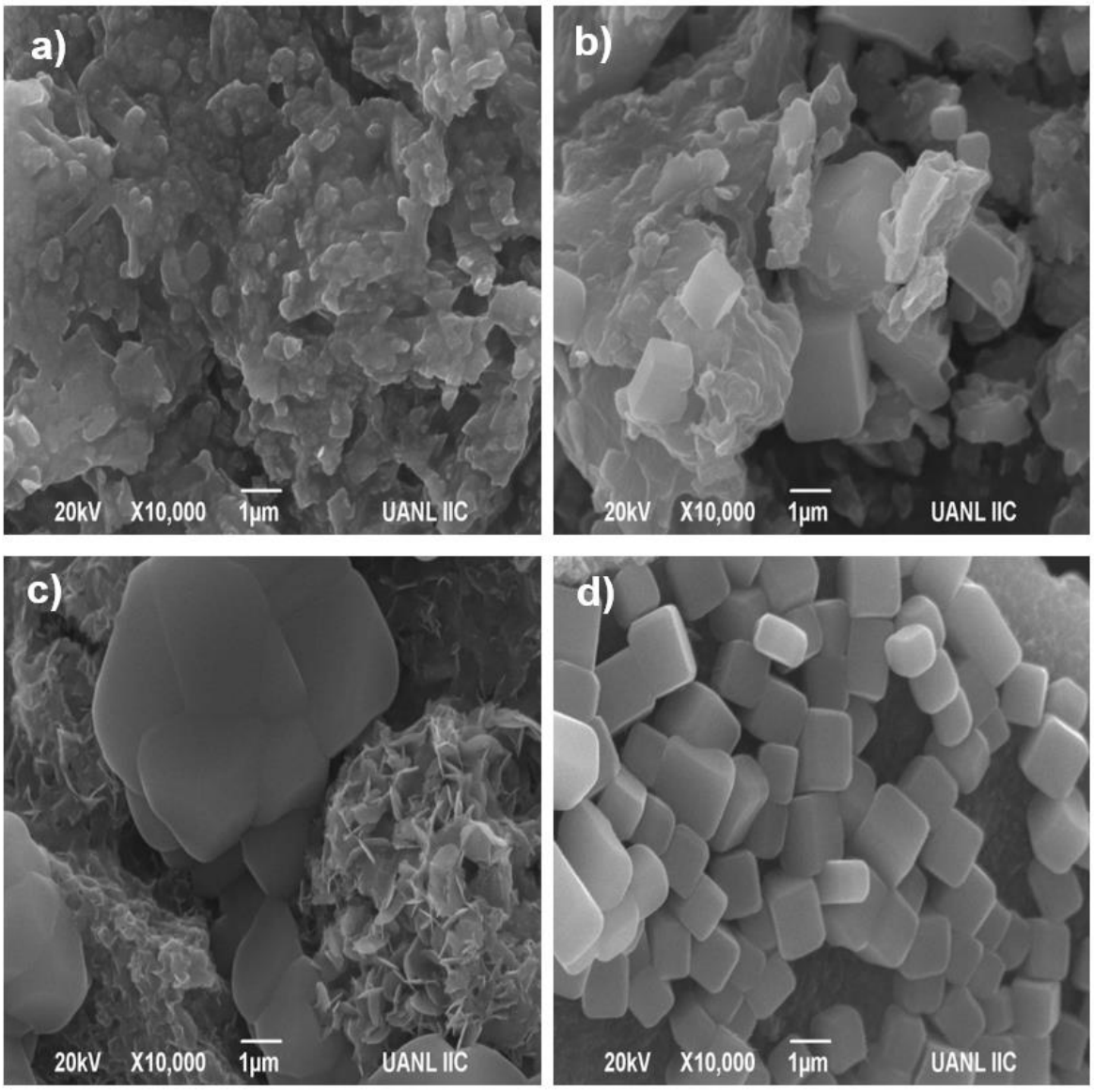

Figure 4. SEM images of a) Ni-1, b) Ni-2, c) Ni-3 and d) Ni-4 samples.

The bandgap energy of the fabricated samples was estimated from the graph of $[F(R\infty)h\nu]^{1/2}$ *vs* photon energy (**Figure 5**). The bandgap energies of the synthesized samples are summarized in **Table 2**. The Cu-1 and Cu-2 coatings, dominated by CuO particles, presented similar bandgap energies, as reported previously (1.5-1.6 eV, **Figure 5a**) [14]. The rest of the samples (Cu-3 and Cu-4) exhibited an additional adsorption band at 2.1-2.3 eV was probably due to the presence of Cu_2O (**Figure 2a**) [37].

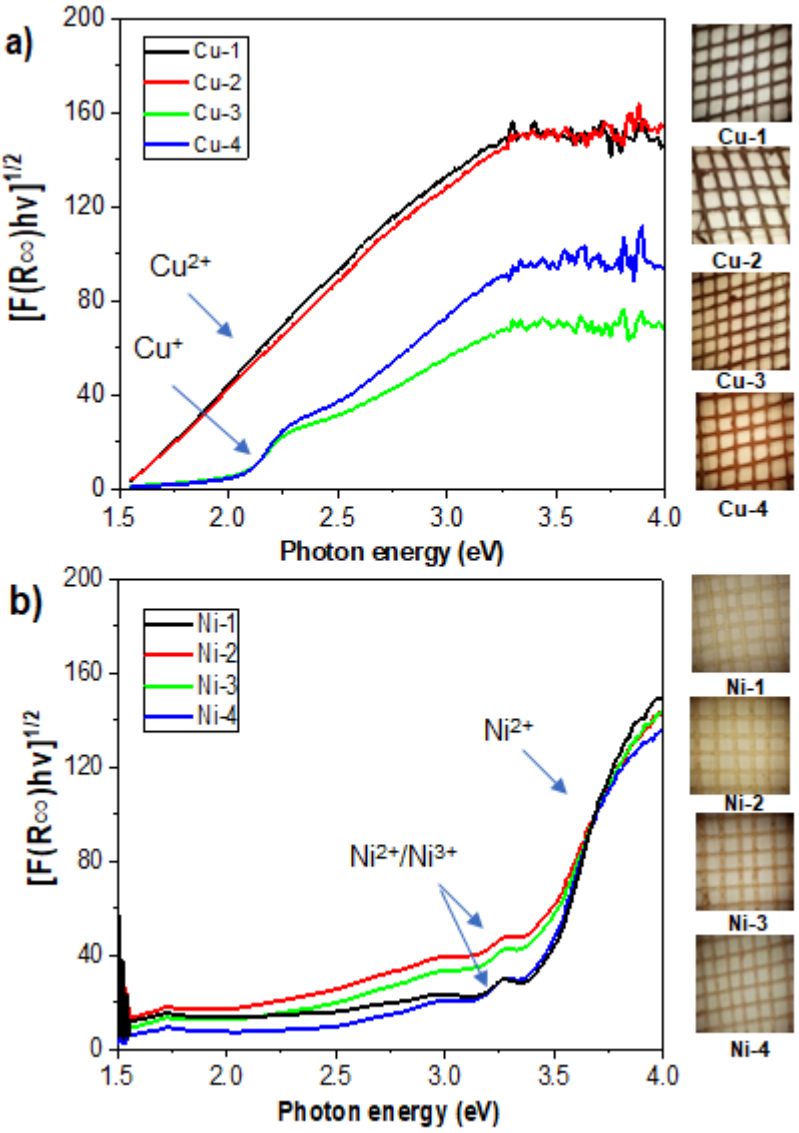

Figure 5. K-M spectra (left) and optical images (right) of the coatings: a) Copper oxides and b) Nickel oxides.

The K-M spectra of nickel oxides coatings are shown in **Figure 5b**. These samples exhibited bandgap energies between 3.3-3.5 eV, which are close to the values reported in the literature (i.e., 3.1- 3.6 eV) [38]. These values are characteristic of the green NiO (Ni-1 and Ni-3). In addition, a much weaker absorption band at 3.2-3.3 eV could be attributed to the Ni^{2+}/Ni^{3+} moiety [39, 40]. The presence of Ni^{2+}/Ni^{3+} is further discussed below using XPS.

Table 2. Physicochemical properties of the coatings.

Sample ID	Crystal phases identified	Particle size (nm)	Bandgap (eV)
Cu-1	CuO Cu_2O	300	1.5
Cu-2	CuO Cu_2O	1330	1.6
Cu-3	Cu_2O Cu	500	1.5
Cu-4	Cu Cu_2O	3300	2.3
Ni-1	NiO	275	3.2
Ni-2	NiO	620	3.3
Ni-3	NiO	400	3.2
Ni-4	NiO	540	3.3

PL spectra were used to study the recombination of charge carriers. The PL emission spectra of Cu_xO coatings exhibited two distinct peaks in the wavelength range of 600-900 nm (**Fig-**

ure 6a). Both peaks were assigned to the radiative emissions of the recombination of electrons and holes on CuO [41]. Cu-1 and Cu-2 samples showed a lower PL intensity, indicating a lower recombination rate as compared to Cu-3 and Cu-4 samples. This observation evidenced the efficient isolation of e^{-}-h^{+} pairs in the CuO/Cu_2O heterostructures [42].

The nickel oxides coatings showed a broad UV emission band peak at 378-380 nm corresponding to the radiative emission of the recombination of photogenerated charges in NiO (**Figure 6b**) [43]. Sample Ni-3 exhibited the lowest PL intensity, indicating a more efficient charge transfer with the flake structured sample.

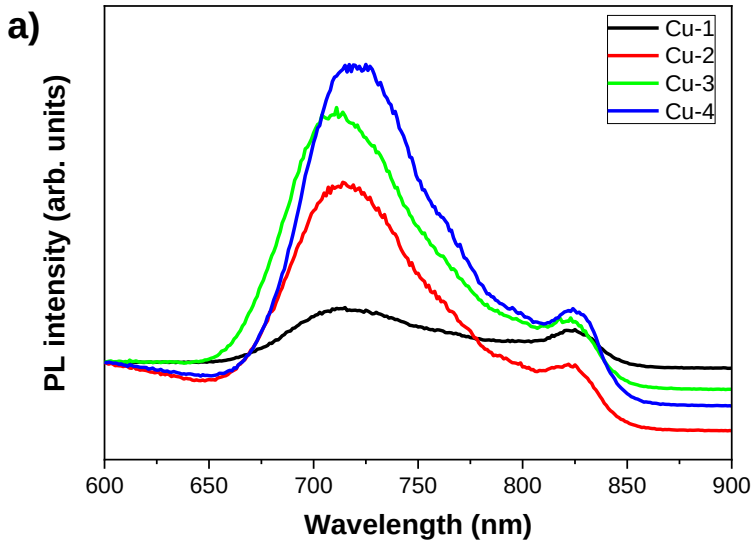

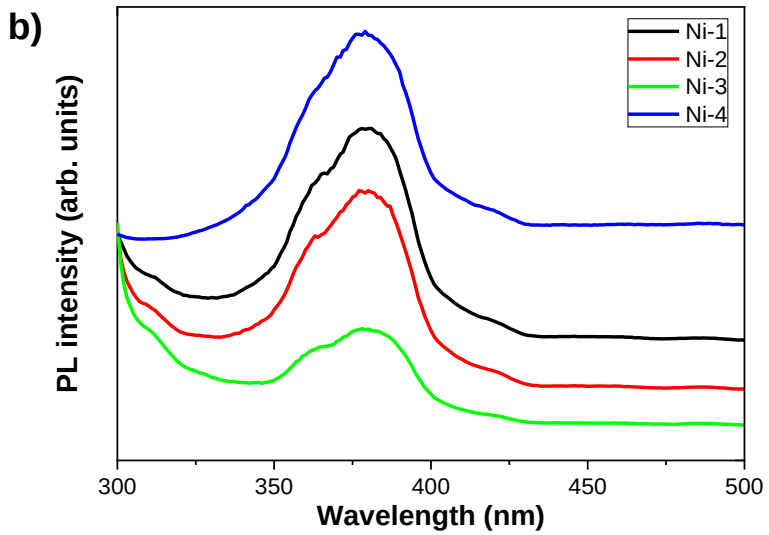

Figure 6. Photoluminescence (PL) emission spectra of the coatings (λ_{exc}= 300 nm).

3.2. Evaluation of CO_2 adsorption

FTIR spectroscopy was used to identify the CO_2 molecule fingerprint on the coatings (**Figure 7**). In general, copper oxides exhibited much more intense troughs than the coatings of nickel oxides, indicating that CuO samples possessed a higher affinity towards CO_2 molecules than nickel oxides. Specifically, Cu-1 and Cu-2 revealed two types of absorption bands at 1560 and 1410 cm^{-1} and 1340 and 1020 cm^{-1}, which were assigned to the monodentate and bidentate carbonate species, respectively [44-46]. However, these bands were absent in Cu-3 and Cu-4, probably attributed to the low basicity of Cu_2O and Cu that had a low affinity towards CO_2. On the other hand, the weak trough (1410 cm^{-1}) shown in the nickel oxides suggested only the monodentate bond presented on the surface of these samples.

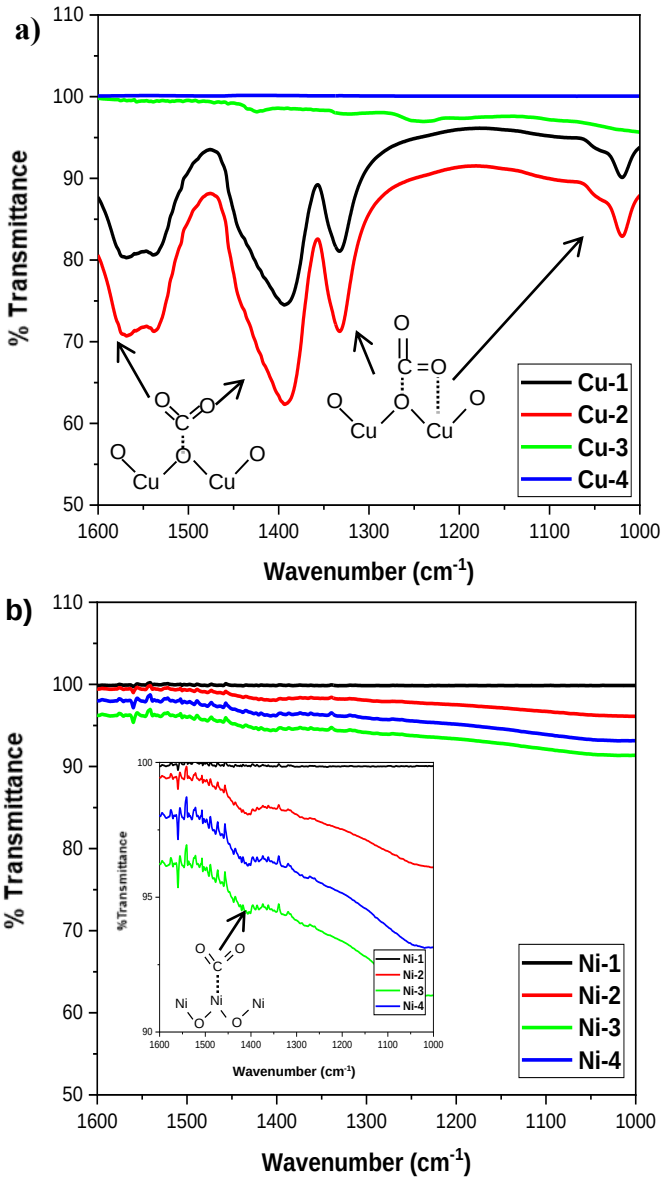

Figure 7. FTIR spectra of a) Copper oxides and b) Nickel oxide coatings.

Cu-1 and Cu-2 coatings, which exhibited a higher affinity towards CO_2 compared to the other fabricated samples, were further evaluated using TPD **(Figure 8)**. Cu-1 with higher CuO content compared to Cu-2 showed a higher CO_2 adsorption capacity. This observation agreed with the FTIR analysis, as shown in **Figure 7a**. The physical-desorption temperature of the samples was close to 280 °C for Cu-1 and Cu-2, respectively. This could be associated with

the exothermic enthalpy of CuO for CO_2 adsorption (ΔH_{ads}= -45.5 kJ mol^{-1}) [47]. The CO_2 chemical-desorption in the Cu-1 and Cu-2 samples was observed at ~320 °C, which may be related to the decomposition temperature of $CuCO_3$ around 300°C. It is worth mentioning that the rest of the samples did not show any response to the adsorbed CO_2 under the same conditions. This could be attributed to the presence of Cu and Cu_2O in the samples that hindered CO_2 adsorption since these phases exhibited endothermic enthalpies in this process ($\Delta H_{ads}Cu_2O$ = +142 kJ mol^{-1}) [47]. From the results reported above, samples Cu-1 and Cu-2 seems to be a potentially good candidate for the CO_2 adsorption and subsequent photocatalytic reduction of CO_2, since they have a low CO_2 desorption temperature that favored the subsequent conversion of CO_2. On the other hand, the adsorption over the nickel oxides samples was under limit detection, and the TPD patterns are in the supplementary section (**Figure S2**).

The FTIR spectra show the moieties adsorb on the surface of the photocatalyst during the reaction. In contrast, the TPD pattern shows the amount of CO_2 desorb. When the TPD peak is high, it indicates more negligible adsorption. This process also describes the physical- and chemical adsorption on the photocatalyst surface. Hence, the FTIR and TPD results show the correct relationship, in which high adsorption of CO_2 (FTIR) and low desorption (TPD), as shown in sample Cu-2, which eventually favor the CO_2 photoconversion. On the other hand, Ni-3 does not show CO_2 adsorption, which could modify its selectivity of the CO_2 reduction, as will be further discussed.

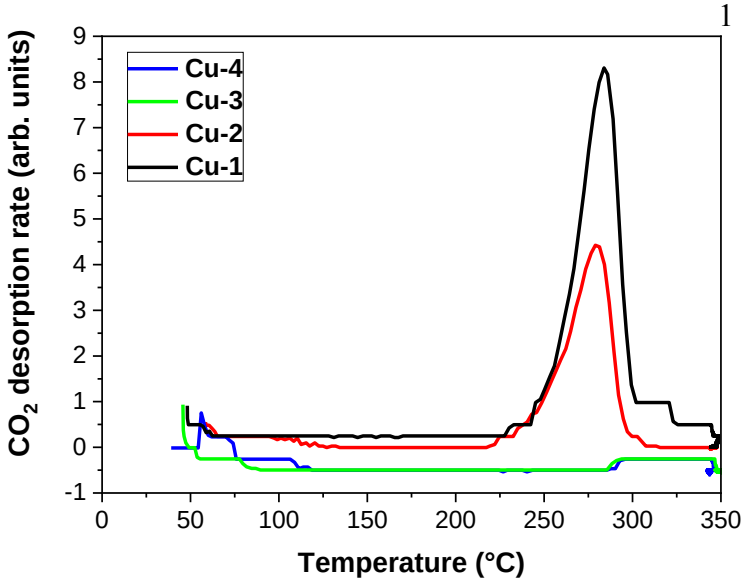

Figure 8. TPD profiles of the fabricated Copper oxides samples.

The sample with the highest affinity to CO_2 (i.e., Cu-2) was further studied with *operando* DRIFTS (**Figure S3**). The Cu-2 sample showed a strong absorption band at 2348 cm^{-1}, associated with the adsorbed CO_2, when CO_2 was fed into the reactor at 24 °C in the dark. In addition, bands at around 1620, 1420, and 1296 cm^{-1}, which were assigned to the asymmetric CO_3 stretching vibration [$\nu_{as}(CO_3)$], symmetric CO_3 stretching vibration [$\nu_s(CO_3)$] and O−H deformation vibration [δ (O−H)] of monodentate bicarbonate species (*m*-HCO_3^{2-}), respectively, were observed upon CO_2 feeding in the dark [48, 49]. When the UV-vis light irradiated onto the sample, the intensity of these bands decreased immediately. The bands at around 1540 and 1384 cm^{-1} correspond to the [$\nu_{as}(CO_2)$] and [$\nu_s(CO_2)$] of the bidentate formate species (*b*-HCO_2^{2-}) [50]. This observation suggested that the CO_2 molecules adsorbed on the surface of Cu-2 were mainly *m*-HCO_3^{2-} and converted to *b*-HCO_2^{2-} through the reaction with OH^- on the surface or oxygen vacancies (OVs) of Cu-2. When the reaction temperature increased to 40 °C, the bands of *m*-HCO_3^{2-} continued to decrease, whereas *b*-HCO_2^{2-} increased steadily. In other words, the adsorption of CO_2 and conversion of *m*-HCO_3^{2-} to *b*-HCO_2^{2-}

were enhanced at elevated temperatures. The *operando* DRIFT results suggested that the mechanism for the photocatalytic CO_2 reduction route of Cu-2 was through the carbene pathway.

According to the FTIR and *operando* DRIFTS results, the fabricated Copper oxides and Nickel oxides coatings were proposed to be partially carbonated during CO_2 adsorption. The proposed mechanism was illustrated in **Figure S4**. In the case of the CuO/Cu_2O, the surface oxygen present on the CuO could act as a Lewis base site that could donate an electron to the C=O bond of CO_2. This phenomenon promoted the formation of monodentate bonds (carbon coordination bonds) and bidentate at the CuO surface, as shown in **Figure S4a**. The Cu, close to OVs, acts as a Lewis acid site by accepting electrons, interacting with oxygen from CO_2 producing $Cu \cdots O - C = O$ species. On the other hand, the bidentate coordination bond occurred by interacting the Cu and O in the CuO with CO_2 molecules [9, 14].

The FTIR spectra of the nickel oxides samples did not show significant changes before and after the CO_2 purge (**Figure 7b**). Only an appreciated amount of the monodentate species was formed on the NiO surface (**Figure S4b**).

3.3. Photocatalytic CO_2 reduction in a continuous system

The Copper oxide and Nickel oxide coatings were evaluated for the photocatalytic reduction of CO_2 in the gas phase in a continuous reactor under UV-Visible light. The amounts of different gaseous products (H_2, CO, and CH_4) was monitored with GC. CH_4 was the main product of the photocatalytic reduction of CO_2 when copper oxides were used as the photocatalyst, while H_2 and CO were generated in low amounts (<10 ppm), as shown in **Figure S5**.

The Cu-1 film showed the highest production rate of CH_4 (94.7 μmol g^{-1} h^{-1}) followed by the Cu-2 sample (67.1 μmol g^{-1} h^{-1}), which showed up to 32 times higher production than other reports (**Table S1**) [7, 12, 13, 20, 21, 24-28]. However, Cu-2 revealed a more consistent production of CH_4 than Cu-1 throughout the 4 h reaction, which could be attributed to several factors:

- A higher affinity for CO_2 resulted in the formation of monodentate and subsequent bidentate species, as is observed in the FTIR spectra.
- Rod morphology that provided active sites for effective CO_2 adsorption.
- The coexistence of CuO/Cu_2O in this sample resulted in the type-II heterostructure formation that promoted efficient charge transfer, supplying sufficient protons (8 H^+) and electrons (8 e^-) for the conversion into CH_4.

Cu-3 and Cu-4 with a mixture of Cu/Cu_2O showed a lower production of CH_4 than those samples with a higher content of CuO (i.e., Cu-1 and Cu-2), as seen in **Figure 9**. This could be associated with a rapid photo-oxidation of Cu/Cu_2O and low adsorption of CO_2 on these samples. It should be noted that the substrates, which consisted of CaO and Na_2O, exhibited some activity for solar fuels generation due to their intrinsic properties on CO_2 adsorption [33].

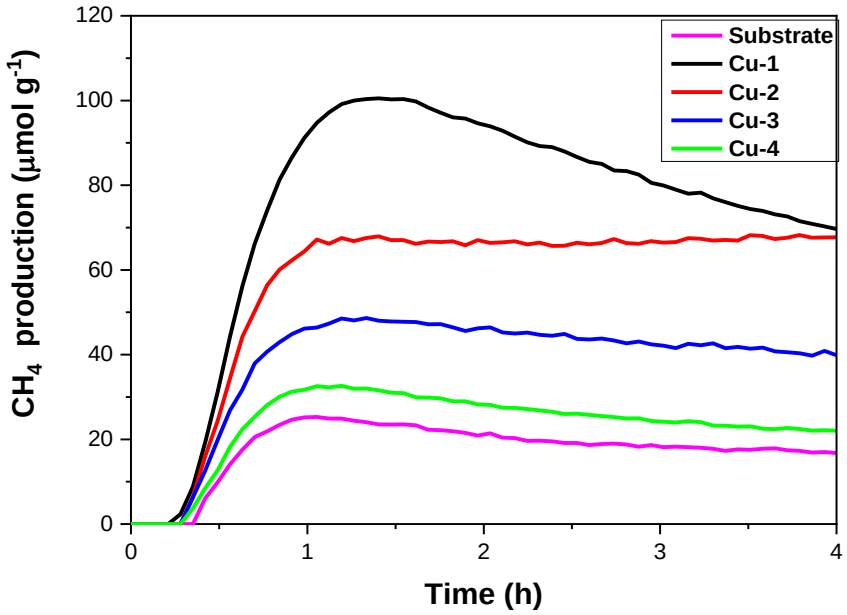

Figure 9. CH_4 evolution using the Copper oxide coatings under 300-600 nm irradiation.

The synthesized nickel oxides samples showed only CO production under the same experimental conditions (**Figure 10**). Ni-3 sample generated the highest amount of CO (103 µmol g^{-1} h^{-1}), which was around 3 times higher than the previous reports in the literature [20-23, 26-28]. Other carbonaceous by-products (CH_4) were obtained only in trace amounts (**Figure S6**). The superior results were attributed to the unique 2D morphology of flaky agglomeration and the coexistence of NiO and Ni_2O_3 moieties in Ni-3.

Also, it is important to note that the amount generated by the samples was distinguished than we observed having blank substrates, as shown in **Figures 9** and **10**.

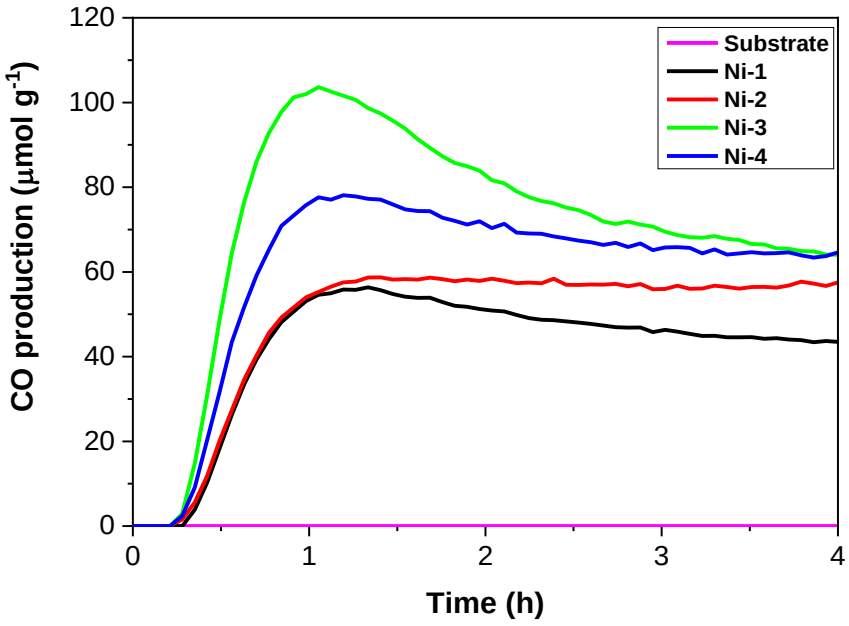

Figure 10. CO evolution using the nickel oxides coatings as photocatalyst under 300-600 nm irradiation.

Also, each system's best heterostructure activity was compared to single metal oxides to highlight the importance of the coexistence of CuO/Cu_2O and NiO/Ni_2O_3 phases on the coatings. A previous report of CuO coatings grown on glass fibers suggested that it exhibits selectivity for CH_4 production [51]; however, the stability and the efficiency for CH_4 generation with the CuO/Cu_2O heterostructure obtained here is higher. Regarding to the nickel-based samples, an additional sample was synthesized without the addition of NaOH or reducing agent, which was identified as Ni-0. This sample exhibited only the monoclinic NiO phase, and it did not exhibit the characteristic band of the coexistence of Ni^{2+}/Ni^{3+} sample, which confirms the presence of only NiO in this sample (Ni-0), as is shown in **Figure S7a,b**. The photocatalytic results show that pure NiO only produce half the yield as of sample with NiO and Ni_2O_3

heterostructure (**Figure S7c**). On the other hand, a coating of a commercial TiO_2 P-25 photocatalyst was prepared for comparative purposes. As shown in **Figure S8**, TiO_2 P-25 presented an apparent deactivation (55%) during the photocatalytic evaluation. This result could be explained by means of blocking the active sites through the deposition of carbon-containing products [52]. TiO_2 P-25 did not exhibit selectivity towards CH_4 or CO production since both products were obtained with 50 and 7 μmol g^{-1} h^{-1} production, respectively, after 4 h of reaction.

A general comparison of the CH_4 and CO production with the copper and nickel-based heterostructures and the traditional TiO_2 photocatalyst was included in **Figure S9**. As it can be seen, the CuO/Cu_2O and NiO/Ni_2O_3 heterostructures exhibited higher activity than the individual oxides: CuO, Cu_2O/Cu (Cu-3 sample), NiO and the traditional TiO_2 photocatalyst, which evidences its effectiveness for the selective generation of CH_4 and CO, respectively. Therefore, both compounds are good candidates to be used as alternative green fuels for energy process generation and other applications.

To provide further insights with Cu-2 and Ni-3, which showed the best performance in CO_2 photoreduction amongst the fabricated samples, these samples were further characterized using transient chronoamperometry (**Figure 11**) and HRTEM techniques (**Figure S10**) to elucidate the differences on their photocatalytic activity. Sample Cu-2 showed a *p*-type behavior with a negative photocurrent response, and the photocurrent density 2 was stable throughout the chronoamperometry measurements. However, the Ni-3 film, which was expected to be a *p*-type semiconductor, showed an *n*-type characteristic with a positive photocurrent response [53]. This observation could be attributed to defects within the crystalline structure, such as OVs, leading to the formation of Ni_2O_3 [54].

Specifically, Cu-2 showed a higher photocurrent (-27.3 μA cm^{-2}) than Ni-3 (0.41 μA cm^{-2}). The delta observed in the charge density in the coatings indicated a surplus of holes available in the photocatalyst valence band that could interact with the water molecule to generate hydroxyl radicals (·OH) and release protons (H^+). Hence, the result suggested that Cu-2 managed to photogenerated more electron-hole pairs for the photo-redox reaction, thus leading to a higher conversion efficiency than Ni-3.

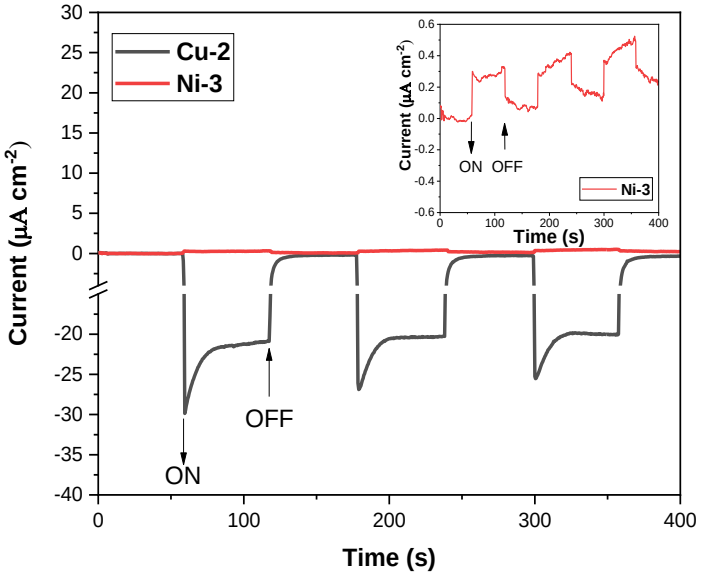

Figure 11. Chronoamperometric pattern of the Cu-2 and Ni-3 samples.

The morphology of Cu-2 and Ni-3 observed under TEM (**Figure S10a and b, respectively**) presented similar structures are those observed under SEM (**Figure 3**). HRTEM images evidenced the presence of the heterostructures in Cu-2 and Ni-3 (**Figure S10c and d)**. The CuO (111), and Cu_2O (211) and (200) crystal planes were identified with *d*-spacings ~0.23, ~0.17, and ~0.21 nm, respectively (**Figure S10c**); whereas the lattice fringes of NiO (200) and Ni_2O_3 (112) revealed an interplanar spacing of ~0.20 and 0.17 nm, respectively.

3.4. Characterization of the coatings after photocatalytic testing

The surface compositions and elemental valence states of the best performance coatings (i.e., Cu-2 and Ni-3) were investigated by XPS before and after the photocatalytic experiments. The analysis of the Cu-2 film surface before and after the photocatalytic reaction is shown in **Figure 12**. Three peaks at 284.4, 285.2, and 288.5 eV are associated with the C-C, C-O, and O-C=O bonds, respectively, of the adsorbed CO_2 (**Figure 12a**) [14, 55, 56]. The O 1s spectrum was fitted with four peaks centered at 529.6, 531.0, 531.9, and 533.3 eV (**Figure 12b**), corresponding to the oxygen in the lattice structure (O_L) of the O_L-CuO and O_L-Cu_2O [57, 58], OVs [59, 60], and oxygen adsorbed on the surface with low coordination related with C-O (O_a) [61, 62], respectively. Meanwhile, the Cu 2p spectrum was deconvoluted in two peaks attributed to Cu^+ and Cu^{2+} at 933.1 and 953.1 eV, respectively (**Figure 12c**) [63-65]. The Cu^{2+} peaks and their respective satellites (Cu $2p_{3/2}$ and Cu $2p_{1/2}$) appeared at 934.3, 954.3, 961.4, and 962.5 eV for Cu-2.

After the photocatalytic reaction, the Cu-2 sample showed an additional band in its C 1s spectrum related to C-H bond at 286.1 eV (**Figure 12d**). This band could be ascribed to the residual methoxide, which is an intermediate of the photocatalytic reaction [66]. This species could be adsorbed on the edge sites of the film forming CH_3O-Cu^{2+} [67]. Moreover, the intensity of the signal at 532.1 eV grew after the reaction due to the presence of hydroxides (O-H), carbonates (CO_3^{2-}) [68], or oxygen-containing hydrocarbons (CH_3O-Cu^{2+}) [69], while the signal related to OVs at 531.0 eV disappeared after photocatalytic CO_2 reduction, probably because to the partial carbonation of the photocatalyst after the test (**Figure 12e**). The results indicated that OVs acted as an active site for CO_2 adsorption. It is also possible to observe an additional band around 934.8 eV related to the partial carbonation of the CuO [46, 70], which suggested the formation of intermediates monodentate and bidentate carbonate species. The Na 1s signal, which was originated from the substrates, was studied thoroughly.

The reference spectra showed a central peak at 1071.2 eV corresponding to Na-O bond present in Na_2O (**Figure S11a, b)** [71, 72]. A new band around 1071.6 eV appeared in the Na 1s spectrum after the reaction, which was associated with the partial carbonation of Na_2O (**Figure S11c, d)** [72, 73]. The carbonation of Na-O suggested that this oxide acted as an additional active site for CO_2 adsorption, enhancing the global efficiency.

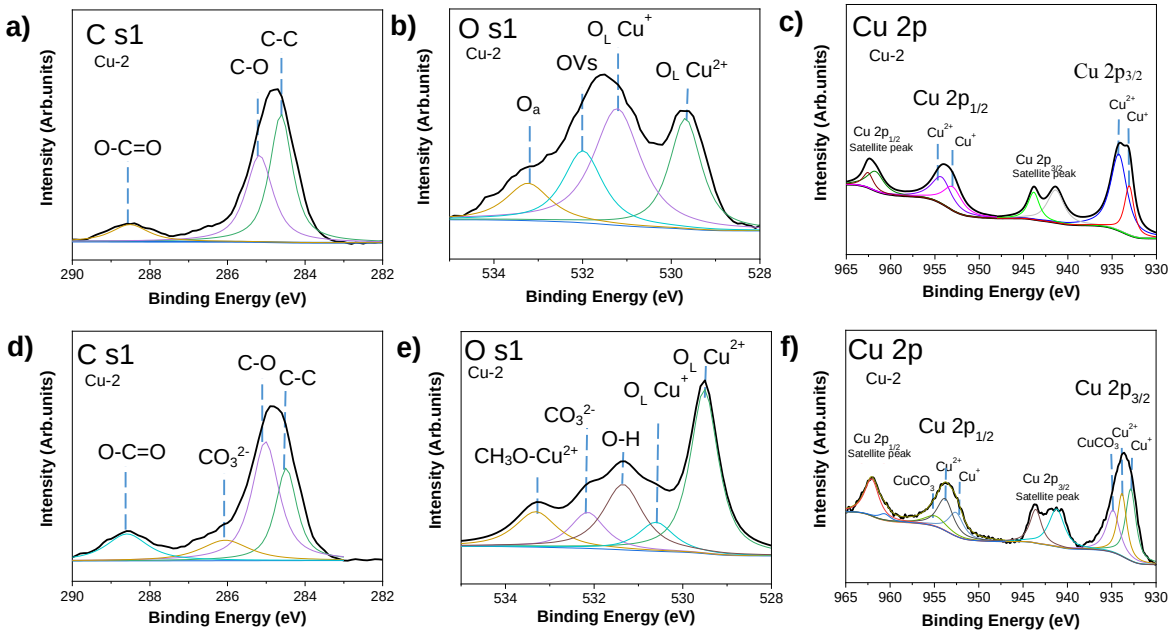

Figure 12. XPS spectra of Cu-2 film before and after the photocatalytic reaction for the element of a) and d) C 1s, b) and e) O 1s, c) and f) Cu 2p, respectively.

The surface analysis of Ni-3 before and after CO_2 reduction is shown in **Figure 13**. The C 1s spectrum of the film shows peaks at 284.4, 285.2, and 288.5 eV attributed to *sp*2 carbon components C–C, C-O, and O-C=O bonds, respectively (**Figure 13a**) [14, 55, 56]. These signals were due to the CO_2 adsorbed from the air. For the O1s spectrum (**Figure 13b),** three peaks were observed at 529.7, 530.5, and 531.4 eV, related to Ni^{2+} (O_L Ni^{2+}) of NiO [74], to oxygen adsorbed on the surface with low coordination (O_a) [61, 75], and Ni^{3+} (O_L Ni^{3+}) of Ni_2O_3 [76, 77], respectively. The Ni 2p spectrum in **Figure 13c** displays two edge splits by

spin-orbital coupling: i) the Ni $2p_{3/2}$ peak at 854.7 eV related with NiO [78], and ii) the $2p_{3/2}$ central peak at 855.7 eV and its satellite at 860.2 eV, evidencing the existence of Ni_2O_3 on the surface [77, 78]. This observation also explained the enhanced performance in PL (**Figure 6**) and the *p*-type characteristic of the sample, as shown in the transient chronoamperometry tests (**Figure 11**). After CO_2 reduction, Ni-3 film presented additional bands in the C 1s, Ni 2p, and O 1s spectra related to the presence of hydroxides, carbonates, or oxygen-containing hydrocarbons (**Figure 13d, e**) [68, 79]. The Ni 2p spectrum after the reaction showed the $2p_{3/2}$ at 855.7 eV, the $2p_{1/2}$ at 872.6 eV, and its satellite peak at 860.2 and 879.5 eV, respectively (**Figure 13f**). Also, additional bands in the O 1s spectrum were observed at 856.7 and 866.1 eV, suggesting the conversion of NiO to $Ni(OH)_2$ after the reaction [80]. According to these results, the formation $Ni(OH_2)$ species during the photocatalytic reaction promoted the hydroxylation of NiO phase and the dissolution of the NiO/Ni_2O_3 heterostructure. As a result, the photoreduction of CO_2 activity deactivated with time, as shown in **Figure 10**, which eventually decreased the charge transfer in the Ni-3 sample.

According to the results, the decrease of CH_4 or CO production by Cu-1 and Ni-3, respectively, was due to the carbonation occurred on the surface of the catalyst as discussed with **Figures 12** and **13**. These experiments gave a strong indication that no degradation occurred during CO_2 photoreduction reaction.

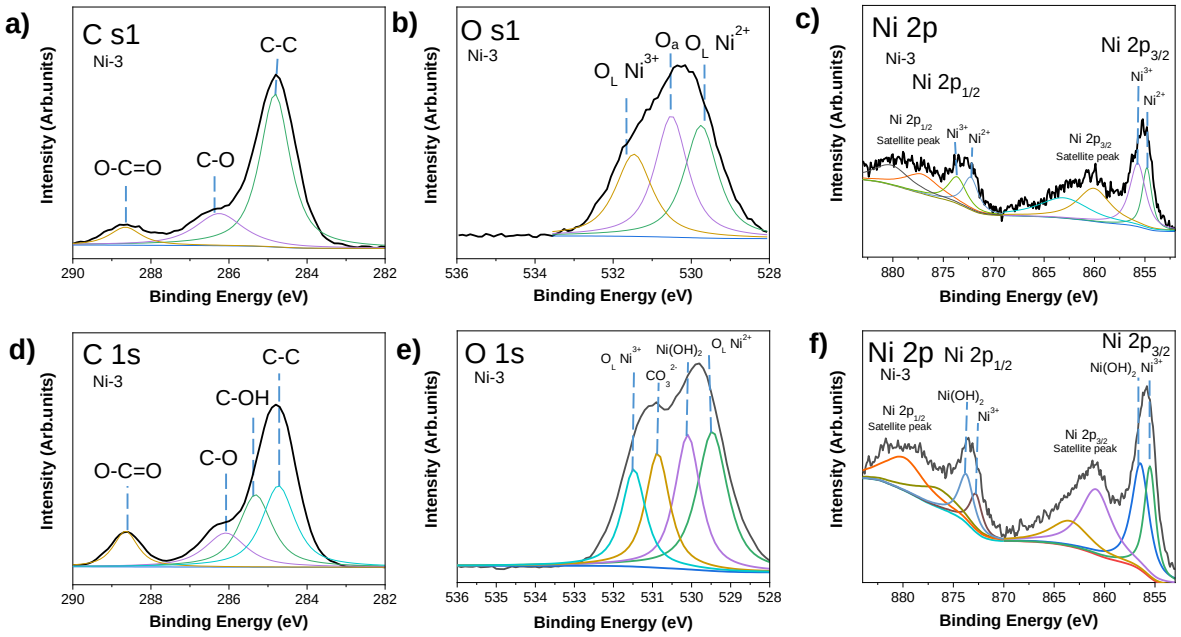

Figure 13. XPS spectra of Ni-3 film before and after the photocatalytic CO_2 reduction for the element of a) and d) C 1s, b) and e) O 1s, c) and f) Ni 2p, respectively.

3.5. Stability test

The stability of the optimized samples (Cu-2 and Ni-3) was conducted under a similar photocatalytic reduction of CO_2. Three consecutive runs were performed on each sample (**Figure S12**). The results revealed that copper oxides exhibited a stable CH_4 production after three consecutive cycles, whereas the CO production of Ni-3 coating deteriorated in each cycle significantly, around 28% in the second cycle and 42% in the third one.

After the tests, the morphology of the Cu-2 and Ni-3 samples was analyzed by SEM. After the test, the Ni-3 sample maintained its morphology of polyhedral particles, while the particles with flake morphology were not observed, as is shown in **Figure S13a**. On the contrary, the morphology of Cu-2 bars changed after the photocatalytic evaluation. **Figure S13b** shows that after the reaction, the bars tended to agglomerate with each other forming elongated

agglomerates, which could be related to the loss of active sites for the photocatalytic CO_2 reduction.

3.6. Photocatalytic CO_2 reduction in a batch reactor

The photocatalytic activity of the samples with the best performance in the continuous system (Cu-2 and Ni-3) was also evaluated in a batch reactor to investigate the formation of liquid solar fuels under LED visible-light (**Figure S14**). Both samples produced HCOOH and CH_3OH; however, traces of CH_2O were identified in both samples (<2 μmol g^{-1} h^{-1}). Cu-2 sample exhibited higher CH_3OH production (177 μmol g^{-1} h^{-1}) than Ni-3 sample (5 μmol g^{-1} h^{-1}). These results could be attributed to efficient charge transfer in the CuO/Cu_2O film, high affinity of CO_2 adsorption, and the type of carbonate adsorbed species. Formic acid was also identified, which production was better in the Ni-3 sample (4245 μmol g^{-1} h^{-1}) compared with the Cu-2 sample (1450 μmol g^{-1} h^{-1}). These results confirm that the charge transfer efficiency and the CO_2 affinity are important factors to obtain hydrocarbons of higher molecular weights, since the use of NiO/Ni_2O_3 promote the formation of CO and HCOOH in the gas and liquid phases, respectively. Because these reactions just required two electrons to occur. The liquid products obtained from the photocatalytic evaluation of Cu-2 were confirmed and monitored by ^1H NMR (**Figure S15**). It was possible to corroborate the presence of methanol at 3.6 ppm in the sample and ethanol at 3.4 ppm. The observed concentrations are of the same order of magnitude as those liquid samples analyzed using GC. With this technique was not possible to identify the presence of CH_2O and HCOOH due to its detection limit (<2 ppm). Also, for comparative purposes, TiO_2 P-25 was evaluated under the same experimental conditions in the liquid phase. This reference sample only promoted the formation of HCOOH

(81 μmol g^{-1} h^{-1}), and other products were not detected. These results confirm the better photocatalytic activity of the earth-abundant photocatalyst proposed in this work.

3.7. Photocatalytic mechanism

The photocatalytic proposed for the CO_2 reduction mechanism on the surface of the Cu-2 and Ni-3 sample was illustrated in **Figure 14**. The theoretical potential of the conduction band of Cu_2O is more negative (-0.4 eV) than that of CuO (0.3 eV). Therefore, the electrons (e^-) of the valence band of Cu_2O are transferred to the conduction band of CuO generating a hole (h^+) in the first band, which reacts with the CO_2 and H_2O molecules adsorbed on its surface (**Figure 14a I**). In the proposed mechanism, the presence of Na_2O in the substrate, represented as a gray circle, provides an extra active site where the CO_2 adsorption occurs. This phenomenon was corroborated by analyzing the Na1s spectrum after and before the photocatalytic reaction, which evidences the formation of Na_2CO_3 after its interaction with the CO_2 molecule. Once the carbonates are captured on the photocatalytic device (Metal oxides/Substrate), the photogenerated electrons can proceed to reduce this species onto C1 products (**Figure 14a II**). In an initial step, the CO_2 molecule is adsorbed on the heterostructure surface, forming mono and bidentate species (as it was previously demonstrated by FTIR analysis); at the beginning of the reaction, electrons are transferred from Cu_2O to CuO and then to the adsorbed species (**Figure 14a III**). CO_2 can be physisorbed as a linear molecule or chemisorbed as a partly charged $CO_2^{\delta-}$ species via interactions with surface atoms. Three different coordination systems have been proposed for CO_2 molecules adsorbed on a photocatalyst surface:

1. First, the positively charged carbon atom may behave as a Lewis acid, accepting electrons from Lewis's base centers such as oxide ions and forming a carbonate-like species (**Figure S16a**).

2. Second, as illustrated in **Figure S16b**, the oxygen atoms in CO_2 have lone pairs of electrons that can be transported to the Lewis acid centers on the surface.

3. Thirdly, the oxygen and carbon atoms of the CO_2 molecule can act as electron donors and acceptors, resulting in a mixed coordination structure, as is shown in **Figure S16c**.

The mechanism for the formation of C1 products such as CH_3OH and CH_4 can occur by different routes [50]. The first route is by forming *CO and subsequent hydrogenation to *CHO, *CH_2O (which desorbs as HCHO), and *CH_3O (methoxy). Additionally, the intermediate *CH_3O may convert to CH_4, leaving *O on the surface, which would evolve into H_2O. Another way to form CH_4 also originates from the formation of *CO on the surface. This intermediate is hydrogenated to form *COH on the surface, subsequently dehydrated to form *C. Via step-by-step hydrogenation, this intermediate forms CH_4. An additional mechanism that differs from these two pathways could also occur. Rather than forming *CO initially, this pathway begins with the bidentate coordination of CO_2*$^-$ via the oxygen atoms, followed by the generation of HCO_2, H_2OCO*, and *CHO. This mechanism is referred to as the carbene pathway [50]. On the other hand, the Ni-based coatings only produce CO and HCOOH due to their lower affinity to adsorbed CO_2. Based on the results, it is proposed that the reaction mechanism follows the carbene route since it was possible to identify by XPS residual species such as CH_3O-Cu^{2+}, which is an intermediate in the production of methanol and methane.

On the other hand, the proposed mechanism of the photocatalytic reactions that take place in the Ni-3 coating is illustrated in **Figure 14b**. Like that of the Cu-2 film, the photoreduction process begins once CO_2 is adsorbed. Electrons are transferred from the conduction band of NiO to Ni_2O_3 according to their theoretical CB potentials, e.g., -0.34 and 0.07 V vs NHE, respectively. In this mechanism, NiO acts as an electron donor in which the photoexcited

electrons could be transferred to the CO_2 adsorbed on the Ni_2O_3 surface, producing CO following the pathway for C_1 products [81]. Due to the relatively low amount of photogenerated electrons in the NiO conduction band, a small amount of these is transferred to the Ni_2O_3. Then, the electrons photogenerated in Ni_2O_3 (small black particles) are transferred to the Ni-O = C = O species (**Figure 14b I**). According to the results shown in the FTIR spectrum, the lower affinity for CO_2 on NiO could promote a rapid desorption of carbonate species, which favored the formation of CO and HCOOH in the gas and liquid phase, respectively. Furthermore, the minor current density indicates that the NiO/Ni_2O_3 heterostructure did not provide enough electrons for CO_2 photoreduction to methane or methanol. Additionally, the presence of Ni_2O_3 could favor de charge transfer due to the formation of a type-II heterostructure, while the presence of Na_2O, also help to prevents the re-oxidation of the products (**Figure 14b II.**). A closer view of this mechanism is shown in **Figure 14b III**, in which the CO or HCOOH production starts when the CO_2 molecule is adsorbed on the NiO surface. Of note, when the surface of NiO interacts with water, it could form $Ni(OH)_2$ on the surface, which would reduce the photocatalytic activity of the heterostructure.

In both mechanisms, the H_2 generation is suppressed by the higher affinity of CO_2 for the protons (H^+) generated in the valence band of the semiconductors, as is shown in **Figure S5c**.

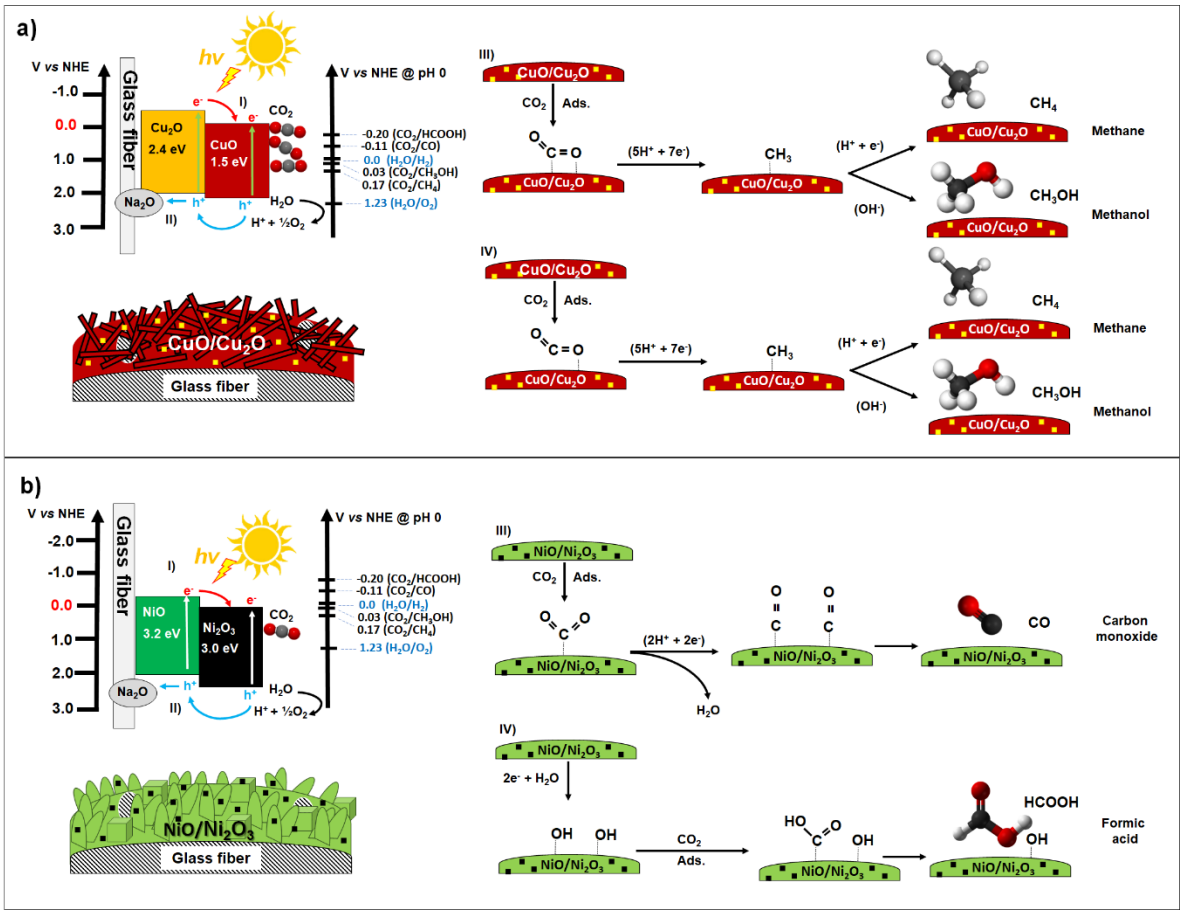

Figure 14. Schematic diagram of proposed mechanisms for the photocatalytic CO_2 reduction in a) Cu-2 (CuO/Cu_2O) and b) Ni-3 (NiO/Ni_2O_3) samples.

4. Conclusions

Heterostructured Cu_xO (x = 1 and 2) and Ni_xO_y (x=1 and 2, y=1 and 3) coatings on flexible substrates were obtained by an *in-situ* microwave-hydrothermal method using glucose as a reductive agent at 80 °C for 1 h. The coatings exhibited photocatalytic activity to convert CO_2 into value-added products, such as CH_4 and CO in a continuous system under UV-Visible light and CH_3OH and HCOOH in a batch reactor under visible light. The CuO/Cu_2O coatings were selective towards CH_4 and CH_3OH; meanwhile NiO/Ni_2O_3 preferably produced CO and HCOOH.

The highest CH_4 production with CuO/Cu_2O coatings was 94 μmol g^{-1} h^{-1}, which was 32 times higher than previous studies in the literature using a simple or binary oxides of coatings. The superior CO_2 photoreduction was attributed to the high affinity for CO_2 and an efficient charge transfer in the CuO/Cu_2O heterostructure. On the other hand, Ni_xO_y coatings showed a much lower affinity to CO_2 adsorption and less efficient charge transfer than CuO/Cu_2O coatings, producing lighter products: CO in the continuous reactor and HCOOH in the batch reactor. Also, the stability in these samples was lower than the copper oxide coatings due to the conversion of NiO/Ni_2O_3 to $NiO/Ni(OH)_2$, as evidenced in XPS.

5. Acknowledgments

The authors wish to thank CONACYT for financial support for this research through the following projects: Cátedras CONACYT 1060, CONACYT-FC-1725, and Paradigmas y Fronteras de la Ciencia 320379. Also, the authors thank to UANL for its support by PAICYT projects. Manuel Alejandro Ávila López wants to thank CONACYT for the PhD scholarship. In addition, the authors want to thank to M.C Luis Gerardo Silva Vidaurri from CIMAV for his help with the XPS analysis.

UK Catalysis Hub is kindly thanked for resources and support provided via the membership of the UK Catalysis Hub Consortium and funded by current EPSRC grants: EP/R026939/1 and EP/R026815/1. The authors would like to thank Dr. Leila Negahdar, Dr. June Callison, Dr. Nitya Ramanan, and Prof. Andrew M. Beale for their great help and support during the DRIFTS experiments. The authors also thank the financial support provided by the UK Engineering and Physical Sciences Research Council (EP/K021796/1). They are also grateful for the support provided by the Research Centre for Carbon Solutions (RCCS) and the Buchan Chair in Sustainable Energy Engineering at Heriot-Watt University.

6. References

[1] J. Bradshaw, Z. Chen, A. Garg, D. Gomez, H.-H. Rogner, D. Simbeck, R. Williams, in: B. Metz, O. Davidson, de C. Heleen, M. Loos, L. Meyer (Eds.), Carbon Dioxide Capture and Storage, Intergovernmental Panel on Climate Change, Canada, 2009, pp. 75–104.

[2] Q. Wang, J. Luo, Z. Zhong, A. Borgna, CO2 capture by solid adsorbents and their applications: current status and new trends, Energy Environ. Sci. 4 (2011) 42–55. https://doi.org/10.1039/C0EE00064G

[3] Y. Wang, L. Zhao, A. Otto, M. Robinius, D. Stolten, A Review of Post-combustion CO2 Capture Technologies from Coal-fired Power Plants, Energy Procedia 114 (2017) 650–665. https://doi.org/10.1016/j.egypro.2017.03.1209

[4] W. Tu, Y. Zhou, Z. Zou, Photocatalytic Conversion of CO2 into Renewable Hydrocarbon Fuels: State-of-the-Art Accomplishment, Challenges, and Prospects, Adv. Mater 26 (2014) 4607-4626. https://doi.org/10.1002/adma.201400087

[5] Ž. Kovačič, B. Likozar, M. Huš, Photocatalytic CO2 Reduction: A Review of Ab Initio Mechanism, Kinetics, and Multiscale Modeling Simulations, ACS Catal. 10 (2020) 14984-15007. https://doi.org/10.1021/acscatal.0c02557

[6] J. Fu, K. Jiang, X. Qiu, J. Yu, M. Liu, Product selectivity of photocatalytic CO2 reduction reactions, Mater. Today 32 (2020) 222-243. https://doi.org/10.1016/j.mattod.2019.06.009

[7] W.A. Thompson, A. Olivo, D. Zanardo, G. Cruciani, F. Menegazzo, M. Signoretto, M.M. Maroto-valer, Systematic study of TiO2/ZnO mixed metal oxides for CO2 photoreduction, RSC Adv 9 (2019) 21660–21666. https://doi.org/10.1039/C9RA03435H

[8] Z.-Y. Wang, H.-C. Chou, J.C.S. Wu, D.P. Tsai, G. Mul, CO2 photoreduction using NiO/InTaO4 in optical-fiber reactor for renewable energy, Appl. Catal. A 380 (2010) 172–177. https://doi.org/10.1016/j.apcata.2010.03.059

[9] A.E. Nogueira, J.A. Oliveira, G.T.S.T. da Silva, C. Ribeiro, Insights into the role of CuO in the CO2 photoreduction process, Sci. Rep. 9 (2019) 1316. https://doi.org/10.1038/s41598-018-36683-8

[10] Z. Xiong, Z. Lei, C.-C. Kuang, X. Chen, B. Gong, Y. Zhao, J. Zhang, C. Zheng, J.C.S. Wu, Selective photocatalytic reduction of CO2 into CH4 over Pt-Cu2O TiO2 nanocrystals: The interaction between Pt and Cu2O cocatalysts, Appl. Catal. B Environ. 202 (2017) 695–703. https://doi.org/10.1016/j.apcatb.2016.10.001

[11] J.Y. Do, B.S. Kwak, S.-M. Park, M. Kang, Effective Carbon Dioxide Photoreduction over Metals (Fe-, Co-, Ni-, and Cu-) Incorporated TiO2/Basalt Fiber Films, Int. J. Photoenergy 2016 (2016) 1–12. https://doi.org/10.1155/2016/5195138

[12] J.Z.Y. Tan, Y. Fernández, D. Liu, M. Maroto-Valer, J. Bian, X. Zhang, Photoreduction of CO2 using copper-decorated TiO2 nanorod films with localized surface plasmon behavior, Chem. Phys. Lett. 531 (2012) 149–154. https://doi.org/10.1016/j.cplett.2012.02.016

[13] J.-C. Wang, L. Zhang, W. Fang, J. Ren, Y.-Y. Li, H. Yao, J. Wang, Z. Li, Enhanced Photoreduction CO2 Activity over Direct Z-Scheme α-Fe2O3/Cu2O Heterostructures under Visible Light Irradiation, ACS Appl. Mater. Interfaces 7 (2015) 8631–8639. https://doi.org/10.1021/acsami.5b00822

[14] M.A. Ávila-López, E. Luévano-Hipólito, L.M. Torres-Martínez, CO2 adsorption and its visible-light-driven reduction using CuO synthesized by an eco-friendly sonochemical method, J. Photochem. Photobiol. A Chem. 382 (2019) 111933. https://doi.org/10.1016/j.jphotochem.2019.111933

[15] Y. Li, W.-N. Wang, Z. Zhan, M.-H. Woo, C.-Y. Wu, P. Biswas, Photocatalytic reduction of CO2 with H2O on mesoporous silica supported Cu/TiO2 catalysts, Appl. Catal. B Environ. 100 (2010) 386–392. https://doi.org/10.1016/j.apcatb.2010.08.015

[16] Y. Yan, Y. Yu, C. Cao, S. Huang, Y. Yang, X. Yang, Y. Cao, Enhanced photocatalytic activity of TiO2–Cu/C with regulation and matching of energy levels by carbon and copper for photoreduction of CO2 into CH4, CrystEngComm 18 (2016) 2956–2964. https://doi.org/10.1039/C6CE00117C

[17] M. Tahir, B. Tahir, N. A. S. Amin, A. Muhammad, Photocatalytic CO2 methanation over NiO/In2O3 promoted TiO2 nanocatalysts using H2O and/or H2 reductants, Energy Conversion and Management 119 (2016) 368-378. https://doi.org/10.1016/j.enconman.2016.04.057

[18] C. Han, R. Zhang, Y. Ye, L. Wang, Z. Ma, F. Su, H. Xie, Y. Zhou, P.K. Wong, L. Ye, Chainmail co-catalyst of NiO shell-encapsulated Ni for improving photocatalytic CO2 reduction over g-C3N4, J. Mater. Chem. A 7 (2019) 9726–9735. https://doi.org/10.1039/C9TA01061K

[19] A.M. Huerta-Flores, E. Luévano-Hipólito, Leticia M. Torres-Martínez, A.T. Sánchez, Photocatalytic H2 production and CO2 reduction on Cu, Ni‑ doped ZnO: effect of metal doping and oxygen vacancies, J. Mater. Sci. Mater. Electron. (2019) 1–13. https://doi.org/10.1039/C9TA01061K

[20] L. Liu, H. Zhao, J.M. Andino, Y. Li, Photocatalytic CO2 Reduction with H2O on TiO2 Nanocrystals: Comparison of Anatase, Rutile, and Brookite Polymorphs and Exploration of Surface Chemistry, Catal. ACS 2 (2012) 1817–1828. https://doi.org/10.1021/cs300273q

[21] M. Tasbihi, F. Fresno, U. Simon, I.J. Villar-García, V. Pérez-Dieste, C. Escudero, V.A. de la Peña O'Shea, On the selectivity of CO2 photoreduction towards CH4 using Pt/TiO2 catalysts supported on mesoporous silica, Appl. Catal. B Environ. 239 (2018) 68–76. https://doi.org/10.1016/j.apcatb.2018.08.003

[22] B.S. Kwak, K.M. Kim, S.-M. Park, M. Kang, Synthesis of basalt fiber@Zn1-xMgxO core/shell nanostructures for selective photoreduction of CO2 to CO, Appl. Surf. Sci. 407 (2017) 109–116. https://doi.org/10.1016/j.apsusc.2017.02.178

[23] M. Tahir, B. Tahir, N.A.S. Amin, A. Muhammad, Photocatalytic CO2 methanation over NiO/In2O3 promoted TiO2 nanocatalysts using H2O and/or H2 reductants, Energy Convers. Manag. 119 (2016) 368–378. https://doi.org/10.1016/j.enconman.2016.04.057

[24] N. Jantarasorn, O. Mekasuwandumrong, P. Kelly, P. Praserthdam, Reactive Magnetron Sputter Deposition of Copper on TiO2 Support for Photoreduction of CO2 to CH4, IOP Conf. Ser. Mater. Sci. Eng. 559 (2019) 012017. https://doi.org/10.1088/1757-899X/559/1/012017

[25] J.Y. Do, Y. Im, B.S. Kwak, S.-M. Park, M. Kang, Dramatic CO2 photoreduction with H2O vapors for CH4 production using the TiO2 (bottom)/Fe–TiO2 (top) double-layered films, Ceram. Int. 42 (2016) 5942–5951. https://doi.org/10.1016/j.cej.2015.03.066

[26] Y. Im, S.-M. Park, M. Kang, Effect of Ca/Ti Ratio on the Core-Shell Structured

CaTiO3@basalt Fiber for Effective Photoreduction of Carbon Dioxide, Bull. Korean Chem. Soc. 38 (2017) 397–400. https://doi.org/10.1002/bkcs.11100

[27] A.A. Beigi, S. Fatemi, Z. Salehi, Synthesis of nanocomposite CdS/TiO2 and investigation of its photocatalytic activity for CO2 reduction to CO and CH4 under visible light irradiation, J CO2 Util. 7 (2014) 23–29. https://doi.org/10.1016/j.jcou.2014.06.003

[28] J. Kim, J.Y. Do, N.K. Park, S.J. Lee, J.P. Hong, M. Kang, Photoreduction of CO2 into CH4 using Bi2S3-TiO2 double-layered dense films, Korean J. Chem. Eng. 35 (2018) 1089–1098. https://doi.org/10.1007/s11814-018-0007-y

[29] A. Olivo, E. Ghedini, M. Signoretto, Matteo Compagnoni, Ilenia Rossetti, Liquid vs. Gas Phase CO2 Photoreduction Process: Which Is the Effect of the Reaction Medium?, Energies 10 (2017) 1394. http://dx.doi.org/10.3390/en10091394

[30] A. Olivo, D. Zanardo, E. Ghedini, F. Menegazzo, M. Signoretto, Solar Fuels by Heterogeneous Photocatalysis: From Understanding Chemical Bases to Process Development, Chemengineering 2 (2018) 42. http://dx.doi.org/10.3390/chemengineering2030042

[31] T. Baran, A. Visibile, M. Busch, X. He, S. Wojtyla, S. Rondinini, A. Minguzzi, A. Vertova, Copper Oxide-Based Photocatalysts and Photocathodes: Fundamentals and Recent Advances. Molecules 26 (2021) 7271. https://doi.org/10.3390/molecules26237271

[32] A. I. Vaizogullar, Facile preparation and characterization of NiO/Ni2O3-decorated nanoballs and mixed phase CdS nano rods (CdS&NiO/Ni2O3) for effective photocatalytic decomposition of Congo red under visible light irradiation, J. Dispers. Sci. Technol. 42 (2021) 1408-1418. https://doi.org/10.1080/01932691.2020.1814804

[33] M.A. Ávila-López, E. Luévano-Hipólito, L.M. Torres-Martínez, CuO coatings on glass fibers: a hybrid material for CO2 adsorption and photocatalytic reduction to solar fuels,

J. Mater. Sci. Mater. Electron. 32 (2020) 11336–11337. https://doi.org/10.1007/s10854-020-03955-x

[34] W. A. Thompson, A. Olivo, D. Zanardo, G. Cruciani, F. Menegazzo, M. Signoretto, M. Mercedes Maroto-Valer, Systematic study of TiO2/ZnO mixed metal oxides for CO2 photoreduction, RSC Advances 9 (2019) 21660-21666. https://doi.org/10.1039/C9RA03435H

[35] A. Soman, Y. Qiu, Q. Chan Li, HPLC-UV Method Development and Validation for the Determination of Low Level Formaldehyde in a Drug Substance, J. Chromatogr. Sci. 46 (2008) 461–465. https://doi.org/10.1093/chromsci/46.6.461

[36] D. Hasan, I. Mahmood, I. Ahmad, F. Aziz, I. Ahmad, Development of an HPLC Method for Formic Acid Analysis through Peak Exclusion Approach, Sains Malaysiana 48 (2019) 1011–1018. http://dx.doi.org/10.17576/jsm-2019-4805-09

[37] S. Banerjee, D. Chakravorty, Optical absorption by nanoparticles of Cu2O, Europhys. Lett. 52 (2000) 468–473. https://dx.doi.org/10.1209/epl/i2000-00461-5

[38] M. Hashem, E. Saion, N.M. Al-hada, H.M. Kamari, A.H. Shaari, Z.A. Talib, S.B. Paiman, M.A. Kamarudeen, Results in Physics Fabrication and characterization of semiconductor nickel oxide (NiO) nanoparticles manufactured using a facile thermal treatment, Results Phys. 6 (2016) 1024–1030. https://doi.org/10.1016/j.rinp.2016.11.031

[39] A. Molla, M. Sahu, S. Hussain, Synthesis of Tunable Band Gap Semiconductor Nickel Sulphide Nanoparticles: Rapid and Round the Clock Degradation of Organic Dyes Sci. Rep. 6 (2016) 26034. https://doi.org/10.1038/srep26034

[40] A. Renaud, B. Chavillon, L. Cario, L. Le Pleux, N. Szuwarski, Y. Pellegrin, E. Blart, E. Gautron, F. Odobel, S. Jobic, Origin of the Black Color of NiO Used as Photocathode in pType Dye-Sensitized Solar Cell, J. Phys. Chem. C 117 (2013) 22478–22483. https://doi.org/10.1021/jp4055457

[41] X. Zhao, P. Wang, Z. Yan, N. Ren, Room temperature photoluminescence properties of CuO nanowire arrays, Opt. Mater. 42 (2015) 544–547. https://doi.org/10.1016/j.optmat.2014.12.032

[42] X.X. Jiang, X. De Hu, M. Tarek, P. Saravanan, R. Alqadhi, S.Y. Chin, M.M. Rahman Khan, Tailoring the properties of g-C3N4 with CuO for enhanced photoelectrocatalytic CO2 reduction to methanol, J. CO2 Util. 40 (2020) 101222. https://doi.org/10.1016/j.jcou.2020.101222

[43] L. Kumari, W.Z. Li, C.H. Vannoy, R.M. Leblanc, D.Z. Wang, Vertically aligned and interconnected nickel oxide nanowalls fabricated by hydrothermal route, Cryst. Res. Technol. 44 (2009) 495–499. https://doi.org/10.1002/crat.200800583

[44] H. Du, C.T. Williams, A.D. Ebner, J.A. Ritter, In Situ FTIR Spectroscopic Analysis of Carbonate Transformations during Adsorption and Desorption of CO2 in K-Promoted HTlc Chem. Mater. 22 (2010) 3519–3526. https://doi.org/10.1021/cm100703e

[45] Y. Liu, Y. Yang, Q. Sun, Z. Wang, B. Huang, Y. Dai, X. Qin, X. Zhang, Chemical Adsorption Enhanced CO2 Capture and Photoreduction over a Copper Porphyrin Based Metal Organic Framework, ACS Appl. Mater. Interfaces 5 (2013) 7654–7658. https://doi.org/10.1021/am4019675

[46] A. Hakim, T.S. Marliza, N.M. Abu Tahari, R.W.N. Wan Isahak, R.M. Yusop, W.M. Mohamed Hisham, A.M. Yarmo, Studies on CO2 Adsorption and Desorption Properties from Various Types of Iron Oxides (FeO, Fe2O3, and Fe3O4), Ind. Eng. Chem. Res. 55 (2016) 7888–7897. https://doi.org/10.1021/acs.iecr.5b04091

[47] W.N.R.W. Isahak, Z.A.C. Ramli, M.W. Ismail, K. Ismail, R.M. Yusop, M.W.M. Hisham, M.A. Yarmo, Adsorption–desorption of CO2 on different type of copper oxides surfaces: Physical and chemical attractions studies, J. CO2 Util. 2 (2013) 8–15. https://doi.org/10.1016/j.jcou.2013.06.002

[48] L. Liu, C. Zhao, J. Xu, Y. Li, Integrated CO2 capture and photocatalytic conversion by a hybrid adsorbent/photocatalyst material, Appl. Catal. B Environ. 179 (2015) 489–499. https://doi.org/10.1016/j.apcatb.2015.06.006

[49] Y. Kato, M. Yamamoto, M. Akatsuka, R. Ito, A. Ozawa, Y. Kawaguchi, T. Tanabe, T. Yoshida, Study on carbon dioxide reduction with water over metal oxide photocatalysts Surf. Interface Anal. 51 (2019) 40–45. http://dx.doi.org/10.1002/sia.6542

[50] S.N. Habisreutinger, L. Schmidt-Mende, J.K. Stolarczyk, Photocatalytic Reduction of CO2 on TiO2 and Other Semiconductors, Angew. Chemie Int. Ed. 52 (2013) 7372–7408. https://doi.org/10.1002/anie.201207199

[51] Manuel Alejandro Ávila-López, Stelios Gavrielides, Xiao Jiao Luo, Abah Ezra Ojoajogwu, Jeannie Z. Y. Tan, E. Luévano-Hipólito, Leticia M. Torres-Martínez, M. Mercedes Maroto-Valer, Comparative study of CO2 photoreduction using different conformations of CuO photocatalyst: Powder, coating on mesh and thin film, Journal of CO2 Utilization 50 (2021) 101588. doi.org/10.1016/j.jcou.2021.101588

[52] E. Korovin, D. Selishchev, D. Kozlov, Photocatalytic CO2 Reduction on the TiO2 P25 Under the High Power UV-LED Irradiation, Top. Catal. 59 (2016) 1292–1296. https://link.springer.com/article/10.1007/s11244-016-0651-6

[53] N. Põldme, L. O'Reilly, I. Fletcher, J. Portoles, I. V. Sazanovich, M. Towrie, C. Long, J.G. Vos, M.T. Pryce, E.A. Gibson, Photoelectrocatalytic H2 evolution from integrated photocatalysts adsorbed on NiO, Chem. Sci. 10 (2019) 99–112. https://doi.org/10.1039/C8SC02575D

[54] M. Fingerle, S. Tengeler, W. Calvet,z W. Jaegermann, T. Mayer, Sputtered Nickel Oxide Thin Films on n-Si(100)/SiO2 Surfaces for Photo-Electrochemical Oxygen Evolution Reaction (OER): Impact of Deposition Temperature on OER Performance and on Composition before and after OER, J. Electrochem. Soc. 167 (2020) 136514.

[55] H. Jensen, A. Soloviev, Z. Li, E.G. Søgaard, XPS and FTIR investigation of the surface properties of different prepared titania nano-powders, Appl. Surf. Sci. 246 (2005) 239–249. https://doi.org/10.1016/j.apsusc.2004.11.015

[56] Y. Wang, Y. Jin, M. Jia, Ultralong Fe3O4 nanowires embedded graphene aerogel composite anodes for lithium ion batteries, Mater. Lett. 228 (2018) 395–398. https://doi.org/10.1016/j.matlet.2018.06.077

[57] Y. Min, T. Wang, Y. Chen, Microwave-assistant synthesis of ordered CuO microstructures on Cu substrate, Appl. Surf. Sci. 257 (2010) 132–137. https://doi.org/10.1016/j.apsusc.2010.06.049

[58] Y. Wang, Y. Lü, W. Zhan, Z. Xie, Q. Kuang, L. Zheng, Synthesis of porous Cu2O/CuO cages using Cu-based metal–organic frameworks as templates and their gas-sensing properties, J. Mater. Chem. A 3 (2015) 12796–12803. https://doi.org/10.1039/C5TA01108F

[59] H. Yu, J. Li, Y. Zhang, S. Yang, K. Han, F. Dong, T. Ma, H. Huang, Three-in-One Oxygen Vacancies: Whole Visible-Spectrum Absorption, Efficient Charge Separation, and Surface Site Activation for Robust CO 2 Photoreduction, Angew. Chemie - Int. Ed. 58 (2019) 3880–3884. https://doi.org/10.1002/anie.201813967

[60] Z.P. Nie, D.K. Ma, G.Y. Fang, W. Chen, S.M. Huang, Concave Bi2WO6 nanoplates with oxygen vacancies achieving enhanced electrocatalytic oxygen evolution in near-neutral water, J. Mater. Chem. A 4 (2016) 2438–2444. https://doi.org/10.1039/C5TA09536K

[61] S. Jaiswar, K.D. Mandal, Evidence of Enhanced Oxygen Vacancy Defects Inducing Ferromagnetism in Multiferroic CaMn7O12 Manganite with Sintering Time, J. Phys. Chem. C 121 (2017) 19586–19601. https://doi.org/10.1021/acs.jpcc.7b05415

[62] Y. Zhao, M. Ikram, J. Zhang, K. Kan, H. Wu, W. Song, L. Li, K. Shi, Outstanding Gas Sensing Performance of CuO-CNTs Nanocomposite Based on Asymmetrical Schottky Junctions, Appl. Surf. Sci. 428 (2018) 415–421. http://dx.doi.org/10.1016/j.apsusc.2017.09.173

[63] J. Park, K. Lim, R.D. Ramsier, Y.-C. Kang, Spectroscopic and Morphological Investigation of Copper Oxide Thin Films Prepared by Magnetron Sputtering at Various Oxygen Ratios, Bull. Korean Chem. Soc. 32 (2011) 3395–3399. http://dx.doi.org/10.5012/bkcs.2011.32.9.3395

[64] L. Yang, D. Chu, L. Wang, X. Wu, J. Luo, Synthesis and photocatalytic activity of chrysanthemum-like Cu2O/Carbon Nanotubes nanocomposites, Ceram. Int. 42 (2016) 2502–2509. https://doi.org/10.1016/j.ceramint.2015.10.051

[65] K. Ozawa, Y. Oba, K. Edamoto, Formation and characterization of the Cu2O overlayer on Zn-terminated ZnO(0 0 0 1), Surf. Sci. 603 (2009) 2163–2170. http://dx.doi.org/10.1016/j.susc.2009.04.027

[66] K. Habermehl-Ćwirzeń, J. Lahtinen, P. Hautojärvi, Methanol on Co(0 0 0 1): XPS, TDS, WF and LEED results, Surf. Sci. 598 (2005) 128–135. https://doi.org/10.1016/j.susc.2005.08.033

[67] J.M. Montero, M.A. Isaacs, A.F. Lee, J.M. Lynam, K. Wilson, The surface chemistry of nanocrystalline MgO catalysts for FAME production: an in situ XPS study of H2O, CH3OH and CH3OAc adsorption, Surf. Sci. 646 (2016) 170–178. https://doi.org/10.1016/j.susc.2015.07.011

[68] S. Röhe, K. Frank, A. Schaefer, A. Wittstock, V. Zielasek, A. Rosenauer, M. Bäumer, CO oxidation on nanoporous gold: A combined TPD and XPS study of active catalysts, Surf. Sci. 609 (2013) 106–112. http://dx.doi.org/10.1016/j.susc.2012.11.011

[69] B.K. Deka, K. Kong, J. Seo, D. Kim, Y. Park, H.W. Park, Controlled growth of CuO nanowires on woven carbon fibers and effects on the mechanical properties of woven carbon fiber/polyester composites, Compos. Part A Appl. Sci. Manuf. 69 (2015) 56–63. https://doi.org/10.1016/j.compositesa.2014.11.001

[70] Y. Wang, H. Xiang, C. Yang, D. Liu, Corrosion Resistance of Copper-bearing Duplex Stainless Steel in Culture Medium without and with Bacteria, J. Chinese Soc. Corros. Prot. 34 (2014) 558–565. https://doi.org/10.11902/1005.4537.2013.184

[71] S. Wu, Y. Qiao, K. Jiang, Y. He, S. Guo, H. Zhou, Tailoring Sodium Anodes for Stable Sodium-Oxygen Batteries, Adv. Funct. Mater. 28 (2018) 1706374. https://doi.org/10.1002/adfm.201706374

[72] D. McNulty, D. Noel Buckley, C. O'Dwyer, NaV2O5 from Sodium Ion-Exchanged Vanadium Oxide Nanotubes and Its Efficient Reversible Lithiation as a Li-Ion Anode Material, ACS Appl. Energy Mater. 2 (2019) 822–832. https://doi.org/10.1021/acsaem.8b01895

[72] P.C. Kao, J.Y. Wang, J.H. Lin, S.H. Chen, Enhancement of Electron Injection in Organic Light Emitting Diodes Using an Ultrathin Sodium Carbonate Buffer Layer, J. Electrochem. Soc. 157 (2010) 1–5. http://dx.doi.org/10.1149/1.3305947

[73] J.F. Moulder, W.F. Stickle, P.E. Sobol, K.D. Bomben, Handbook of X-Ray Photoelectron Spectroscopy, John Wiley & Sons, Ltd, Chichester, UK, 2005, pp. 50–51.

[74] V.V. Kaichev, A.Y. Gladky, I.P. Prosvirin, A.A. Saraev, M. Hävecker, A. Knop-Gericke, R. Schlögl, V.I. Bukhtiyarov, In situ XPS study of self-sustained oscillations in catalytic oxidation of propane over nickel, Surf. Sci. 609 (2013) 113–118. https://doi.org/10.1016/j.susc.2012.11.012

[75] S.-B. Lee, J.-H. Boo, W.-S. Ahn, XPS Studies of Oxygen Adsorption on Polycrystalline Nickel Surface, Bull. Korean Chem. Soc. 8 (1987) 358–362.

[76] Q. Liu, Q. Chen, Q. Zhang, Y. Xiao, X. Zhong, G. Dong, M.-P. Delplancke-Ogletree, H. Terryn, K. Baert, F. Reniers, X. Diao, In situ electrochromic efficiency of a nickel oxide

thin film: origin of electrochemical process and electrochromic degradation, J. Mater. Chem. C 6 (2018) 646–653. https://doi.org/10.1039/C7TC04696K

[77] H. Lin, B. Sun, H. Wang, Q. Ruan, Y. Geng, Y. Li, J. Wu, W. Wang, J. Liu, X. Wang, Unique 1D Cd1−xZnxS@O-MoS2/NiOx Nanohybrids: Highly Efficient Visible-Light-Driven Photocatalytic Hydrogen Evolution via Integrated Structural Regulation, Small 15 (2019) 1804115. https://doi.org/10.1002/smll.201804115

[78] N. Weidler, J. Schuch, F. Knaus, P. Stenner, S. Hoch, A. Maljusch, R. Schäfer, B. Kaiser, W. Jaegermann, X-ray Photoelectron Spectroscopic Investigation of Plasma-Enhanced Chemical Vapor Deposited NiOx, NiOx(OH)y, and CoNiOx(OH)y: Influence of the Chemical Composition on the Catalytic Activity for the Oxygen Evolution Reaction, J. Phys. Chem. C 121 (2017) 6455–6463. https://doi.org/10.1021/acs.jpcc.6b12652

[79] D.H. Kim, M.C. Jung, S.H. Cho, S.H. Kim, H.Y. Kim, H.J. Lee, K.H. Oh, M.W. Moon, UV-responsive nano-sponge for oil absorption and desorption, Sci. Rep. 5 (2015) 1–12. http://dx.doi.org/10.1038/srep12908

[80] S. Oswald, W. Brückner, XPS depth profile analysis of non-stoichiometric NiO films, Surf. Interface Anal. 36 (2004) 17–22. https://doi.org/10.1002/sia.1640

[81] L. Wang, W. Chen, D. Zhang, Y. Du, R. Amal, S. Qiao, J. Wu, Z. Yin, Surface strategies for catalytic CO2 reduction: from two-dimensional materials to nanoclusters to single atoms, Chem. Soc. Rev. 48 (2019) 5310–5349. https://doi.org/10.1039/c9cs00163h